

A POST-BUCKMINSTERFULLERENE VIEW OF CARBON CHEMISTRY

Harold Kroto

School of Chemistry and Molecular Sciences,
University of Sussex, Brighton, BN1 9QJ UK

Keywords: C₆₀, Fullerenes, carbon particles

INTRODUCTION

The discovery of C₆₀ Buckminsterfullerene, Fig 1, has its origins in a research programme involving synthetic chemistry, microwave spectroscopy and radioastronomy¹. In 1975, at Sussex (with David Walton), the long chain polyyne H-C≡C-C≡C-C≡N was synthesised and studied by microwave spectroscopy. Subsequently, with Takeshi Oka and NRC(Ottawa) astronomers, the molecule was discovered in space, Fig 2, by radioastronomy using the laboratory microwave frequencies.

This discovery led on to the detection of the even longer carbon chain molecules HC₇N, HC₉N and HC₁₁N in the space between the stars². Further work aimed at understanding the formation of the chains in space focussed attention on the possibility that they are produced at the same time as carbon dust in red giant stars^{1,2}. During experiments at Rice University in 1985 (with James Heath, Sean O'Brien, Robert Curl and Richard Smalley), designed to simulate the conditions in these stars and explore their capacity for carbon chain formation, the exciting discovery that C₆₀ was remarkably stable was made³. It was found that under conditions where almost all the atoms in a carbon plasma had nucleated to form microparticles the molecule C₆₀ remained behind - together with some C₇₀. This result was, as is now well known, rationalised on the basis of the closed cage structure shown in Fig 1. It was proposed that the geodesic and aromatic factors inherent in such a structure could account for the stability of the molecule.

THE CIRCUMSTANTIAL EVIDENCE FOR THE EXISTENCE OF FULLERENES

Many subsequent experiments, carried out during the period 1985-90 provided compelling evidence for the exceptional stability of C₆₀ whatever its structure might have been^{2,4}. For instance support for the structure had been obtained by showing that the mass spectrometric magic numbers observed in cluster experiments were consistent with the formation of a whole family of closed cages, the fullerenes Fig 3^{5,2}. Particularly convincing was the fact that the smallest cages, in which all the 12 pentagons needed for closure are isolated, are C₆₀ and C₇₀⁵.

To explain the spontaneous creation of such an unexpected species in a chaotic carbon plasma a simple refined nucleation mechanism^{6,7} was developed. It was also recognised that the mechanism could not only account for C₆₀ but it also⁷ explained the detailed structure of carbon microparticles such as those that Iijima⁸ had observed (Fig 4a). In this scheme it is proposed that when carbon nucleates, curved and closing graphitic shells form⁶ (rather than flat sheets as has

traditionally been assumed) and these wrap up under epitaxial control⁷. It predicts that the embryos involved in carbon particle growth are partially closed cages which grow into quasi-icosahedral graphite particles⁷. This mechanism explains the formation of the fullerene cages, C₆₀ in particular, as resulting from closure during the general carbon microparticle formation process. It is proposed that embryos that do not close grow directly into graphite microcrystals essentially consisting of imperfect, concentric quasi-icosahedral spirally interconnected shells. The mechanism is supported by simulated TEM images (Fig. 4b) derived for the structures predicted by the new scheme⁹ which show excellent agreement with the elegant electron microscope images of carbon microparticles obtained by Iijima⁸ in 1980, Fig 4a.

It was also recognised that there were significant similarities between the structures of the pure carbon particles and soot particles and that both could be explained by essentially the same scheme (albeit in perturbed form for soot). This proposal has been criticised on various grounds¹⁰, however detailed analysis of soot¹¹ reveals that there are numerous serious gaps in our understanding of the formation process, indeed sufficient to show that the new scheme cannot be discounted readily¹². Harris and Weiner¹¹ said, in 1985, that "...knowledge of the chemistry (of soot formation) has been totally absent." so there would appear to be some room for some fresh ideas on the chemistry involved. The new mechanism does appear able to explain many observations more simply than some previous models such as those involving liquid droplet formation in which it appears the substructure is thought to be held in place van der Waals forces. The mechanism predicts that C₆₀ should be a by-product of the soot formation process⁶. Interestingly Gerhardt, Löffler and Homann¹³ subsequently showed that C₆₀⁺ is the major ion in a sooting flame. Homann has however pointed out that this observation is not necessarily to be taken as support for the new scheme.

THE PRODUCTION AND CHARACTERISATION OF BUCKMINSTERFULLERENE

In August 1990 the scepticism which surrounded the original fullerene-60 proposal was finally laid to rest by the breakthrough made by two groups, Krätschmer, Lamb, Fostiropoulos and Huffman¹⁴ (Heidelberg/ Tucson) and Taylor et al¹⁵ (Sussex). From the carbon deposit produced from arc processed graphite Krätschmer et al¹⁴ obtained a crystalline material. X-ray analysis showed it to consist of arrays of spherical C₆₀ molecules of exactly the expected size. Mass spectrometric and infrared data were further confirmation. From similarly processed graphite Taylor et al¹⁵ also obtained mass spectrometric evidence for fullerene-60 and also extracted a red solution (in benzene) independently. Subsequently they chromatographically separated the material into two components C₆₀ and C₇₀. The ¹³C NMR analysis of the beautiful magenta solution of C₆₀ yielded a single line resonance (Fig 5) indicating that all the C atoms in the molecule are equivalent! A result perfectly commensurate with the proposed fullerene-60 structure. Elegant support came from the spectrum of C₇₀ which showed that it had five lines (Fig 5), again in perfect agreement with expectation. This result was also important as it showed that other members of the fullerene family existed.

POSTBUCKMINSTERFULLERENE CHEMISTRY

Since this breakthrough was made in September 1990 the field has exploded and all aspects of the chemical and physical properties of the fullerenes are now being investigated in minute detail. The fact that this new, third form of carbon exists, is created spontaneously and has been under our noses since time immemorial is somewhat difficult to accept. Indeed fullerenes appear to make up some 10-30% of the material produced by the carbon arc and it has now been shown to reside in soot. Howard and co-workers who have found the fullerene content of soot from a benzene flame can be as high as 7% under certain conditions.

These observations have major implications; in particular for:

- 1) The composition of carbon vapour,
- 2) The mechanism of carbon nucleation,
- 3) The structure of graphitisable carbons,
- 4) Fluid carbon phases,
- 5) Soot formation,
- 6) The structure of interstellar and circumstellar grains,
- 7) Structure and synthesis of new polyaromatic hydrocarbons,
- 8) New metal-carbon complexes and intercalation compounds

New advances are made every day as the material becomes more and more accessible and a complete review of the material published on C₆₀ Buckminsterfullerene by the end of 1990 has been written⁴.

ACKNOWLEDGEMENTS

The success in the most recent work at Sussex was made possible by the expertise, effort and help of: Wahab Allaf, Simon Balm, John Dennis, Laurence Dunne, Richard Hallett, Jonathan Hare, Ken McKay, A Abdul-Sada, Amit Sarkar, Roger Taylor, David Walton and Steve Wood. We also thank the SERC.

LITERATURE CITED

1. H W Kroto, Chem. Soc. Revs., 11, 435-491 (1982).
2. H W Kroto, Science, 242, 1139-1145 (1988)
3. H W Kroto, J R Heath, S C O'Brien, R F Curl and R E Smalley, Nature, 318, 162-163, (1985).
4. H W Kroto, A W Allaf and S P Balm, Chem Revs (in press)
5. H W Kroto, Nature, 329, 529-531 (1987)

6. Q L Zhang, S C O'Brien, J R Heath, Y Liu, R F Curl, H W Kroto and R E Smalley, *J Phys Chem.*, 90, 525-528 (1986)
7. H W Kroto and K McKay, *Nature*, 331, 328-331 (1988)
8. S Iijma, *J Cryst Growth* 50 675-683 (1980)
9. K G McKay, D Wales and H W Kroto, in preparation
10. L B Ebert, R V Kastrup, J C Scanlon and R D Sherwood, 19th Biennial Conf. Carbon (Penn State) 396-397
11. S J Harris and A M Weiner, *Ann. Rev. Phys. Chem.*, 36, 31-52 (1985)
12. H W Kroto (in preparation)
13. P H Gerhardt, S Löffler and K H Homann, *Chem Phys Letts* 137, 306 (1987)
14. W Krätschmer, L D Lamb, K Fostiropoulos and D Huffman, *Nature*, 347, 354-358 (1990)
15. R Taylor, J P Hare, A K Abdul-Sada and H W Kroto, *J. C. S. Chem. Comm.*, 1423-1425 (1990)
16. J B Howard, J T McKinnon, Y Makarovsky, A L Lafleur and M E Johnson, *Nature* (in press)

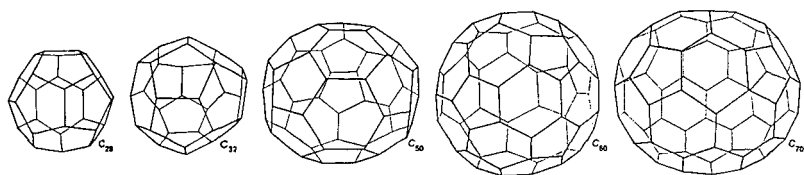


Fig 3 Family of relatively stable Fullerenes⁵

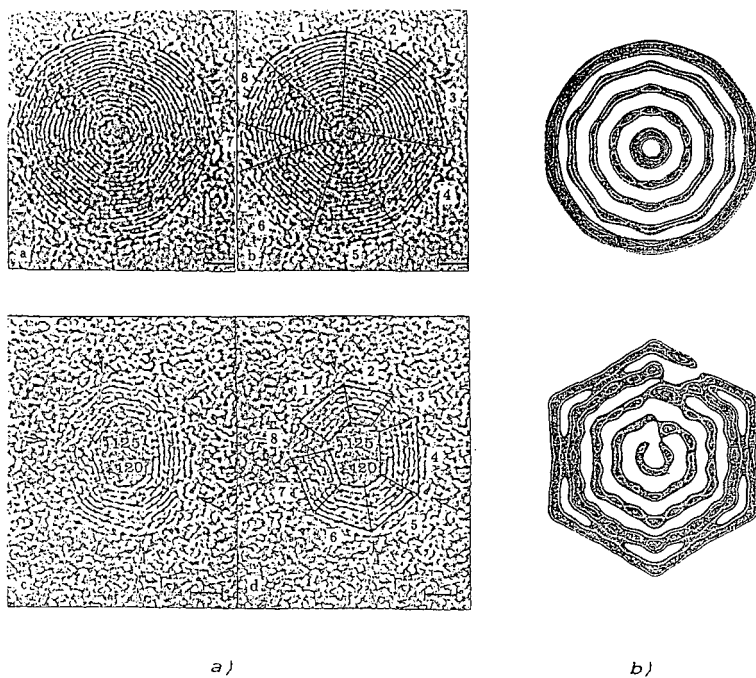


Fig 4 Comparison between TEM images of polyhedral graphite microparticles observed by Iijima⁸ a) and simulated images for a hypothetical icospiral microparticle (two different angles) b)

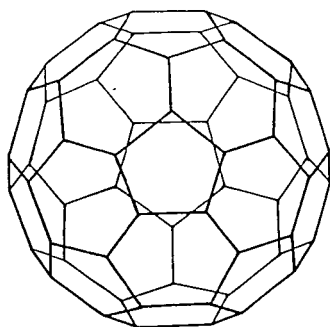


Fig. 1 C_{60} Buckminsterfullerene.

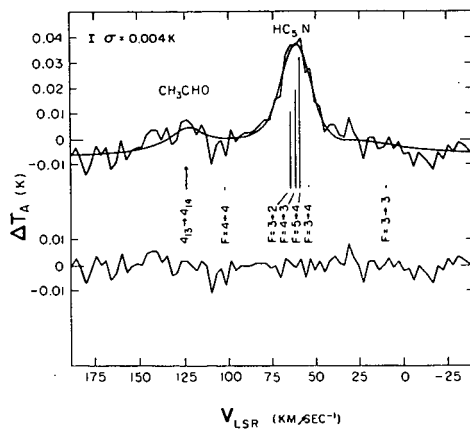


Fig. 2 Radio line of HC_5N observed in a giant molecular cloud SgrB2 near the center of the Galaxy

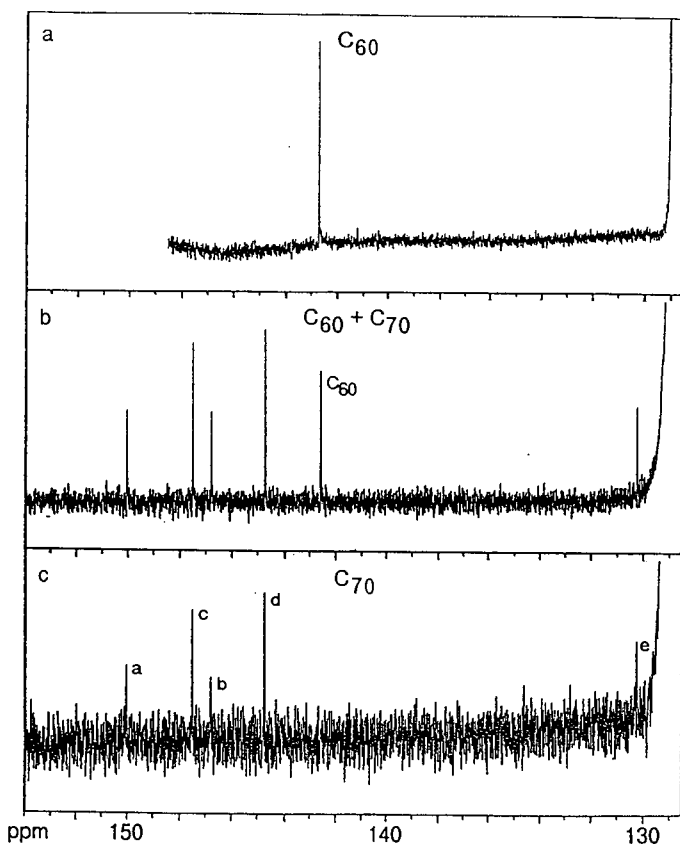


Fig 5 ^{13}C NMR spectrum of Fullerene-60

PRODUCTION AND CHARACTERIZATION OF FULLERENES IN FLAMES

Jack B. Howard, J. Thomas McKinnon, Yakov Makarovsky,
Arthur L. Lafleur, and M. Elaine Johnson
Department of Chemical Engineering and
Center for Environmental Health Sciences
Massachusetts Institute of Technology
Cambridge, Massachusetts 02139-4307

Keywords: fullerenes, C_{60} , flames

ABSTRACT

Closed-cage all-carbon molecules referred to as fullerenes were discovered in carbon vapor from laser heating of graphite and subsequently produced in macroscopic quantities by resistive heating of carbon rods. Suggestions that fullerenes may be involved in soot formation, and the detection, in flames, of all-carbon ions having the same masses as fullerenes, have generated much interest in the possible formation of fullerenes in flames. Combustion experiments and chemical analyses will be reported which have been conducted over ranges of flame conditions to determine if fullerenes can be produced in flames and to assess the relationship between fullerenes and soot.

INTRODUCTION

Fullerenes were discovered¹ in carbon vapor produced by laser irradiation of graphite, and have recently been produced in macroscopic quantities^{2,3,4} by graphite vaporization with resistive heating. Fullerene C_{60} is a closed cage carbon structure containing 20 six-membered rings and 12 five-membered rings with the appearance of a soccer ball. There has been a surge of scientific interest in these compounds because they represent a new class of carbon in addition to the two known forms, graphite and diamond. There has also been much practical interest in fullerenes. Many potential applications have been suggested, including catalysts and superconductors produced by incorporation of metal atoms with the fullerenes, and super lubricants produced by fluorination of fullerenes.

That fullerenes may be formed in sooting flames has frequently been suggested^{5,6,7,8} since the early days of fullerene research. Zang et al.⁵ considered the possible role of carbon shell structures in the formation and morphology of soot. They envisioned the growth of successive shells, separated by roughly the 0.33 nm intersheet distance in graphite, producing a soot nucleus consisting of concentric but slightly imperfect spheres, with the edge of the outermost shell giving a very rapid growth front. Kroto and McKay⁶ described a carbon nucleation scheme involving quasi-icosahedral spiral shell carbon particles, and suggested it may apply to soot. Curl and Smalley⁷ suggested carbon nets in the form of spiral structures may be important to soot formation in flames.

In spite of early predictions that fullerenes may be associated with soot formation and morphology, confirming evidence has not been produced although all-carbon ions having the same molecular weights as fullerenes have been detected in flames^{9,10,11}. Also, Pope¹² (see Pope and Howard, Fuel Chemistry Div. Preprints, this Meeting) has determined that compounds in the mass range 700-750 amu in a flame behave in a manner consistent with the relatively stable fullerene C_{60} being a substantial fraction of the material in this mass range. This conclusion

resulted from a study of molecular beam mass spectrometer data obtained by Bittner¹³ in a near-sooting benzene-oxygen flame. Similar flames but in the sooting regime were studied by McKinnon¹⁴, whose data on high molecular weight soot precursors gave interesting but inconclusive evidence pertinent to the possible presence of fullerenes. The subsequent application of soot extraction techniques similar to those employed in the graphite vaporization studies revealed the presence of fullerenes in soot deposited on surfaces of the combustion chamber in McKinnon's studies (McKinnon and co-workers, submitted for publication).

EXPERIMENTAL

In order to determine if fullerenes are formed in flames, soot samples were collected from flames under ranges of conditions and analyzed using conventional techniques. Premixed laminar flames of benzene and oxygen with argon diluent were stabilized on a water-cooled burner in a low-pressure chamber equipped with windows and feed-throughs for visual observation, optical diagnostics and probes, and exhausted into a vacuum pump. The burner consists of a horizontal drilled copper plate (100 mm diameter, 12 mm thick, 1 mm diameter holes centered 2.5 mm apart in a triangular grid) in the end of a tube, upward through which the feed mixture is delivered. The flame is stabilized with a flat front uniformly displaced from a drilled copper burner plate by a short distance which depends on the velocity of the gas leaving the burner and the flame speed of the mixture. The flame is surrounded by an annular nonsooting flame which provides a thermal shield, giving an approximately one-dimensional core within which temperature and species concentrations vary only with distance, or residence time, from the burner surface. The burner was previously used in mechanistic studies of soot nucleation and growth¹⁵, and the flames studied are of a type for which considerable data on temperature and chemical composition are available⁹⁻¹⁸.

Flames were produced under different sets of conditions over the ranges: burner chamber pressure, 1.60-13.35 kPa; atomic C/O ratio, 0.96-1.07; mol % Ar, 0-39; gas velocity at the burner (298 K), 14-75 cm/s. Each flame was maintained for 1.6 to 2.8 hr, during which a soot sample was withdrawn from the flame at a given distance from the burner using a quartz probe connected to a room-temperature filter, vacuum pump, and gas meter. Soot was also collected from the inside surface of the burner chamber after each run. Using flame temperature and gas composition information, the soot masses and gas volumes collected with the probe in the different flames are found to correspond to soot yields in the range 0.8 to 12% of the carbon fed.

The soot samples were extracted with toluene, using an ultrasonic bath at room temperature, and filtered. The solution from one of the samples was evaporated to dryness and analyzed with a Varian-MAT model 731 mass spectrometer interfaced to a Teknivent data system using a direct injection probe heated from 373 K to 673 K and electron impact ionization. The mass spectrum has been submitted for publication.

The toluene extracts were fractionated with a high performance liquid chromatograph (HPLC) coupled to a spectrophotometric diode-array detector (DAD). A separation scheme proven effective for large polycyclic aromatic hydrocarbons (PAH)²⁰⁻²² was used. The column (4.6 mm i.d., 250 mm length) was packed with 5 μ m Nucleosil octadecylsilyl-bonded silica having 300 Å pore size. A reverse-phase solvent system of methanol/dichloromethane was used. The mobile phase program consisted of a linear increase in dichloromethane concentration from 10-100% in 40 min with a 10 min hold time at 100%. The flow rate was 1.0 mL/min. In HPLC chromatograms for the toluene extracts, the broadband DAD response

is roughly proportional to mass for PAH²³.

In order to obtain broadband ultraviolet-visible (UV-Vis) spectra, solutions from HPLC fractionation of the soot extracts were concentrated by evaporation under nitrogen and the HPLC mobile phase was replaced with spectro-grade decalin. The UV-Vis spectra of the different peaks of interest were acquired over the 200-800 nm wavelength interval using a Hewlett-Packard 8450 A spectrophotometer. Mass spectra of these HPLC fractions were acquired using the equipment and technique mentioned above. The identities of the HPLC peaks suggested by UV-Vis spectra were confirmed by mass spectra. The HPLC method was then used to analyze the toluene extracts of all the soot samples.

The experimental results, which have been submitted for publication, not only show whether fullerenes are formed in flames but also reveal behavior of interest in comparison with that of the graphite vaporization technique for fullerenes production.

ACKNOWLEDGEMENTS

We thank Chenhui Zeng and Catherine Costello of the MIT Mass Spectrometry Facility (NIH Grant No. RR00317 to K. Biemann) for assistance in obtaining the mass spectra. The combustion research was supported by the Division of Chemical Sciences, Office of Basic Energy Research, Office of Energy Research, U.S. Department of Energy under Grant No. DE-FG02-84ER13282. The analytical investigation was supported in part by the National Institute of Environmental Health Sciences under Center Grant EHS-5P30-ES02109-10 and Program Grant EHS-5P01-ES01640-11. M.E.J. was supported by a Dow Fellowship Award from the MIT Undergraduate Research Opportunities Program.

REFERENCES

- (1) Kroto, H.W.; Heath, J.R.; O'Brien, S.C.; Curl, R.F.; Smalley, R.E. Nature 1985, **318**, 162-164.
- (2) Krätschmer, W.; Lamb, L.D.; Fostiropoulos, K.; Huffman, D.R. Nature 1990, **347**, 354-358.
- (3) Ajie, H.; Alvarez, M.M.; Anz, S.J.; Beck, R.D.; Diederich, F.; Fostiropoulos, K.; Huffman, D.R.; Krätschmer, W.; Rubin, Y.; Schriver, K.E.; Sensharma, D.; Whetten, R.L. J. Phys. Chem. 1990, **94**, 8630-8633.
- (4) Haufler, R.E.; Conceicao, J.; Chibante, L.P.F.; Chai, Y.; Byrne, N.E.; Flanagan, S.; Haley, M.M.; O'Brien, S.C.; Pan, C.; Xiao, Z.; Billups, W.E.; Ciufolini, M.A.; Hauge, R.H.; Margrave, J.L.; Wilson, L.J.; Curl, R.F.; Smalley, R.E. J. Phys. Chem. 1990, **94**, 8634-8636.
- (5) Zhang, Q.L.; O'Brien, S.C.; Heath, J.F.; Liu, Y.; Curl, R.F.; Kroto, H.W.; Smalley, R.E. J. Phys. Chem. 1986, **90**, 525-528.
- (6) Kroto, H.W.; McKay, K. Nature 1988, **331**, 328-331.
- (7) Curl, R.F.; Smalley, R.E. Science 1988, **242**, 1017-1022.
- (8) Kroto, H. Science 1988, **242**, 1139-1145.

- (9) Gerhardt, Ph.; Löffler, S.; Homann, K.H. Chem. Phys. Lett. 1987, **137**, 306-310.
- (10) Gerhardt, Ph.; Löffler, S.; Homann, K.H. Twenty-Second Symposium (International) on Combustion, The Combustion Institute, 1989, 395-401.
- (11) Löffler, S.; Homann, K.H. Twenty-Third Symposium (International) on Combustion, The Combustion Institute, Pittsburgh, in press.
- (12) Pope, C.J. Fluxes and Net Reaction Rates of High Molecular Weight Material in a Near-Sooting Benzene-Oxygen Flame; M.S. thesis, M.I.T., Cambridge, Massachusetts, 1988.
- (13) Bittner, J.D.; Howard, J.B. Eighteenth Symposium (International) on Combustion, The Combustion Institute, Pittsburgh, 1981, 1105-1106.
- (14) McKinnon, J.T. Chemical and Physical Mechanisms of Soot Formation; Ph.D. thesis, M.I.T., Cambridge, Massachusetts, 1989.
- (15) Homann, K.H.; Mochizuki, M.; Wagner, H.Gg. Z. Phys. Chem. N.F. 1963, **37**, 299-313.
- (16) Homann, K.H.; Morgeneyer, W.; Wagner, H.Gg. Combustion Institute European Symposium ed. F.J. Weinberg; Academic Press: London, 1973, 394-399.
- (17) Olson, D.B.; Calcote, H.F. Eighteenth Symposium (International) on Combustion, The Combustion Institute, Pittsburgh, 1981, 453-462.
- (18) Bockhorn, H.; Fetting, F.; Wenz, H. Ber. Bunsenges. Phys. Chem. 1983, **87**, 1067-1073.
- (19) Howard, J.B.; Bittner, J.D. Soot in Combustion Systems and Its Toxic Properties, eds. J. Lahaye and G. Prado; Plenum: New York, 1983, 57-91.
- (20) Fetzer, J.C.; Biggs, W.R. J. Chromatogr. 1985, **322**, 275-286.
- (21) Fetzer, J.C.; Biggs, W.R. J. Chromatogr. 1985, **346**, 81-92.
- (22) Fetzer, J.C.; Biggs, W.R. J. Chromatogr. 1984, **295**, 161-169.
- (23) Lafleur, A.L.; Monchamp, P.A.; Plummer, E.F.; Wornat, M.J. Anal. Lett. 1987, **20**, 1171, 1192.

Sublimation and Heterogenous Reactions of Fullerene (C_{60}) in Different Gases

Ismail M. K. Ismail
University of Dayton Research Institute
c/o Phillips Lab/RKFC
Edwards Air Force Base, CA 93523-5000, USA

ABSTRACT

The sublimation process and heterogeneous reactions of C_{60} Fullerene under a flow of argon, air, or hydrogen have been investigated at 25-1000 C. The results are compared against those obtained with other forms of well characterized carbons; Saran char (a highly reactive disordered carbon) and SP-1 graphite (less reactive, well ordered carbon). In Ar, 83% of the C_{60} aggregates (examined here) sublime, leaving behind a carbonaceous non-volatile residue insoluble in toluene. In air, the C_{60} first chemisorbs (reacts with) oxygen to a limit corresponding to 1.5 oxygen atoms/ C_{60} molecule. The carbon then loses weight (gasifies) at a rapid rate; higher than the rate of Saran gasification. In hydrogen, while the rates of SP-1 and Saran gasification at 1000 C are insignificant, the volatile part of C_{60} aggregates completely sublimes or gasifies at 500-800 C, leaving behind the 17% residue left after the sublimation process. Some possible future applications of C_{60} , particularly in the areas of carbon composites and molecular sieve materials, are addressed.

Keywords: C_{60} , Buckyballs, Fullerene.

INTRODUCTION

Fullerene C_{60} , a newly established form of carbon, is a molecule containing 60 carbon atoms arranged in a closed hollow cage with 32 faces; 12 pentagons and 20 hexagons [1]. The molecule is a stable cluster of carbon atoms often known as "buckyball". The buckyballs are prepared by laser vaporization of graphite discs [1-3], and by carbon arc vaporization of graphite rods [4-6]. The evaporation is performed under subambient pressures (100-200 Torr) at 1000-1300 C in an inert atmosphere of helium or argon. The graphite vapor nucleates in the gas phase forming particles which are collected on a cold substrate, yielding soot and aggregates of C_{60} with a small fraction of other larger cages. To isolate the buckyballs the particles are first dispersed in a solvent; benzene [4], toluene or carbon disulfide [5,6]. The buckyballs dissolve but the other forms of carbon (soot) remain suspended. After filtration, the solvent is evaporated, leaving behind aggregates of C_{60} .

The structure of buckyballs has been supported by infrared and ultraviolet spectra [1,4], by NMR [7], and by theoretical calculations [8,9]. The literature is full of C_{60} physical properties; including electrical and magnetic properties [10,11], electron energies [12-14] and optical spectrum [14]. Scanning Tunneling Microscopy has indicated that the C_{60} molecules are arranged in hexagonal arrays with an intercluster spacing of 1.0-1.1 nm [15,16]. The spacing agrees with the sum of the theoretical molecular diameter of C_{60} (0.701 nm) plus the interlayer spacing of graphite (0.335 nm). These values are also in agreement with those calculated from X-ray and electron diffraction studies [17]. With the assumption that the C_{60} molecules are arranged in a hexagonal close-packed lattice, the estimated nearest neighbor distance is 1.002 nm, and the X-ray density is 1.678 g/cc. It is consistent with the experimental value of 1.65 ± 0.05 g/cc obtained by density gradient columns [17].

The structure of C_{60} and its different methods of preparation are well established. The buckyballs can now be prepared at a rate of 10 g/h or higher [6]. Yet, little is known about their properties and performance as a truly carbonaceous material. Because of their unique spherical structure, the C_{60} molecule does not have dangling carbon atoms or active sites as the other carbonaceous materials. The C_{60} molecules should be less reactive to air, hydrogen, or oxidizing agents than the other carbons. The treatment of soot and fullerene with perchloric acid at 100-160 C has verified this point [18]. The treatment indicated that fullerene is more oxidation resistant than soot [18]. On the other hand, C_{60} sublims at considerably lower temperatures than the other carbons. Therefore, when exposed to air at

high temperatures, the homogeneous reaction between air and C_{60} in the gas phase (if any) could be faster than the "normal" heterogeneous reaction between air and active sites of the other carbons. Thus, it is not clear how the behavior of C_{60} in different gases compares to the other forms of carbon.

The objective of the present work is to address several subjects. First, how does C_{60} respond when heated in inert or reactive medium. Initially, we discuss the sublimation reaction of C_{60} in Ar. Then we move to the reaction between C_{60} and air or H_2 . Second, a comparison is made between the reactivity of C_{60} and other forms of carbon. We finally outline some potential future applications of this form of carbon; especially in the areas of carbon composites and molecular sieve carbons.

EXPERIMENTAL

Materials

Two batches (A and B) of C_{60} crystals were graciously supplied by Professor D. R. Huffman (University of Arizona - Tucson). They were used as-received, without further purification. To understand their relative reactivity in air or H_2 , two additional carbons were included in the study; a reactive Saran char and a considerably less reactive SP-1 graphite. Saran is a highly disordered non-graphitic char with a large micropore surface area of $850 \text{ m}^2/\text{g}$ [19], an average micropore width of 1.05 nm [20], and an active surface area (ASA) of $37 \text{ m}^2/\text{g}$ [19]. The sample has a low level of impurities [19], so we can rule out the catalytic effects which enhance the rates of C/O_2 and C/H_2 reactions. SP-1, on the other hand, is composed of well ordered natural flakes which have been purified by the manufacturer to a minimum level of impurities. It is non-porous graphite with an external surface area of $2.00 \text{ m}^2/\text{g}$ [21] and an ASA of $0.05 \text{ m}^2/\text{g}$ [22].

Measurements of Reaction Rates

The experiments were performed on a Cahn Thermogravimetric Analyzer (TGA), system 113, connected to a vacuum system. The samples (about 5 mg) were evacuated at room temperature until a pressure of 10^{-5} Torr was reached. The sample was flushed with ultrahigh purity Ar flowing at 50 cc/min to ambient pressure. Then, starting from room temperature, all samples were heated at a constant heating rate (HR) in, Ar, air, or H_2 flowing at 50 cc/min. The change in sample weight was monitored as a function of temperature and time every 15 sec.

RESULTS AND DISCUSSION

The Sublimation Process in Argon

Figure 1 illustrates the drop in C_{60} weight, due to sublimation, as a function of temperature (HR = 5 C/min). The sublimation in Ar begins at 550 C and ends at 900 C; the two temperature limits are dependent on HR and sample size. At higher temperatures, 900-1000 C, there was no further drop in sample weight. The apparent remaining weight of residue was $21.6 \pm 0.7 \%$ of the original sample. To get the true weight, a correction had to be made which takes into consideration the thermal and buoyancy effects imposed by reactor geometry, HR, geometry of sample container, and type of gas injected as well as its flow rate. When the TGA reactor is heated, the density of the flowing gas drops, and as a result, there is an apparent mass-gain which increases with temperature. By performing a blank run, with Ar flowing at 50 cc/min over empty sample container, the proper correction factors at different temperatures have been obtained. At 900 C, the correction factor is 4.6%. Therefore, the true weight of the C_{60} residue, left after the sublimation reaction, is $21.6 - 4.6 = 17.0\%$.

When the samples reached 1000 C in Ar, with no indication of further weight change, they were held isothermally at this limit. Air was then introduced to replace Ar at the same flow rate. The residue gasified with the liberation of only CO which is normally the main product for the carbon/ O_2 reaction at 1000 C. After gasification, the apparent final weight dropped from 21.6 to 4.9%, the latter value is equivalent to the new correction factor at 1000 C, 4.9%. It means that the "non- C_{60} " residue is just

another stable form of carbon or soot. This trend has been confirmed with all batch A and B samples not only after the sublimation process, but also after the hydrogenation reaction (Section 3.4).

These results imply that the C_{60} aggregates, at least the ones examined in this study, are composed of 83% volatile C_{60} carbon contaminated with 17% of "non- C_{60} " carbon. Since the X-ray and experimental densities are very close [17], the density of both type of carbons should be essentially the same. The 83 to 17 ratio suggests that each five molecules of C_{60} are approximately associated with one particle of the "non- C_{60} " carbon. If one assumes that the particle volume is, on the average, equivalent to the size of one C_{60} molecule; 0.180 nm^3 , the X-ray dimensions of the particle can be estimated. Knowing that the area of one graphitic hexagon is 0.052 nm^2 , and assuming the particle has an average interlayer spacing of 0.35 nm , the number of hexagons in the particle can be estimated. If the particle has three graphitic layers, as a first reasonable guess, this number is given by: $0.180/(0.052 \times 0.7) = 4.9$; about 5 hexagons. A graphitic crystal with such a small size ($0.57 \times 0.7 \text{ nm}$) is hard to exist. Therefore, the "non- C_{60} " carbon component in the aggregates is probably present as larger particles of soot randomly imbedded within the C_{60} crystal.

The question is then raised regarding the residue origin. The residue could be a biproduct formed during the sublimation of C_{60} . In other words, a polymerization reaction could be taking place in Ar at elevated temperatures to form larger stable graphitic crystals. Alternatively, the residue could be composed of soot or particulates that were originally present with the buckyballs but trapped inside the aggregates. The solvent extraction process was not able to completely remove the residue because the size of these particles is very small. During the filtration process, they may have passed through the filtering device and stayed with the C_{60} extract solution. At present, the possibility of a polymerization reaction cannot be ruled out, however, the last explanation is probably more valid. It is noteworthy to add that the residue obtained after sublimation is insoluble in toluene.

Oxidation in Air

Exposure of C_{60} to air, Figure 2, is associated with two main processes; a weight increase at lower temperatures, followed by a weight decrease at higher temperatures. While the increase in weight is attributed to oxygen chemisorption or an addition reaction, the weight loss is due to carbon gasification. Unlike the sublimation process, the oxidation reaction shows some difference between batch A and B. The reason for this discrepancy may be due to the way by which the C_{60} molecules aggregate in each batch. It could also be dependent on the average particle size or distribution. Apparently either the internal structure and porosity of batch B is more open than A, or the average particle size of B is smaller than A. With either explanation, batch B chemisorbs (or reacts with) more oxygen than A as shown in Figure 2. In spite of this difference, the general trend with both C_{60} samples is essentially the same. The weight increases to reach a maximum value, then the rate gradually decreases. With batches B and A, the maximum "apparent" increase in weights at 360-380 C are 5.4 and 4.8%, respectively. After considering the proper correction factor of 2.4% at 360-380 C, the corresponding true maximum weight gains of oxygen are reduced to $5.4-2.4 = 3.0\%$ and $4.8-2.4 = 2.4\%$, or 30 and 24 mg O_2/g C_{60} , respectively. The average value of the two is 27 mg O_2/g C_{60} which yields 0.73 mole $O_2/mole$ C_{60} . This calculation assumes that the molecular weight of fullerene is 720, and that oxygen molecules are only consumed by the C_{60} component in the crystal which constitutes 83% of the total carbon.

It is interesting to note that just before the beginning of C_{60} weight loss (gasification), each molecule acquires, on the average, $0.73 \times 2 = 1.46$ (say 1.5) oxygen atoms. There are several possible explanations for this. First, the "attack" with oxygen starts by opening, at least, one C=C bond to form an ether-type linkage on each C_{60} molecule. Then, on every other molecule, another C=C bond opens up in the same way. Second, one C_{60} molecule forms the ether-type bond while the next molecule converts a C=C to either C-O-O-C (peroxide) or two carbonyl groups. Third, some (accessible) C_{60} molecules are attacked by more than 1.5 oxygen atoms while others (hidden inside the crystal) are not attacked at all because oxygen cannot reach them. Fourth, several complicated organic reactions between C_{60} and O_2 could be taking place. Whatever the oxidation mechanism is, it is clear

that the gasification of the C_{60} crystals starts by formation of carbon-oxygen functional groups. This is exactly the mechanism of gasifying the other forms of carbon in air. It is well known that chemisorption of oxygen on carbons is the first step of the overall gasification reaction [23,24].

Let us look at the same data in a different way. The amount of oxygen uptake can be converted to estimate the active surface areas (ASA). ASA calculations assume the area occupied by one chemisorbed oxygen atom as $0.083 \text{ nm}^2/\text{site}$, and that each active site chemisorbs one oxygen atom [25]. Based on the two assumptions, the ASA of batches B and A, with maximum values of 30 and 24 $\text{mg O}_2/\text{g C}_{60}$, are 93.8 and 75 m^2/g , respectively. If, as just mentioned, each oxygen atom is shared by two carbon atoms, the ASA values are reduced by half to yield 46.9 and 37.5 m^2/g , respectively. Compared to other forms of carbon, the C_{60} ASA values are exceptionally high. With the other carbons, typical ASA values are 0.2 - 5.3 m^2/g for graphitized carbons [25,26], 2.2 - 11.3 m^2/g for ungraphitized carbons [26], and 37 m^2/g for the highly reactive microporous Saran char [19]. In fact, the C_{60} ASA values computed here represent a low estimate. The more realistic values should be even higher because the oxygen uptake at the maxima, shown in Figure 2, represents the net of two processes. Oxygen chemisorption which increases the weight and carbon gasification which lowers the weight. If gasification were not occurring concurrently with chemisorption at the maxima, the maximum weight gain and, consequently, the ASA would have been even higher.

Now we examine how the gasification reactions of C_{60} in air compare to other forms of carbons. With the non-isothermal oxidation procedure, which has been utilized in the current investigation, the results can be presented in different ways. The most useful ones are the oxidation rate profiles (ORP) and Arrhenius plots [27]. The ORP is a relation between the rate of weight loss (gasification rate) and sample temperature. Figure 3 compares the ORP of C_{60} , Saran (a highly reactive carbon) and SP-1 Graphite (a less reactive carbon). Both rates were based on starting sample weight. Once again, there is some difference between the ORP of batches A and B. Batch A is more reactive and starts gasifying at a slightly lower temperature (360 C) than B (380 C). The maximum rate of oxidation of batch A is higher, but occurs at a lower temperature than the maximum of B (430 vs 470 C). Nevertheless, both batches oxidize at considerably lower temperatures than Saran. In fact, it was noted that most of the C_{60} completely gasified when the highly reactive Saran char was just beginning to lose some weight. The main reason for the remarkable reactivity of C_{60} in air is its highly developed ASA. It is attributed to the early attack of oxygen on C_{60} molecules. If each C_{60} molecule is, on the average, attacked by at least one oxygen atom before the start of gasification, the buckyballs begin breaking down. This process continues at a faster rate during the course of gasification. Because of the increasingly large number of nascent carbon active [25] or reactive [28] sites generated, and the small size of carbon fragments generated during oxidation, the C_{60} gasifies faster than the rest of carbons.

Behavior of C_{60} in Different Gases

A comparison is now made between the sublimation process in Ar and gasification of C_{60} in air and hydrogen. The results, illustrated in Figure 4, reveal several features. First, the oxidation reaction is the fastest, the sublimation process is the slowest, and the hydrogenation reaction is in the middle. Second, the oxidation reaction starts and ends at a region far below the sublimation temperature range. The C_{60} carbon oxidizes in the solid form before it sublimates. Third, the shape of the profiles in Ar and H_2 are essentially the same. In air, the profiles look different, indicating that the C_{60}/O_2 reaction is more complicated than the other two reactions. The profile indicates that different type of sites (or two different forms of carbon: C_{60} and soot) are gasifying at different temperature ranges. Fourth, in spite of the low temperature range at which the C_{60} gasifies, the maximum rates of oxidation are 40-50% higher than the hydrogenation or sublimation rates measured at higher temperatures. Fifth, the similarity between the profiles of the C_{60}/H_2 reaction and C_{60}/Ar sublimation process is somewhat puzzling. If the C_{60}/H_2 reaction was a typical heterogeneous reaction, the profile shown in Figure 4 should have acquired, to some extent, the shape of the C_{60}/O_2 profiles. That is, the profile in H_2 should not have been symmetrical. Since this is not the case, other possible reasons have to be considered, and this subject is addressed next.

Reduction/Gasification of C₆₀ in Hydrogen

Figure 5 compares the Arrhenius plots of the C₆₀ sublimation and hydrogenation reactions. The plots were computed from the corresponding ascending branches of Figure 4. The Arrhenius plots are practically linear with activation energies of 39-42 Kcal/mole for the sublimation process, and 34 (batch A) or 42 (batch B) Kcal/mole for the hydrogenation reaction. Once again, batch A is slightly more reactive to H₂ than B. Thus, the activation energy in Ar and H₂ is practically the same, suggesting that there is some similarity between the nature of the two processes. On the other hand, the activation energy for the C₆₀/H₂ reaction is in line with those values reported in the literature for other carbon/hydrogen reactions; 36 ± 6 Kcal/mole at atmospheric pressure [29], and 35.8 - 50.9 Kcal/mole at 27 atm [30]. So far, the C₆₀ and the other "old" carbons appear to take the same activation energy path when exposed to H₂. However, the hydrogenation reaction of C₆₀ may be different than the normal gasification reactions of other carbons which yield CH₄.

The C₆₀ hydrogenation reaction takes place at a considerably lower temperature range than the rest of "older" carbons. Figure 6 illustrates this point. Under similar experimental conditions, the extent of gasifying the highly reactive Saran, and the less reactive SP-1 graphite, is small. The change in apparent sample weights between 500 and 1000 C is also small; less than 5% (no correction factor is included here). By contrast, the reaction between C₆₀ and hydrogen starts at 500 C and ends at 900 C. Once again, the carbon leaves behind the "non-C₆₀" residue (soot) which has low reactivity in H₂ at 1000 C, resembling Saran and SP-1 graphite.

Although the hydrogenation reaction of C₆₀ has an activation energy similar to the "old" carbon/H₂ reaction, one may conclude that fullerene is just gasifying in H₂ like a typical carbonaceous material. This may be true to some extent. Yet, at the present time, we cannot rule out other possible explanations until further conclusive experiments are performed. That is, the observed hydrogenation reaction may be taking place through an entirely different route than the "normal" C/H₂ gasification reaction. It is possible that H₂ molecules are opening the C=C bonds and saturating the surface with C-H bond, yielding C₆₀ H₃₆ and other smaller hydrocarbons. In other words, the reaction could merely be starting with hydrogen addition rather than carbon gasification. The resulting products, with different amounts of hydrogen, could simply be a wide variety of different organic molecules that have different sizes, properties, and boiling points. If this is the major reaction, then the TGA experiments were merely measuring the weight loss due to evaporation of organic compounds with minor contribution of gasification of the carbonaceous matrix.

CONCLUSIONS

1. The C₆₀ carbon crystals examined here sublime in inert atmospheres, leaving behind a non-volatile carbon residue weighing 17% of the original sample. The residue, possibly soot is another form of carbon which gasifies in air yielding CO at 1000 C and is insoluble in toluene.
2. Oxidation of C₆₀ in air starts by a weight gain process during which, each C₆₀ molecule acquires, on the average, 1.5 oxygen atoms. At this point, a portion of the C₆₀ molecules begin opening up. With increasing temperature, the buckyballs further oxidize with a concurrent gasification reaction of the carbonaceous matrix.
3. Under otherwise similar conditions, C₆₀ is considerably more reactive in air or hydrogen than the other forms of carbon. This is attributed to the fast rate of generating active sites when the C₆₀ molecules start breaking.
4. The hydrogenation reaction of C₆₀ may, or may not, resemble the "old" carbon/H₂ gasification reaction to yield CH₄. The current data indicate some similarity between the two carbons. However, at the present time, the possibility of other hydrogenation reactions, that may convert fullerene to other forms of hydrocarbons, cannot be ruled out.

FUTURE APPLICATIONS

There are several potential applications for this new form of carbon, especially in the areas of carbon composites and molecular sieve carbons. Carbon composites have been used extensively in several aerospace applications. When stored, especially in an environment with high humidity, the composite adsorbs (absorbs?) moisture, some of the mechanical properties may deteriorate, and the component weight increases. To avoid this, a layer (blanket) or two of C_{60} could be spread to cover the entire external surface and pore entrances of the component. The assumption is made here that C_{60} has a hydrophobic surface that does not adsorb moisture. This assumption is reasonable because the C_{60} molecule does not have functional groups which normally enhance the moisture adsorption on carbons. To "spread the blanket" on a composite, the process has to be performed in an oxygen-free atmosphere, perhaps under vacuum. While a C_{60} reservoir is heated, the composite surface is cooled. Alternatively, a very dilute solution of C_{60} in benzene or toluene can be sprayed on the substrate. The solvent is then evaporated leaving behind the C_{60} blanket. This process does not require large quantities of fullerene. Based on the 1.0 nm diameter of C_{60} molecules, the computed surface area is $675 \text{ m}^2/\text{g}$. This means that 6.2 g of C_{60} can make a "blanket" for a substrate whose area is equivalent to an acre!

The second potential application is the preparation of molecular sieve carbons, which are highly microporous carbons with large adsorption capacity. Yet the size of their pore entrances, the "gate", has to be tailored to the specific application. The C_{60} comes as good and bad news for preparing this class of carbons. The starting substrate for molecular sieve carbons is normally a microporous (activated) carbon with a wide micropore size distribution. If one layer of C_{60} is deposited on the micropore entrance, the "gate" is narrowed by approximately 1.0 nm. Deposition of additional layers will narrow the "gate" further by multiples of nanometers (2,3,4,5,...nm). If the average pore size is 1.3 or 2.3 nm, then deposition of one or two layers of C_{60} will reduce the "gate" (of both pores) to 0.3 nm. The product is an excellent sieve to separate argon from oxygen whose minimum dimensions are 0.38 and 0.28 nm, respectively [31]. The sieve will preferentially adsorb oxygen, leaving argon passing through the separation tower. This is the good news. Now, if the starting average pore size is 1.0 or 2.0 nm, the deposition of C_{60} will just close the pores; and with it, come the bad news.

ACKNOWLEDGEMENT: *The financial support of Air Force Office of Scientific Research under contract number F04611-83-C-0046 with the Phillips Laboratory OLAC is highly appreciated. The author acknowledges Professor D. R. Huffman for providing the two C_{60} samples. Special thanks go to Dr. E. J. Wucherer, Major W. Hurley, Dr. Jeff Gilman, Dr. Pat Carrick, Dr. W. Hoffman, and Mr. M. Mahowald for the fruitful stimulating discussions.*

REFERENCES

1. H. W. Koto, J. R. Heath, S. C. O'Brien, R. F. Curl and R. E. Smalley, *Nature* **318**, 162 (1985).
2. J. R. Heath, S. C. O'Brien, Q. Zhang, Y. Liu, R. F. Curl, H. W. Kroto, F. K. Tittel and R. E. Smalley, *J. Am. Chem. Soc.* **107**, 7779 (1985).
3. Q. L. Zhang, S. C. O'Brien, J. R. Heath, Y. Liu, R. F. Curl, H. W. Kroto, and R. E. Smalley, *J. Phys. Chem.* **90**, 525 (1986).
4. W. Kratschmer, K. Fostiropoulos, and D. R. Huffman, *Chem. Phys. Lett.* **170**, 167 (1990).
5. R. E. Haufler, Y. Chai, L. P. F. Chibante, J. Conceicao, Changming Jin, Lai-Sheng Wang, Shigeo Maruyama and R. E. Smalley, *Mat. Res. Soc. Symp. Proc.*, Boston, Mass., November (1990).
6. R. E. Haufler, J. Conceicao, L. P. F. Chibante, Y. Chai, N. E. Byrne, S. Flanagan, M. M. Haley, S. C. O'Brien, C. Pan, Z. Xiao, W. E. Billups, M. A. Ciufolini, R. H. Hauge, J. L. Margrave, L. J. Wilson, R. F. Curl and R. E. Smalley, *J. Phys. Chem.* **94**, 8634(1990).

7. C. S. Yannoni, R. D. Johnson, G. Meijer, D. S. Bethune, and J. R. Salem, *J. Phys. Chem.* **95**, 9 (1991).
8. M. D. Newton, and R. E. Stanton, *J. Am. Chem. Soc.* **108**, 2469 (1986).
9. H. P. Luthi and J. Almlof, *Chem. Phys. Lett.* **135**, 357 (1987).
10. P. W. Fowler, P. Lazzeretti and R. Zanasi, *Chem. Phys. Lett.* **165**, 79 (1990).
11. R. C. Haddon and V. Elser, *Chem. Phys. Lett.* **169**, 362 (1990).
12. S. Satpathy, *Chem. Phys. Lett.* **130**, 545 (1986).
13. R. C. Haddon, L. E. Brus and K. Raghavachari, *Chem. Phys. Lett.* **125**, 459 (1986).
14. S. Larsson, A. Volosov and A. Rosen, *Chem. Phys. Lett.* **137**, 501 (1987).
15. D. S. Bethune et.al., *Nature* **348**, 621 (1990).
16. J. L. Wragg et.al., *Nature* **348**, 623 (1990).
17. W. Kratschmer, L. D. Lamb, K. Fostirpoulos, and D. R. Huffman, AZPH-Th/90-44, University of Arizona (Department of Physics) Report (1990).
18. D. Heymann, *Carbon* **29**, 684 (1991).
19. I. M. K. Ismail and P. L. Walker, Jr., *Carbon* **27**, 549 (1989).
20. I. M. K. Ismail, Extended Abstract, Carbone 90, Carbon Conference held in Paris, July 16-20, p.38 (1990).
21. I. M. K. Ismail, *Carbon* **28**, 423 (1990).
22. J. M. Ranish and P. L. Walker, Jr., *Carbon* **28**, 887 (1990).
23. P. L. Walker, Jr., M. Shelef, and R. A. Anderson, *Chemistry and Physics of Carbon* **4**, 287 (1968).
24. P. L. Walker, Jr., *Carbon* **28**, 261 (1990).
25. N. R. Laine, F. J. Vastola, and P. L. Walker, Jr., *J. Phys. Chem.* **67**, 2030 (1963).
26. I. M. K. Ismail, M. M. Rose, and M. A. Mahowald, *Carbon* **29**, 575 (1991).
27. I. M. K. Ismail, Proceedings of the 20th Biennial Conference on Carbon, University of California, Santa Barbara, June (1991).
28. A. A. Lizzio, H. Jiang, and L. R. Radovic, *Carbon* **28**, 7 (1990).
29. E. R. Gilliland and P. Harrriott, *Ind. Eng. Chem.* **46**, 2195 (1954).
30. A. Tomita, O. P. Mahajan, and P. L. Walker, Jr., *Fuel* **56**, 137 (1977).
31. S. A. Verma and P. L. Walker, Jr., *Carbon* **28**, 175 (1990).

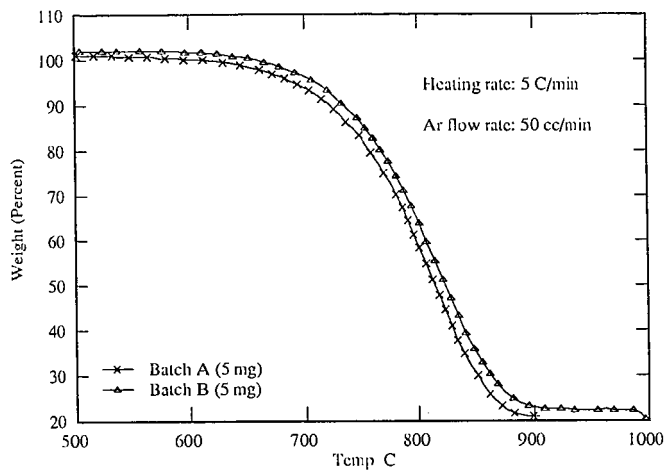


Figure 1: Sublimation of Fullerene (C₆₀) in Argon.

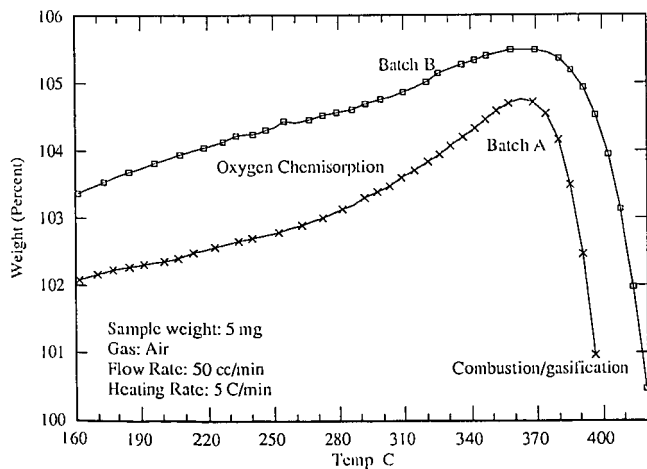


Figure 2: Reaction between Fullerene and Air at Low Temperatures.

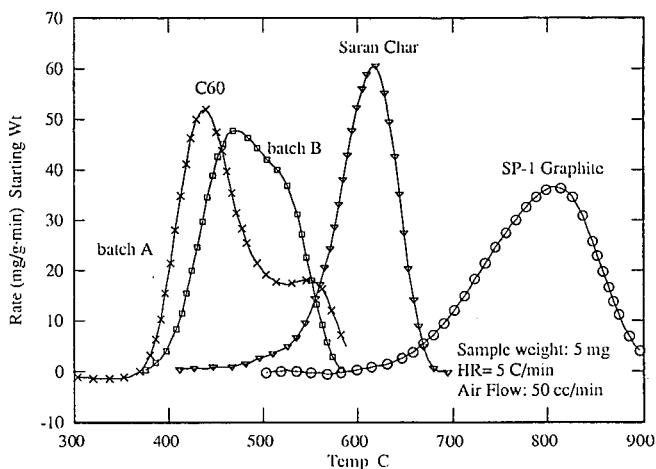


Figure 3: Comparison between Oxidation Rates of C60/ Saran/ SP-1 in air.

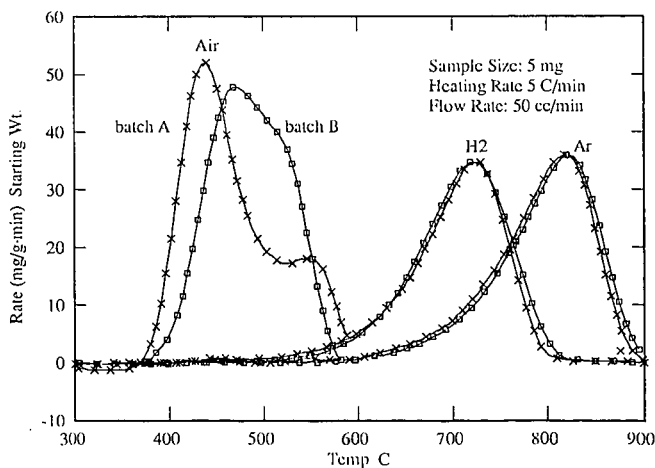


Figure 4: Reactions of Fullerene in Argon - Air and Hydrogen.

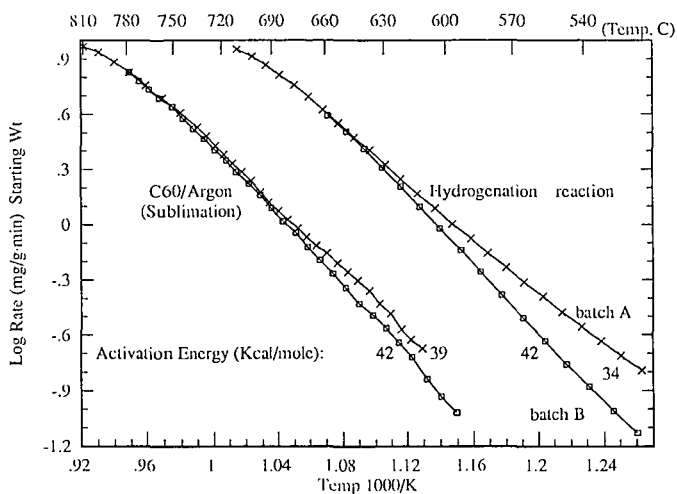


Figure 5: Arrhenius Plots for C60/Argon and C60/Hydrogen Reactions.

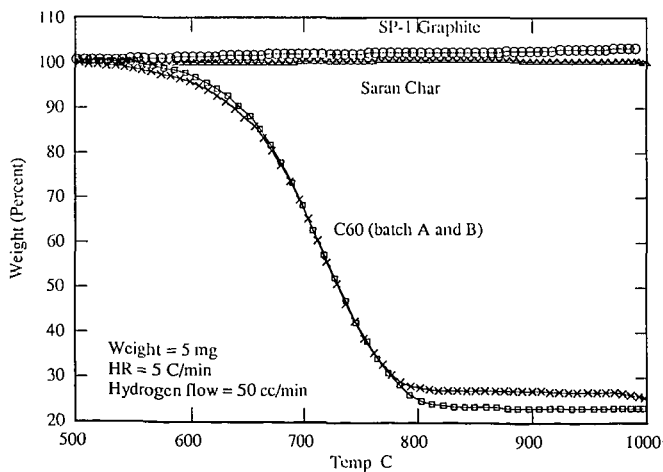


Figure 6: Comparison between C60 and other Forms of Carbon in Hydrogen.

CARBOPHANES: A NEW FAMILY OF CRYSTALLINE PHASES OF CARBON

R. H. Baughman and W. B. Hammond
Allied-Signal, Inc.
Research and Technology
Morristown, NJ 07962-1021

Keywords: Carbyne Carbon Phases, Carbophane Carbon Phases, Graphite Phase Transformation

I. Introduction:

This work is part of a continuing effort to develop structure-property predictions for new phases of carbon which are stable either at ambient or at high pressures [1]. The motivation is both to guide synthetic efforts to produce new carbon phases and to provide models for interpreting data for carbon phases of unknown structures.

Carbon crystals in which carbon exists in more than one hybridization state are the subject of the present analysis. Such materials are in sharp contrast with all available crystalline carbon phases with known structures, which contain either all sp^3 carbons (cubic diamond and Lonsdalite) or all sp^2 carbons (hexagonal graphite, rhombohedral graphite, and the newly discovered fullerenes). As is true for organic chemistry, the chemistry and physics of pure carbon is enormously expanded when one considers structures in which carbon is in more than one hybridization state. We have previously predicted structure-property relationships for a high thermal stability carbon phase which contains a mixture of sp^2 and sp carbon atoms [1]. This carbon phase, called graphyne, is presently the target of synthetic effort. Also, various high energy carbon phases have been proposed [2-7]. While carbon is known to exist in forms containing mixed states of carbon hybridization, all such well established forms are largely amorphous.

The family of carbon phases which we have constructed are called carbophanes, because of the similarities to the well known carbocyclic hydrocarbon molecules containing covalently bridged aromatic rings, which are called "phanes". These carbon phanes contain mixtures of sp^2 carbons, sp^3 carbons, and in some cases sp carbons. The structures and properties of these carbophanes will be compared with experimental results for (1) a phase or series of phases obtained by hydrostatic compression of graphite [8-14], (2) the crystalline transformation product obtained by rapid quenching of pulse-laser melted diamond [15], and (3) reported carbon phases which are often referred to in the literature as either "carbenes" or "carbynes" [16-19]. The structures are not established for any of these materials.

The high pressure transformation product of graphite which is of interest here was probably first discovered by Aust and Dickamer [8] in 1963, based on the observed increase in the resistivity of compressed graphite at about 15 GPa. However, the reported irreversibility of the phase change differs from the reversibility found in more recent work. Also, the reported x-ray data was later thought to originate from a contaminant [16]. Nevertheless, various investigators have firmly established the existence of a room temperature phase

transition for graphite which begins on increasing pressure to between 9 and 23 GPa. Upon decreasing the pressure to about 2 GPa or less, the new phase has been reported [11,12] to revert to a mixture of hexagonal and rhombohedral graphite. Electrical conductivity, optical reflectivity, and x-ray diffraction indicate that the high pressure phase is a crystalline insulator or a large bandgap semiconductor having low reflectivity between 1 and 3 eV [8-12]. This low reflectivity indicates that the interband absorption which occurs below 3 eV in graphite has been eliminated [10,13]. Also, the shear strength (determined by measuring pressure gradients and sample thickness in a diamond cell) is reported to exceed that of corundum and rhenium at 20 GPa, which is indicative of three-dimensional covalent bonding [11]. On the other hand, aromatic-like bonding is also suggested for the high pressure phase by Raman measurements at pressures between 38 and 55 GPa, which show a 100 cm^{-1} width peak centered at 1670 cm^{-1} [13]. However, other researchers report that the Raman spectrum could not be detected above 14 GPa [9]. Despite the width of this Raman line, the observation of at least three crystalline diffraction lines indicates that the transparent high pressure phase is not amorphous [11,12]. Structural models are herein proposed which provide electrical, optical and mechanical properties consistent with those observed. These carbophanes consist of covalently bonded sheets of carbon which contain aromatic rings that are isolated by sp^3 carbons. These structures are consistent with both the observed Raman line at about 1670 cm^{-1} , the low reflectivity between 1 and 3 eV, and the low conductivity. On the other hand, a high shear strength is provided by intersheet linkages via the sp^3 carbon atoms.

The experimental results reported for the carbyne phases are often contradictory and the initial structural assignment to linear chains of sp carbon atoms has added to the confusion [16-19]. There are several reasons why the above investigations are controversial. First, the reported properties of carbynes diverge from those predicted for chains of sp carbon atoms. These properties include, in specific instances, diamond-like hardness, a nonfibular morphology, colorless appearance, relatively high density, and high thermal and chemical stability. Second, atomic coordinates have not been produced which provide a satisfactory explanation for reported unit cell dimensions and diffraction intensities. This problem is understandable, since the derived unit cells are rather large and the only available diffraction data is either x-ray diffraction on polycrystalline and inhomogeneous material or electron diffraction data on very small crystallites which are in a matrix of another material. Third, it is not always clearly established that the investigated crystalline phase component contains only carbon. This problem is exaggerated for synthetic routes which are claimed to produce new carbon phases from organic polymer precursors. Moreover, most of the structural characterization is by electron diffraction, which can be misleading in that highly crystalline minority phase components due to impurities can be highlighted. In fact, Smith and Buseck [20] have assigned phase components attributed by others to carbon to a variety of non-carbonaceous phases. This assignment has been contested and it is presently difficult to decide which of the results reported in the literature is an artifact and which is correctly assigned to a new phase of carbon. The reported carbyne phases of interest here are hexagonal with unit cell parameter (a) in the basal plane in the range of 4.76 - 5.45 Å (or a factor of $\sqrt{3}$ higher) and an orthogonal cell dimension of either ~7.5, ~10, ~12.5, or ~15 Å [16-19]. The reasonable consistency of the a-axis dimension, as well as the systematic

variation in the c-axis dimension, suggest polytypic structures. These facts, as well as the continuing reports from diverse laboratories over three decades, suggests that the results are not all artifacts due to impurity components.

II. Description of Carbophane Polytypes:

The basic structural motif of the carbophanes is a covalently bonded layer having the same intralayer connectivity as graphite. In other words, carbon layers in the carbophanes consist of a two-dimensional array of six membered rings. However, in contrast with graphite, these layers in the benzenoid carbophanes consist of a mixture of sp^3 carbons in rings having the hybridization of 1,4-hexadiene and sp^2 carbons which are simultaneously in both these rings with the sp^3 carbons and in benzene rings. Transformation of 1/4 of the sp^2 carbons of graphite to sp^3 carbons, so that the remaining sp^2 carbons are all in benzene rings and no sp^3 carbons are adjacent in a layer, provides the benzenoid carbophanes. Each sp^3 carbon atom is covalently bonded within the layer to an sp^2 carbon in each of three benzene rings. The remaining covalent bond to each sp^3 carbon provides a covalent interlayer bond. In the case where the covalent bonds between layers are to the same neighboring layer, a bilayer structure results in which bonding between alternating layers is non-covalent. More interesting and diversified structures result when each layer containing the hexagonal rings is covalently bonded to two neighboring layers - thereby providing three-dimensionally covalently bonded structures in which there is one interlayer covalent bond to every fourth carbon atom in the hexagonal ring layer. Examples of the hydrocarbon cyclophanes, which are structurally related to the present carbophanes, are shown in Figure 1.

The carbophane phases are categorized according to the direction of intersheet sp^3 - sp^3 bonds for the fundamental structural motif, which is an aromatic ring surrounded by six sp^3 carbons (Figure 2). If a total of n sp^3 carbons bonded to a particular ring provide sp^3 - sp^3 bonds to the same neighboring sheet, a total of n indices denote the configuration of sp^3 - sp^3 bonds about this ring. These indices correspond to that of a ring carbon to which the associated sp^3 carbons are bonded. Correspondingly, there are seven motif isomers possible: 1,2,3,4,5,6-carbophane for $n = 6$; 1,2,3-carbophane, 1,3,5-carbophane, and 1,2,4-carbophane for $n = 3$; 1,2-carbophane, 1,3-carbophane, and 1,4-carbophane for $n = 2$; and 1-carbophane for $n = 1$. An example of a hexagonal ring sheet formed using the 1,3,5-carbophane motif is shown in Figure 2.

It is easily shown that the 1,2-, 1,4-, 1,2,3-, and 1,2,4-carbophane structures are unique. By unique we mean that there is only one way to covalently interconnect these motifs in a single motif structure. Also, the 1,3,5-carbophane has a type of uniqueness, since there is only one possible way to covalently interconnect the 1,3,5 motif, so as to provide the hexagonal ring sheet. However, these hexagonal sheets can be covalently interconnected with a neighboring sheet in two different ways, one which results in eclipsed aromatic rings, and one which results in non-eclipsed aromatic rings. These structures are named eclipsed 1,3,5-carbophane (or e-1,3,5-carbophane) and staggered 1,3,5-carbophane (or s-1,3,5-carbophane), respectively. Various mixtures of eclipsed and staggered sheets can be used to construct an infinite variety of either ordered or disordered forms of 1,3,5-carbophane which

contain basically the same structure for each hexagonal ring sheet. The structures for e-1,3,5- and s-1,3,5-carbophane viewed parallel to the molecular plane are shown in Figures 3 and 4, respectively.

In contrast with these types of uniqueness, there are an infinite number of possible ways (both periodic and non-periodic) to form covalent connections within the ring sheets using exclusively either the 1,3-carbophane or the 1-carbophane motif. Of the single motif structures, a structure with staggered (i.e. non-eclipsed) aromatic rings is possible only for 1,3,5-carbophane and 1-carbophane. Such structures are of special importance because of decreased strain energy compared with the corresponding fully eclipsed structures. As will be described elsewhere, partially staggered structures can arise for carbophanes having mixed motifs, such as an array of 1,3 and 1,3,5 motifs, where every layer can be either eclipsed on both sides or staggered on one side and eclipsed on the other. Note also that only the 1,3,5-carbophane and 1-carbophane structure could transform to diamond without the breaking of already formed covalent bonds. In such a manner, e-1,3,5-carbophane could transform to hexagonal diamond (Lonsdalite) and s-1,3,5-carbophane could transform to cubic diamond. All of the other above mentioned benzenoid carbophanes could transform to a fully sp^3 structure without bond breaking only by formation of energetically unfavorable cyclobutane rings.

There is another type of single-motif benzenoid carbophane structure which is possible, but this structure (which is analogous to the organic "superphane" shown in Figure 1) does not provide a three dimensionally covalently bonded structure. In this structure, which is denoted 1,2,3,4,5,6-carbophane, all intersheet sp^3 - sp^3 bonds from one sheet are connected to the same neighboring hexagonal ring sheet. These bilayers are bound with neighboring bilayers on either side by exclusively non-covalent interactions. Correspondingly, sheets of normal graphite planes could interdisperse with the bilayers, so as to provide an infinite variety of polytypic structures. From the viewpoint of close-packing, such polytypic structures would be expected to be thermodynamically unstable with respect to phase separation of the graphite sheets to make a pure graphite phase. However, such phase separation would be extremely unfavorable, kinetically.

III. Calculation of Crystal Structures and Strain Energies:

We have used the crystal building capabilities of the software program PolyGraf [21] and a modified Dreiding force field [22] to generate energy minimized unit cell parameters and atom coordinates for the simplest members of the carbophane family of phases. The Dreiding force field was modified to reproduce the known structures for a series of organic cyclophanes [27-29] shown in Figure 1. Note that the present force field provides sp^2 - sp^2 bond lengths and force constants appropriate for an isolated aromatic ring, as in a benzenoid carbophane (with a π -bonding order of 1/2 per bond). Consequently, the intralayer bond distances which are predicted for graphite are too short (the π -bond order in graphite is 1/3) and the calculated density of graphite is correspondingly too high, although the graphite interlayer distance is correctly predicted by our force field. The present calculation does not take into account changes in π -bond order in the aromatic rings due to ring distortion, which might provide contributions from quinoid-like structures.

The present crystal structure calculations for carbophane phases provide enthalpies (H_1) relative to a hypothetical reference state in which the terms in the calculation Hamiltonian are zero. The standard heat of formation of a carbophane is obtained by adding the above energy H_1 (which is largely a strain energy) to the energy of the reference state for a carbophane (relative to graphite), which is denoted H_0 . H_0 is calculated using experimentally derived heats of formation of model hydrocarbon molecules which contain an sp^3 carbon atom covalently bonded to three sp^2 carbon atoms in benzene rings and to an sp^3 carbon, as in carbophane. This is done by first using the molecular mechanics force field to calculate the strain energies (H_1) for the model compounds. Using this strain energy and the experimentally derived gas phase heats of formation, $H_f(g)$, for a model compound, H_0 for the model compound becomes $H_0 = H_f(g) - H_1 - 4RT$, where the term $4RT$ corrects for the enthalpy contributions due to rotational and translational motion ($3RT$) and the difference between constant volume and constant pressure gas phase heat capacities (RT).

Using this approach, H_0 for the family of carbophanes was calculated as follows: $H_0(\text{carbophane}) = 1/4 H_0(1,1,1\text{-triphenylethane}) - 1/8 H_0(\text{ethane}) - 5/8 H_0(\text{benzene})$. Using gas phase formation enthalpies for these hydrocarbons reported in the literature [30,31], the resulting value of H_0 for the reference state of a benzenoid carbophane is 0.85 kcal/mole carbon.

If we approximate the effective bond energy of an sp^2 - sp^3 bond as the average of sp^2 - sp^2 and sp^3 - sp^3 bonds, a second estimate for H_0 of benzenoid carbophane can be obtained from the heat of formation of diamond [32] and the gas phase heats of formation of benzene and biphenyl [31]. The equation for H_0 of carbophane is then: $H_0(\text{carbophane}) = 3/8 H_0(\text{biphenyl}) - 5/8 H_0(\text{benzene}) + H_0(\text{diamond})$. The resulting value of H_0 is -0.94 kcal/mole carbon, which is somewhat lower than the above value of +0.85 kcal/mole carbon. Which value is more reliable cannot presently be determined, since the former calculation contains an uncertainty due to the required estimation of the heat of sublimation of the triphenylethane [30], using group increments, and the latter value is uncertain because of the above bond-energy approximation. Although these values of H_0 are both close to zero, the uncertainties in H_0 limit our ability to calculate equilibrium transition pressures for the interconversion between graphite and the carbophanes.

IV. Properties Evaluation:

Based on experimental observations for multilayered organic benzenoid cyclophanes, the present benzenoid carbophanes are expected to be colorless. For example, Otsubo et al. [33] investigated the effect of layer number on the optical properties of [2.2]paracyclophanes having from 2 to 6 layers. The two layer form of this compound is shown in Figure 1. With increasing layer number, strong bathochromic and hyperchromic changes are observed in the ultraviolet absorption spectra. However, these effects rapidly saturate, so that little change is observed in going from a five layer to a six layer [2.2]paracyclophane, both of which form colorless crystals. Similarly, both fluorescence and phosphorescence spectra exhibit large bathochromic shifts

and the phosphorescence lifetime decreases with increasing layer number. Also, the charge-transfer complexes with acceptors, such as tetracyanoethylene or trinitrobenzene, demonstrate bathochromic shifts of the long wavelength charge-transfer band and an increased association constant for increasing numbers of layers in the paracyclophanes. These shifts in optical properties with increasing number of layers, which are close to saturation for six layer [2.2]cyclophane, largely arise from interlayer π -electron interactions between neighboring aromatic rings. Based on the similar optical properties of unsubstituted cyclophanes and cyclophanes with severe aromatic ring distortions due to eclipsed methyl substituents (as well as the absence of large shifts in the absorption curves for [m]cyclophanes having aromatic ring strain similar to the [2.2]paracyclophanes [34]), the optical property changes due to aromatic ring distortions are expected to be relatively unimportant [33].

The above observations on the multilayered organic benzenoid cyclophanes also suggest that the corresponding eclipsed benzenoid carbophanes with three-dimensional covalent bonding will display red shifts in absorption, fluorescence, and phosphorescence spectra (and a decrease in phosphorescence lifetimes) with decreasing interlayer separation, due to increased π -electron interactions in the stacks of aromatic rings. The decreased phosphorescence lifetime is expected to be a result of a lowering of the energy gap between ground and triplet states as a result of increasing interactions between benzene rings. More specifically, using observations on the stacked [2.2]paracyclophanes [33], an absorption onset at about 3.3 eV, a fluorescence maxima at about 390 nm, and a phosphorescence maxima at about 530-570 nm are expected for an eclipsed carbophane having a spacing between aromatic ring carbons of about 2.97 Å. Such spacings are in the range predicted for carbophanes. A blue shift in these spectra and an increased phosphorescence lifetime is expected for the eclipsed carbophanes in Table 1 having longer interlayer separations, while those eclipsed carbophanes having shorter interlayer separations are expected to behave in the opposite manner. Pressure will decrease the interlayer spacing and produce the corresponding effects on the electronic states.

Note that the calculated densities for the carbophanes in Table 1 range from 2.479 g/cm³ for s-1-carbophane to 2.801 g/cm³ for e-1,3,5-carbophane. The calculated densities of these phases are intermediate between those of hexagonal graphite ($\rho(\text{obs.})=2.267$ g/cm³) and diamond ($\rho(\text{obs.})=3.52$ g/cm³ and $\rho(\text{calc.})=3.502$ g/cm³). Excluding the highest density phases (e-1,3,5-carbophane and s-1,3,5-carbophane), the calculated strain energies of the carbophanes are represented within a maximum deviation of 0.24 kcal/mole by a linear dependence on calculated density ($H_1 = -20.32 + 9.26 \rho$). Staggered 1,3,5-carbophane has a 0.56 kcal/mole lower strain energy and eclipsed 1,3,5-carbophane has a 0.65 kcal/mole higher strain energy than provided by this linear correlation. Consequently, the s-1,3,5-carbophane phase is especially interesting as a phase which might be thermodynamically stable with respect to graphite at high pressure. Note that this phase shows a large density increase with respect to the density of graphite, while requiring a smaller than expected formation energy with respect to graphite at zero pressure. Although increasing the temperature will decrease the formation free energy of a carbophane relative to diamond, because of entropy contributions, diamond will

have a lower free energy than any carbophane phase at room temperature and any pressure.

Calculated bulk moduli for carbophanes and for diamond are also listed in Table 1. Using the modified Dreiding force field, a bulk modulus of 477 GPa is obtained for diamond, as compared with a measured value of 442 GPa [35]. Staggered-1,3,5-carbophane has the highest calculated bulk modulus and the highest bulk density of all the benzenoid carbophanes studied. The bulk modulus of s-1,3,5-carbophane is 240 GPa, which is 54% of the observed modulus of diamond and 7.1 times the observed [9] bulk modulus of graphite (33.8 GPa). Since 1,2,3,4,5,6-carbophane does not have three-dimensional covalent bonding, but instead consists of bilayers which are connected to neighboring bilayers by exclusively non-covalent bonding, a bulk modulus of about twice that of graphite is expected for this phase. Consistent with this view, the ratio of the calculated bulk modulus for 1,2,3,4,5,6-carbophane to the observed bulk modulus for graphite is 2.2.

V. Conclusions:

A carbophane phase provides an interesting model for the room temperature, high pressure transformation product of graphite (HP phase). A number of points provide support for such a model. First, the HP phase is reported to revert to a mixture of hexagonal and rhombohedral graphite upon a reduction in pressure at room temperature [11-12], which would appear to exclude assignment as a polytype of diamond. While the carbophanes are expected to have a considerable degree of kinetic stability at zero pressure, defects (due to imperfect phase transformation, for the ambient temperature formation process) could propagate as molecular scale cracks upon the unloading of pressure, thereby facilitating the reversion to graphite. Second, formation of carbophanes is expected to be kinetically favorable, since no covalent bond breaking is required to transform graphite to a carbophane and a lower degree of cooperative reaction is required than to form a diamond polytype. Third, eclipsed carbophanes are predicted to be transparent up to about 3.3 eV and staggered carbophanes are probably transparent to an even higher energy. This is consistent with the reported bleaching of the interband transition of graphite below 3 eV in going to the HP phase [10,13]. Fourth, the carbophanes would provide a Raman peak (corresponding to the aromatic ring mode) close to that observed for the HP phase, since the in-plane ring stretch occurs in the 1620-1565 cm^{-1} region at atmospheric pressure for various cyclophanes [36]. Fifth, the carbophanes, such as s-1,3,5-carbophane, are calculated to have a bulk modulus which is up to 50% that of diamond, consistent with the report that the HP phase is a superhard material with a strength comparable to diamond [11].

Regarding the possibility that carbophanes might have been already observed at ambient pressure, but unrecognized as such, it is interesting to note that Weathers and Bassett [15] have reported that new crystalline carbon phases are produced as microscopic components by pulsed-laser melting of diamond at high pressures in a diamond anvil cell. As the pressure during the laser pulse is increased from 10 to 30 GPa, the long diffraction spacing observed for the transformation product decreases from 3.4 Å, as in graphite, to 2.8 Å. As shown in Table 1, this is about the range of intersheet spacings which we have

derived for three-dimensional carbophane phases (from 3.17 Å for 1,2,3-carbophane to 2.72 Å for s-1,3,5-carbophane). Additionally, it is interesting to note that the carbophanes provide the diamond-like hardness, non-fibular morphology, colorless appearance, and relatively high density that researchers have attributed to the mysterious carbyne phases [16-19]. Also, if these phases are well ordered, they could provide the high thermal and chemical stability which has been claimed for the carbynes. The directly bridged carbophanes described herein do not provide the acetylenic bond, which is the claimed component of carbynes [16-19]. The evidence for such bonds in the crystalline phase is not firmly established, because of the possibility that the spectroscopic signature for their type of bonding is from the matrix. Nevertheless, acetylene-containing polytypes can be readily constructed from the present carbophane phases by replacing sp^3 - sp^3 interlayer bridges with sp^3 - $sp \equiv sp$ - sp^3 linkages for either a fraction or for all of the interlayer separations. We have shown that the resulting unit cell parameters reproduce reasonably well those in the literature of carbynes [16-19].

This is an interim report of continuing work on what we believe to be an important family of new carbon phases. Work in progress will extend the carbophane family of phases to mixed motif and disordered variants, refine and extend property predictions, and provide comprehensive comparisons of predicted properties with those reported in the substantial literature which claims new crystalline carbon phases. It will also be interesting to see whether or not the fundamental packing arrangements in the carbophanes provide a useful framework for structural models of "amorphous" diamond-like carbon. These materials are known to consist of mixtures of sp^3 and sp^2 hybridized carbons.

References

1. R. H. Baughman, H. Eckhardt, and M. Kertesz, *J. Chem. Phys.* **87**, 6687 (1987).
2. M. T. Yin and M. L. Cohen, *Phys. Rev. Lett.* **50**, 2006 (1983).
3. K. M. Merz, R. Hoffmann, and A. T. Balaban, *J. Am. Chem. Soc.* **109**, 6742 (1987).
4. G. Laqua, H. Musso, W. Boland, and R. Aldrichs, *J. Am. Chem. Soc.* **112**, 7391 (1990).
5. M. A. Tamor and K. C. Hass, *J. Mater. Res.* **5**, 2273 (1990).
6. A. T. Balaban, C. C. Rentia, and E. Ciupitu, *Revue Roumaine de Chimie* **13**, 231 (1968).
7. R. Hoffman, T. Hughbanks, M. Kertesz, and P. H. Bird, *J. Am. Chem. Soc.* **105**, 4832 (1983).
8. R. B. Aust and H. G. Drickamer, *Science* **140**, 817 (1963).
9. M. Hanfland, H. Beister, and K. Syassen, *Phys. Rev. B* **39**, 12598 (1989).
10. M. Hanfland, K. Syassen, and R. Sonnenschein, *Phys. Rev. B* **40**, 1951 (1989).
11. J. F. Shu, H. K. Mao, J. Z. Hu, Y. Wu, and R. J. Hemley, *Bull. Am. Phys. Soc.* **36**, 479 (1991).
12. Y. X. Zhao and I. L. Spain, *Phys. Rev. B* **40**, 993 (1989).
13. A. F. Goncharov, I. M. Makarenko, and S. M. Stishov, *High Pressure Research* **4**, 345 (1990).
14. A. A. Goncharov, *Zh. Eksp. Teor. Fiz.* **98**, 1824 (1990).

15. M. S. Weathers and W. A. Bassett, *Phys. Chem. Minerals* **15**, 105 (1987).
16. L. I. Man, Y. A. Malinovskii, and S. A. Semiletov, *Sov. Phys. Crystallogr.* **35**, 608 (1990).
17. A. G. Whittaker and P. L. Kintner, *Science* **165**, 589 (1969).
18. R. B. Heimann, J. Kleiman, and N. M. Salansky, *Carbon* **22**, 147 (1984).
19. A. M. Sladkov, *Soviet Sci. Rev. Sec. 3*, 75 (1981).
20. P. K. Smith and P. R. Buseck, *Science* **216**, 986 (1982).
21. PolyGraf is an interactive molecular simulation/three-dimensional graphics program from Molecular Simulations, Inc., Sunnyvale, CA, 94086.
22. The following adjustments were made in the Dreiding force field [23]. The van der Waals interactions were treated with an exponential-six potential with parameters for hydrogen ($R_0=3.1665$ Å, $D_0=0.0200$ kcal/mole, and $\zeta=11.2$) and carbon ($R_0=3.8410$ Å, $D_0=0.07918$ kcal/mole, and $\zeta=13.0$) [24]. A Morse potential was used for bond stretching with $B_0(\text{sp}^3\text{-sp}^3)=1.525$ Å, $B_0(\text{sp}^3\text{-sp}^2)=1.500$ Å, and $B_0(\text{sp}^2\text{-sp}^2)=1.375$ Å. A theta expansion was used for the angle bending term with $\Theta_0(\text{sp}^3\text{-sp}^3\text{-sp}^2)=112.0^\circ$. The Dreiding force field uses a six-fold torsion term with a barrier height of 1.0 kcal/mol, and a *cis* max for rotation about an sp^3 carbon bonded to an aromatic ring. We were better able to reproduce the barriers for rotations reported by Schaefer et al. for ethylbenzene [25] and isopropylbenzene [26] if this term was set equal to zero.
23. S. L. Mayo, B. D. Olafson, and W. A. Goddard, III, *J. Phys. Chem.* **94**, 8897 (1990).
24. N. Karasawa, S. Dasgupta, and W. A. Goddard, III, *J. Phys. Chem.* **95**, 2260 (1991).
25. T. Schaefer, G. Penner, and R. Sebastian, *Can. J. Chem.* **64**, 873 (1986).
26. T. Schaefer, R. Sebastian, and G. Penner, *Can. J. Chem.* **66**, 1945 (1988).
27. H. Hope, J. Bernstein, and K. N. Trueblood, *Acta Cryst.* **B28**, 1733 (1972).
28. A. W. Hanson, *Cryst. Struct. Comm.* **9**, 1243 (1980).
29. A. W. Hanson and T. S. Cameron, *J. Chem. Research (S)* 336 (1980).
30. R. M. Joshi, *J. Macromol. Sci., Chem.* **A5**, 687 (1971).
31. D. R. Stull, E. F. Westrum, Jr., and G. C. Sinke, *The Chemical Thermodynamics of Organic Compounds*, Sec. III, pp. 631-769 (Wiley, New York, 1969).
32. P. Hawtin, J. B. Lewis, N. Moul, and R. H. Phillips, *Proc. Soc. London A* **261**, 67 (1966).
33. T. Otsubo, S. Mizogami, I. Otsubo, Z. Tozuka, A. Sakagami, Y. Sakata, and S. Misumi, *Bull. Chem. Soc. Jap.* **46**, 3519 (1973).
34. N. L. Allinger, L. A. Freiberg, R. B. Hermann, and M. A. Miller, *J. Am. Chem. Soc.* **85**, 1171 (1963).
35. M. H. Grimsditch and A. K. Ramdas, *Phys. Rev. B* **11**, 3179 (1975).
36. P. H. Scudder, V. Boekelheide, D. Cornutt, and H. Hopf, *Spectrochimica Acta* **37A**, 425 (1981).

Table 1. Calculated Structural Features of Carbon Phases

Carbon Phase	Space Group	Density g/cm ³	Z ^a	H ₁ (strain) (kcal/mol)	Interlayer Spacing, Å	Bulk Modulus (GPa)
s-1-carbophane	P $\bar{3}$ 1m	2.479	48	2.398	3.074	101
e-1-carbophane	P $\bar{6}$ 2m	2.672	48	4.345	2.926	135
	Cmcm	2.672	64	4.367	2.924	129
1,2-carbophane	Cmcm	2.547	64	3.376	3.125	109
1,3-carbophane	Cmcm	2.737	64	5.128	2.853	192
	P $\bar{6}$ 2m	2.733	48	5.104	2.858	191
1,4-carbophane	Immm	2.722	32	4.862	2.884	199
1,2,3-carbophane	Imma	2.514	32	3.205	3.169	106
1,2,4-carbophane	Cmca	2.707	64	4.573	2.903	195
s-1,3,5-carbophane	R $\bar{3}$ m	2.840	24	5.418	2.724	240
e-1,3,5-carbophane	P $\bar{6}$ ₃ /mmc	2.801	16	6.271	2.775	238
1,2,3,4,5,6-carbophane	P6/mmm	2.636	16	4.190	2.672 ^b 3.226 ^c	75
	P $\bar{6}$ ₃ mmc	2.405	4	-0.007	3.355	43
graphite	R $\bar{3}$ m	2.402	2	0.010	3.355	
	Fd $\bar{3}$ m	3.502	8	0.992	2.059 ^d	477
diamond	P $\bar{6}$ ₃ /mmc	3.490	4	2.591	2.180 ^e	473

^a Atoms per unit cell. ^b Distance between covalently bonded layers. ^c Distance between van der Waals bonded layers. ^d (111) spacing. ^e (100) spacing.

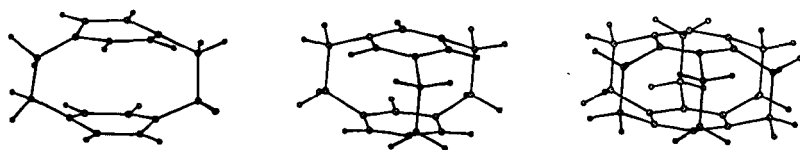


Figure 1. Organic cyclophanes which contain the intersheet bonding arrangement of 1,4-carbophane, 1,3,5-carbophane, and 1,2,3,4,5,6-carbophane.

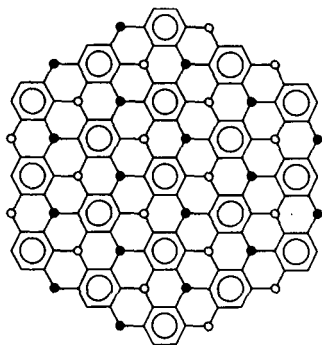


Figure 2. The bonding arrangement for e and s-1,3,5-carbophane showing the six sp^3 carbons surrounding each aromatic ring. Open and closed circles indicate sp^3 bonding below and above the layer plane, respectively.

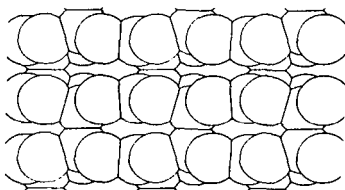


Figure 3. The crystal structure for e-1,3,5-carbophane viewed normal to the intersheet sp^3 - sp^3 bond and parallel to the sheet plane.

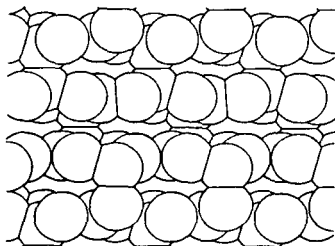


Figure 4. The crystal structure for s-1,3,5-carbophane viewed normal to the intersheet sp^3 - sp^3 bond and parallel to the sheet plane.

High Temperature Raman Scattering Behaviour in Diamond

Harald Herchen and Mark A. Cappelli
High Temperature Gasdynamics Laboratory
Stanford University
Stanford, CA 94305-3032

Keywords: Diamond, First-order Raman

Introduction

The Raman spectrum of synthetic carbon films is now routinely used as an identification of the phase or measure of the quality of such films, when compared to that of natural diamond or natural and synthetic graphite.¹ Since the development of CVD diamond technology, the width and relative shift of the first-order Raman transition of polycrystalline diamond has been used to qualitatively ascribe the amount of disorder² (inhomogeneous strain) or homogeneous strain³ in these new materials. In diamond, the lattice dynamics that give rise to the Raman effect are also responsible for determining the thermal properties such as specific heat and thermal conductivity. The variation with temperature of the first-order Raman mode in polycrystalline diamond in comparison to that of natural diamond can therefore be used as an additional qualitative check on the high temperature behaviour of the thermal properties of these films.

The temperature variation of the first-order Raman spectrum in natural diamond was first investigated by Nayar⁴ in 1941 in an attempt to better understand the relationship between the observed shift and measured thermal expansion coefficients. A similar but more extensive study was performed by Krishnan.⁵ In both cases, the highest temperature achieved (about 1100 K) was limited by diamond contamination and thermal emission, which contributed to background interference. Recently, Herchen and Cappelli⁶ extended these measurements to about 1900 K, using gated photon counting and either modulated or pulsed laser excitation sources. In this paper, similar data is presented for free standing 100 μm thick diamond film. The Stokes to anti-Stokes ratio of the first-order Raman spectrum is used to infer the sample temperature. It is found that this temperature is consistent with temperatures measured by optical pyrometry, provided a diamond emissivity of close to unity is used in the analysis. These temperatures are then employed to deduce the variation in the shift and width of the Raman feature with temperature. The results are compared to similar measurements on type IIa natural diamond.

Experiment

The experimental facility is similar to that used in previous studies,⁶ and is only briefly described here. The Raman spectra were obtained by exciting the free standing polycrystalline diamond samples with the 457.94 nm output from an argon-ion laser that was mechanically chopped at 2 kHz. The backscattered light from near-normal incidence was collected with $f/5$ optics and imaged onto the entrance slit of a 1-m scanning monochromator. The dispersed light at the exit slit was detected with a photomultiplier tube and analyzed with photon counting electronics. The spectral resolution was approximately 0.1-nm, and all spectral width measurements were corrected for instrument broadening.

The free-standing polycrystalline diamond used to obtain the results described here was provided by Crystallume Inc.⁷ The thickness of the sample studied was approximately 100 μm and was grown by microwave plasma deposition. It was translucent and grey in appearance partly resulting from the scattering of light at the grain boundaries. The sample was treated for one hour by boiling in 96% sulphuric acid at atmospheric pressure prior to inserting it into a

high vacuum chamber where it was sandwiched between two electrically heated tungsten ribbons (Fig. 1). The chamber had optical access permitting laser excitation and direct measurement of the tungsten and diamond brightness temperatures.

The diamond was not expected to be in thermal equilibrium with the tungsten ribbons, and so each brightness temperature was monitored independently. A disappearing filament pyrometer with a filter centered at 655 nm was used in the measurement of the brightness temperatures. These temperatures can be corrected to the actual temperatures provided that emissivities of the two materials at 655 nm are known. The emissivity of tungsten at that wavelength is well known, however there is no available data on the emissivities of polycrystalline diamond films. Indeed, the values will be highly dependent on surface and growth conditions. Consequently, the Raman Stokes to anti-Stokes intensity ratio was used to arrive at the true diamond temperature, and this together with the measured brightness temperature provided an experimental determination of the sample emissivity.

Results and Discussion

Typical Stokes and anti-Stokes first-order Raman spectra of the free-standing polycrystalline diamond samples at approximately 1200 K brightness temperature are shown in Fig. 2. The nearby argon plasma transition from the laser discharge ($\text{Ar}^+ 4s^2P \rightarrow 4p^2D^o$ line at 487.986 nm) appears at a shift of 1344.7 cm^{-1} and acts as an accurate calibrant for the Stokes shifted diamond component which appears here at 1309 cm^{-1} . The argon plasma spectral line at 433.12 nm is sufficiently close to the anti-Stokes component to provide a similar reference at -1251.2 cm^{-1} . It is evident that both the Stokes and anti-Stokes components are significantly broadened to about 10 cm^{-1} after correction for the instrument broadening. Their widths are nearly twice that observed for natural type IIa diamond at the same temperature.⁶

The Raman Stokes to anti-Stokes intensity ratio

$$\frac{I_{\text{St}}}{I_{\text{a-St}}} = \left(\frac{\omega_{\ell} - \omega_s}{\omega_{\ell} + \omega_s} \right)^4 e^{h\omega_s/kT}$$

can be a direct measure of the sample temperature. Here ω_s is the phonon frequency, ω_{ℓ} is the line center frequency of the laser excitation source, T is the sample temperature, and h and k are the Planck and Boltzmann constants, respectively. Figure 3 compares the sample temperature derived from the Stokes to anti-Stokes ratio to the tungsten ribbon temperature as measured by optical pyrometry. It is clear from this figure that the sample does not come to thermal equilibrium with the tungsten heaters and is usually 200 to 300 K cooler over the range tested. This difference can be attributed to the thermal contact resistance between the diamond sample and tungsten ribbon heaters and to significant radiative losses due to the high emissivity of this diamond sample. This result further emphasizes the need to directly measure the diamond temperatures during vapor deposition, so as to have a more accurate assessment of the deposition conditions.

The emissivity can be estimated from the temperatures derived from the Stokes to anti-Stokes ratios and the measured diamond brightness temperatures. These are given in Fig. 4. The results suggest emissivities at 655 nm of close to unity, consistent with the visual appearance of the sample. These results are intriguing in that they suggest that polycrystalline diamond coatings may be very useful as high temperature radiative surfaces in circumstances where other properties of such diamond are also advantageous.

The variation in the observed Raman shift with diamond temperature for both the Stokes and anti-Stokes components is shown in Fig. 5. The diamond temperature is found from its brightness temperature and an emissivity of unity. The error in the shift is $\pm 0.3 \text{ cm}^{-1}$ which is less than the size of the symbols used to represent the data points. Also shown in the figure is

a solid line summarizing previously measured values for natural diamond.⁶ The values for the polycrystalline diamond are found to be in excellent agreement with that of natural diamond over the range of temperature studied here. Furthermore, these results are in general agreement with the theoretical molecular dynamics predictions of Wang et al.⁸, a fit through which is shown by a dashed line in Fig. 5.

The variation in the full width at half maximum intensity (FWHM) of the Raman spectrum with temperature (again using the diamond brightness temperature and an emissivity of unity) is shown in Fig. 6. The spectra were corrected for instrument broadening. The spectral lineshapes were found to be well represented by a Voigt profile. The Lorentzian Raman profile was obtained by deconvolving the Gaussian instrument broadening from the measured profiles. The instrument contribution to the FWHM amounted to 3.7 cm^{-1} and 4.7 cm^{-1} for the Stokes and anti-Stokes components, respectively. The solid line in Fig. 6 is a fit to the results obtained for natural diamond.⁶ The high temperature FWHM for the polycrystalline samples are 4 to 6 cm^{-1} greater than that for natural diamond, consistent with room temperature data. Both results however are in reasonable agreement with the predicted FWHM values of Wang et al.⁸ The difference between the measured values of the FWHM for the polycrystalline and natural diamond samples can be attributed to slight disorder in the carbon-carbon bond length (inhomogeneous strain).² An accurate and unambiguous identification of the source of broadening in the first-order Raman spectra requires further experimental and theoretical investigation.

Summary

The data presented here suggest that one can grow polycrystalline CVD diamond that has high temperature Raman scattering characteristics comparable to that of natural diamond. The usefulness of Raman scattering as a possible unambiguous measure of the sample temperatures has been demonstrated. Furthermore, this independent temperature measurement provided the opportunity to make one of the first direct measurements of CVD diamond emissivity. Emissivities approaching unity were obtained, suggesting that CVD diamond could be quite useful as a high temperature radiative coating in chemically harsh environments.

Acknowledgements

The authors would like to thank M. Pinneo of Crystallume for providing the polycrystalline diamond sample studied here. Support for this research was provided by the Office of Naval Research.

References

1. D.S. Knight and W.B. White, *J. Mater. Res.* **4**, 385 (1989).
2. R.G. Buckley, T.D. Moustakas, L. Ye, and J. Varon, *J. Appl. Phys.* **66**, 3595 (1989).
3. M.A. Cappelli, T.G. Owano, C.H. Kruger, *J. Mater. Res.* **5**, 2326 (1990).
4. R.G.N. Nayar, *Proc. Indian Acad. Sci. Sect. A* **13**, 284 (1941).
5. R.S. Krishnan, *Proc. Indian Acad. Sci. Sect. A* **24**, 45 (1946).
6. H. Herchen and M.A. Cappelli, *Phys. Rev. B* (in press).
7. Crystallume Inc., 125 Constitution Ave, Menlo Park, California, 94025.
8. C.Z. Wang, C.T. Chan and K.M. Ho, *Phys. Rev. B* **42**, 11 276 (1990).

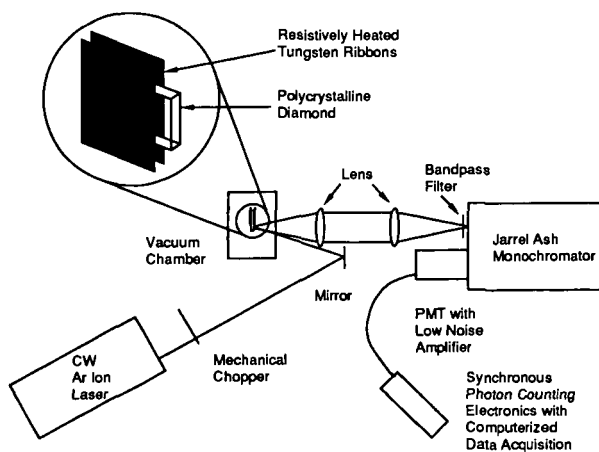


Figure 1. Schematic of the experimental setup for Raman backscattering studies of polycrystalline diamond at high temperature. The inset illustrates the mechanism used to heat and hold the sample.

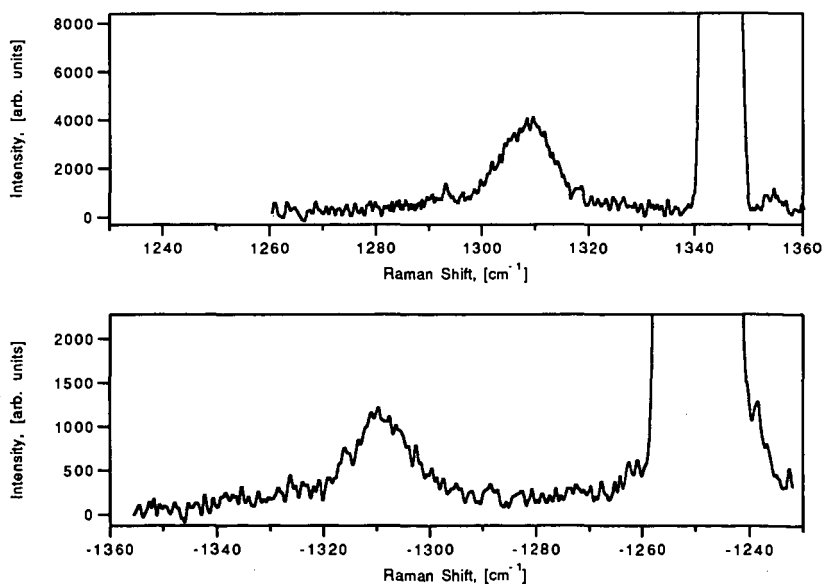


Figure 2. Stokes, top, and anti-Stokes first-order Raman spectra with argon ion emission calibration lines. The diamond temperature was 1200 K.

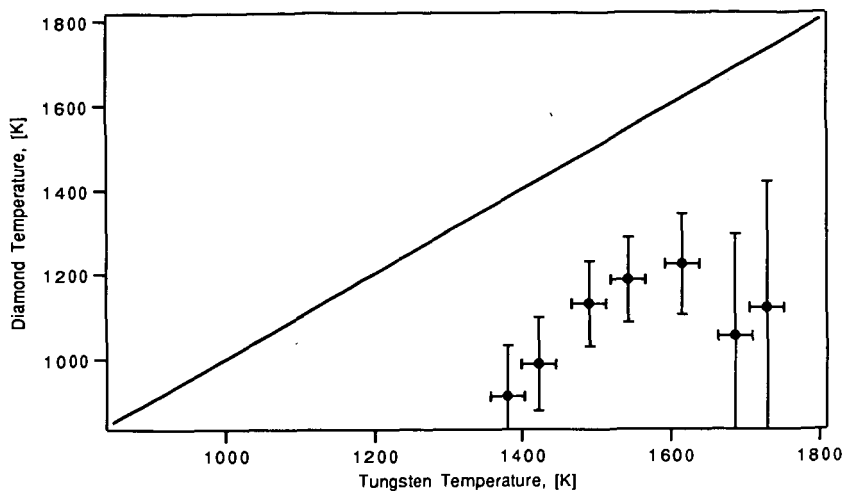


Figure 3. Polycrystalline diamond temperature based on the Stokes to anti-Stokes intensity ratio as a function of the tungsten ribbon temperature. The solid line corresponds to equal diamond and tungsten temperatures.

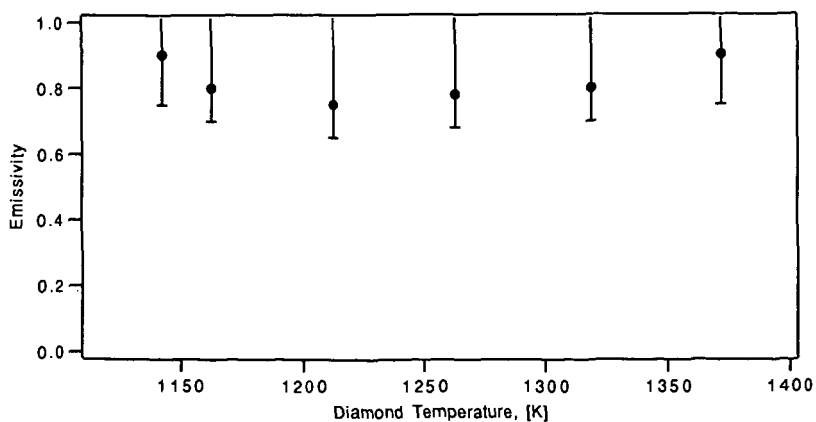


Figure 4. Polycrystalline diamond emissivity at 655 nm determined from the measured brightness temperature and the diamond temperature found from the Stokes to anti-Stokes intensity ratio.

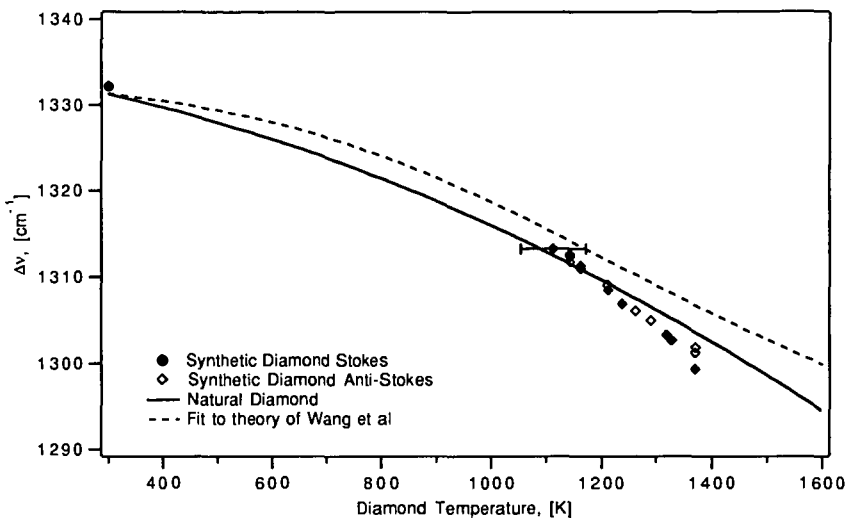


Figure 5. Variation of the first-order Raman shift in polycrystalline diamond with temperature. The diamond temperature is found using an emissivity of unity. The solid line is a fit to the first-order Raman shift for natural diamond (Ref. 6). The dashed line is a fit to the results of molecular dynamics simulation of Wang et al (Ref 8).

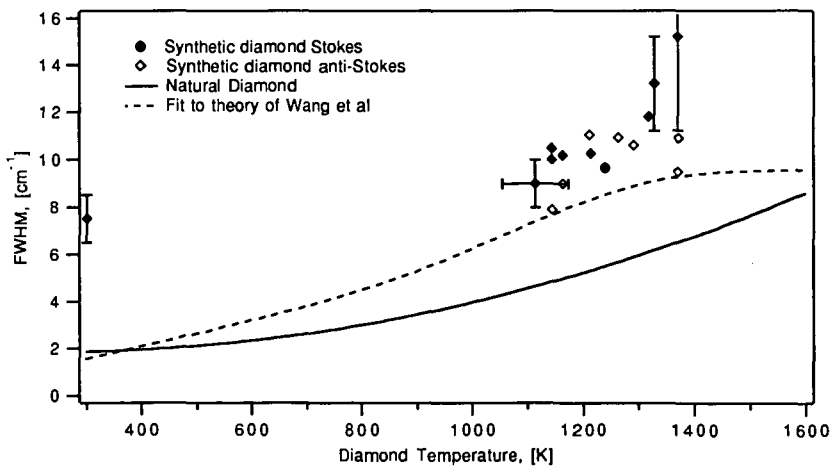


Figure 6. Variation of the full width at half maximum (FWHM) of the first-order Raman spectrum in polycrystalline diamond with temperature. The diamond temperature is found using an emissivity of unity. The solid line is a fit to the FWHM for natural diamond (Ref. 6). The dashed line is a fit to the theoretical results of Wang et al (Ref 8).

HYDROGEN BINDING AND DIFFUSION IN DIAMOND*

S. P. Mehandru and Alfred B. Anderson
Chemistry Department, Case Western Reserve University
Cleveland, OH 44106-7078

and

John C. Angus
Department of Chemical Engineering, Case Western Reserve University
Cleveland, OH 44106

Keywords: hydrogen in diamond, diffusion

INTRODUCTION

The growing interest in the surface and bulk properties of diamond, which are markedly influenced by foreign atoms, is the natural consequence of the evolving technology for low-pressure diamond film and crystal growth.¹⁻⁴ Large hydrogen concentrations are found in natural^{5,6} and man-made diamond, particularly in diamond-like films.⁷ Surface hydrogen is believed to be responsible for low-pressure diamond growth from C₁ and C₂ hydrocarbon fragments, whose identification is under investigation at this time.⁸ During low-pressure growth, hydrogen is essentially a catalyst, maintaining tetrahedral bonding structure at the diamond surface, blocking routes to graphite formation. Bound H atoms are removed by bonding to H atoms from the gas and coming off as H₂. This process momentarily forms active dangling radical orbitals at the surface to which hydrocarbon radicals from the gas bind, in competition with H atoms, ultimately propagating diamond growth. Beyond this, the growth mechanism or mechanisms are not yet understood. We have made model atom superposition and electron delocalization molecular orbital (ASED-MO) studies of the absorption of C₁ and C₂ hydrocarbon species on the diamond (100) and (111) surfaces^{9,10} and have found C₁ species may be able to diffuse on the former surface, but not the latter.

Hydrogen has been rather well studied as an interstitial impurity in silicon, but not in diamond. In silicon it is attracted to substitutional B atoms and poisons their p-dopant properties, affecting the semiconducting properties.¹¹ Recent theoretical works based on quantum mechanical models have shown that an isolated interstitial H atom binds in a Si-Si bond-center site and provides an attractive potential well for second interstitial H to pair with it in an interstitial antibonding site, forming H-Si-H-Si oriented in the [111] direction.¹²⁻¹⁶ For H in diamond, theory has predicted similarly that bond-centered interstitial sites are most stable and a second H is attracted to the antibonding site.¹⁶⁻¹⁹ Infra red (IR) studies of natural diamonds show well-defined stretching and bending excitations at 3107 cm⁻¹ and 1405 cm⁻¹.²⁰⁻²² Recent thermal desorption studies yielded an integrated hydrogen desorption flux of about 10 monolayers of

*Supported by the U. S. National Science Foundation,
Grant No. DMR-03527

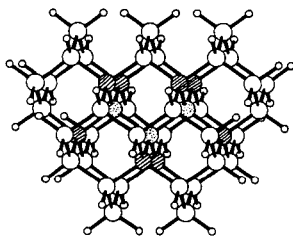
hydrogen between 700 and 1100 K from a polished diamond (1x1) H-covered (100) surface.²³

Standard free energies for alkane formation begin to favor the elements, $C(di)+H_2(g)$, for C_6 and larger, and for all unsaturated hydrocarbon molecules the elements are favored.²⁴ Therefore, it might be expected that sub-surface hydrogen will be released as H_2 . Single bonds between carbon atoms and H_2 single bonds are replacing CH bonds. However, the details of the subsurface H bonding are not known. Interstitial H atoms are likely to be bound weakly as is the case for Si. The release of such H as gas phase H_2 should be very stabilizing and the question of its rate is a kinetic one. If C vacancies exist and H binds to the carbon atoms surrounding these vacancies, and this would be a plausible explanation for the bending and stretching modes seen by IR, then such H would be rather strongly bound. Muon-spin-rotation (μ SR) studies have shown that at temperatures greater than 800 K the +1-charged muon nuclei are in an anisotropic environment,²⁵ which might correspond to such a site. The loss of H, as H_2 following combination with a second vacancy-bound H, would not be stabilizing unless there is massive restructuring which forms C-C bonds and removes the vacancies, since a single H_2 bond would be replacing 2 CH bonds. Whether subsurface vacancies might have several weakly bound H atoms squeezed into them is unknown. Such H might be partially released without the need for restructuring.

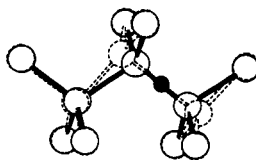
With the above questions in mind, along with what is already known about H in silicon, we have undertaken an ASED-MO study of H atom interstitial and vacancy bonding and diffusion in diamond. We explain our results in terms of the orbital and electronic structures and speculate on the possible effects of p-type dopants. The atomic parameters are those used in the earlier ASED-MO diamond surface work.^{9,10}

INTERSTITIAL H AND ITS MIGRATION

Our C_{46} diamond structure cluster model is terminated by 48 CH bonds to eliminate surface radical orbitals with energies in the band gap, which would interfere with our bulk property calculations. Its structure is shown in 1, with 3 shaded atoms being those relaxed around interstitial H in bond-centered sites, which are calculated to be the most stable interstitial locations, and the hatching identifies the second shell of atoms which were also relaxed in the calculations.

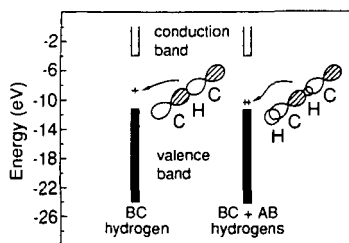


1

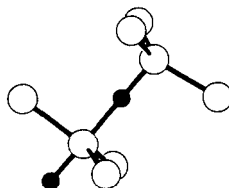


2

Rather severe distortions take place to accommodate the bond-centered interstitial H atom, shown black in 2. The interstitial H atom is unstable relative to the free atom by 1.7 eV. The C-C stretching caused by H insertion lowers a localized σ^* orbital from the conduction band into the band-gap as shown in 3, thus stabilizing the radical electron. The band gap orbital has a node at H and the 3-centered C-H-C σ bonding orbital is dispersed in the valence band. It may be expected that a p-type dopant atom, such as B, will stabilize the promoted electron in the band-gap orbital and then interstitial H atoms will be attracted to the vicinity of the dopant atom, as for Si.¹⁵ This will destroy the p-dopant electrical properties of diamond. A second H binds at the antibonding site as shown in 4 1.4 eV more strongly than the first H in the bond-centered site. The second radical electron pairs with the first in



3

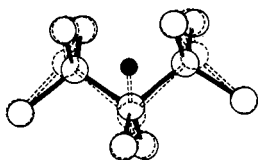


4

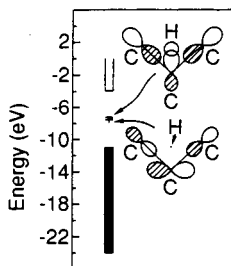
the band-gap orbital, which is stabilized due to overlap between it and the H 1s orbital in the antibonding site as shown in 3. It is expected therefore that p-type dopants will attract a second, and perhaps a third, interstitial H atom.

In the presence of H in the interstitial antibonding site, the bond-centered CH vibrational excitation energy, based on the vibrational force constant in a local-mode approximation, is calculated to be $\sim 1600 \text{ cm}^{-1}$ greater than that calculated in the same way for a CH bond in methane. For the antibonding H it is $\sim 1000 \text{ cm}^{-1}$ greater. Some high-energy vibrational excitations have been observed by IR²² but they match bending overtones and a stretch-bend combination for an isolated, perhaps vacancy, CH bond rather well. Consequently, the concentration of interstitial CH is probably relatively low. An isolated bond-centered interstitial H would, for symmetry reasons, be IR inactive.

An isolated bond-centered interstitial H will migrate to an adjacent bond-centered site by passing through a transition state with the structure shown in 5. The calculated energy barrier is 1.9 eV. Since in the transition state two C-C bonds are stretched, two σ^* orbitals from the conduction band drop into the band gap as shown in 6 and the lower one is C-H non-bonding. This orbital, which takes the promoted electron, is 1.2 eV above the occupied band-gap orbital for the bond-centered site and contributes this much to the H migration barriers. Thus, it is expected that p-dopant atoms will decrease energy barrier for interstitial H atom migration in their vicinity.



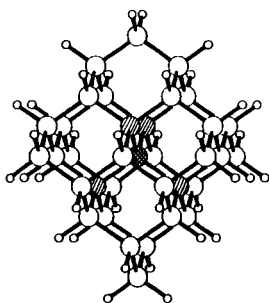
5



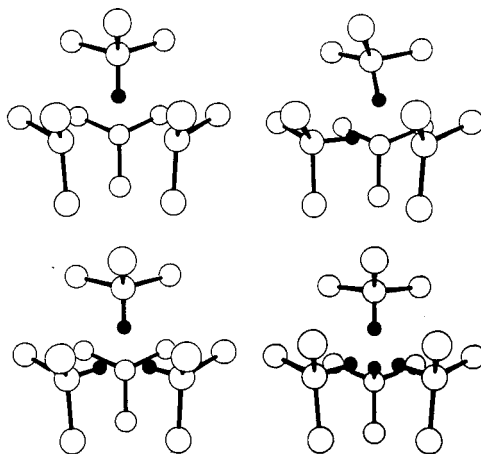
6

BINDING OF H ATOMS TO A VACANCY

A vacancy is modeled by removing the cross-hatched atom in 7 and relaxing the hatched atoms. The calculated vacancy formation energy, based on placing the removed C atom on a 3-fold (111) surface site, is calculated to be 6.0 eV. A slight tetragonal distortion, which removes the degeneracy of the doubly occupied t-symmetry set of vacancy radical orbitals, contributes 0.03 eV stability. The structures with 1-4 H atoms in the vacancy are shown in 8. The first H atom forms a CH bond with a strength of 5.3 eV



7



8

with respect to its removal from the lattice cluster model. Based on the tertiary C-H bond strength in t-butane, this is a bit over 1 eV too strong. Subsequent H atoms are each calculated to bind about 1 eV more weakly than the previous one. This implies a bulk vacancy could trap up to 4 interstitial H atoms. The H atoms are

crowded quite close together, 1.18 Å when four are present. If there is a substantial number of such H-filled vacancies near the surface, they could contribute to the ~10 monolayers of H₂ desorption observed by Hamza et al.²³ in the temperature-programmed thermal desorption study of the polished (100)-(1x1) surface.

In the local-mode approximation the vibrational excitation of the CH bond for a single H in the vacancy is calculated to be about 3400 cm⁻¹. This is 300 cm⁻¹ higher than the CH stretch observed in natural diamond by IR.²² Since ASED-MO calculations overestimate secondary and tertiary C-H bond strengths, they could well overestimate the CH excitation for H in a vacancy site by ~300 cm⁻¹. Thus our calculations are probably consistent with a CH bond in a vacancy site as the source of the observed 3107 cm⁻¹ stretch. The calculated increases due to adding a second, third, and fourth H to the vacancy are ~400, 700 and 1400 cm⁻¹, respectively. Whether the first two of these are the cause of the observed broad IR absorption around 3700 cm⁻¹ in ref. 22 cannot be established without experimental studies of H concentration dependence and more detailed theoretical analysis.

REFERENCES

1. Yarbrough, W. A.; Messier, R. Science **1990**, *247*, 688.
2. Angus, J. C.; Hayman, C. C. Science **1988**, *241*, 913.
3. Angus, J. C.; Buck, F. A.; Sunkara, M.; Groth, T. F.; Hayman, C. C.; Gat, R., Mater. Res. Bull. October 1988, p. 38.
4. Spear, K. E. J. Am. Ceram. Soc. **1989**, *72*, 171.
5. Sellschop, J. P. F., Abstracts of the Diamond Conference, Bristol, U.K., 1987, p. 45.
6. Sellschop, J. P. F.; Madiba, C. C. P.; Annegan, H. J., Abstracts of the Diamond Conference, Cambridge, U.K., 1979, p. 43.
7. Vandentop, G. J.; Kawasaki, M.; Nix, R. M.; Brown, I. G.; Salmeron, M.; Somorjai, G. A. Phys. Rev. B **1990**, *41*, 3200 and references therein.
8. a. Frenklach, M.; Wang, H. Phys. Rev. B **1991**, *43*, 1520.
b. Harris S. J.; Weiner, A. M. J. Appl. Phys., to be published.
c. Toyoda, H.; Kojima, H.; Sugai, H. Appl. Phys. Lett. **1989**, *54*, 1507.
d. Belton, D. N.; Schmieg, S. J. J. Vac. Sci. Technol. A **1990**, *8*, 2353.
9. Mehandru, S. P.; Anderson, A. B. J. Mater. Res. **1990**, *5*, 2286; Carbon **1990**, *28*, 797.
10. Mehandru, S. P.; Anderson, A. B. Surf. Sci., in press.
11. Pankove, J. I.; Carlson, D. E.; Berkeyheiser, J. E.; Wance, R.O. Phys. Rev. Lett. **1983**, *51*, 2224.
12. Estreicher, S. Phys. Rev. B **1987**, *36*, 9122.
13. Van de Walle, C. G.; Bar-Yam, Y.; Pantelides, S. T. Phys. Rev. Lett. **1988**, *60*, 2761.
14. Chang, K. J.; Chadi, D. J. Phys. Rev. Lett. **1989**, *62*, 937.
15. Chang, K. J.; Chadi, D. J. Phys. Rev. B **1989**, *40*, 11644.
16. Chu, C. H.; Estreicher, S. Phys. Rev. B **1990**, *42*, 9486.
17. Claxton, T. A.; Evans, A.; Symons, M. C. R. J. Chem. Soc. Faraday Trans. 2, **1986**, *82*, 2031.

18. Estle, T.L.; Estreicher, S.; Marynick, D. S. Phys. Rev. Lett. **1987**, 58, 1547.
19. Briddon, P.; Jones, R.; Lister, G. M. S. J. Phys. C **1988**, 21, L1027.
20. Ruciman, W. A.; Carter, T. Solid St. Commun. **1971**, 9, 315.
21. Woods, G. S.; Collins, A. T. J. Phys. Chem. Solids **1983**, 44, 471.
22. Davis, G.; Collins, A. T.; Spear, P. Solid St. Commun. **1984**, 49, 433.
23. Hamza, A. V.; Kubiak, G. D.; Stulen, R. H. Surf. Sci. **1990**, 237, 35.
24. CRC Handbook of Chemistry and Physics, R. C. Weast, Editor, 67th Edition, Boca Raton, Florida, 1986.
25. Holtschuh, E.; Kündig, W.; Meier, P. F.; Patterson, B. D.; Sellschop, J. P. F.; Stemmet, M. C.; Appel, H. Phys. Rev. A **1982**, 25, 1272.

HOMOEPIITAXIAL HIGH TEMPERATURE DIAMOND GROWTH FROM OXYACETYLENE FLAMES

C. M. Marks, L. M. Hanssen, J.A. Freitas*, C. L. Vold†, K.A. Snail

Optical Sciences Division, Code 6522

†Materials Science and Technology, Code 6322

Naval Research Laboratory
Washington, DC 20375-5000

*Sachs Freeman Associates
1401 McCormick Drive
Landover, MD 20785-5396

Keywords: Diamond, Flame, Acetylene.

ABSTRACT

High quality single crystal diamond is grown from natural seeds in a fuel-rich oxyacetylene torch at substrate temperatures of 1150-1350°C. The flame-grown diamonds are optically clear and have a Raman and photoluminescence spectrum comparable to natural, type IIa diamond with very low defect density. Laue X-Ray diffraction patterns indicate the growth is epitaxial. Growth rates were 100-200 $\mu\text{m/hr}$, both vertically and laterally. {100} top seeds showed macroscopic terraces on the top surface after growth. Scanning electron microscope pictures show that initially round seed crystals grew into octagons.

Introduction

Among the new materials that have appeared recently, diamond has received much interest for its superlative properties. With its high thermal conductivity, optical transmission range, index of refraction, bandgap and breakdown voltage, diamond is important for heat sink, electronic and optical applications (1). A method of producing large single crystal boules of diamond would be particularly important for use as windows in optical materials and as wafers in semiconductor applications.

Experimental

Polycrystalline diamond films have been grown in oxyacetylene torches by several groups(2-6). As in our group's previous work(7,8), a torch system was used to grow diamond homoepitaxially on seeds as shown in the apparatus diagram in figure 1. The torch was a standard #0 brazing torch with an orifice diameter of 0.89 mm. Feed gases were purified 99.6% C_2H_2 dissolved in acetone and ultra-high purity, 99.99% O_2 , their flow rates controlled with mass flow controllers to a $\text{C}_2\text{H}_2/\text{O}_2$ ratio of 1.08. Acetone was removed from the C_2H_2 line by adsorption onto activated charcoal, while the O_2 was used without further purification. The seed was brazed with a Au-Ta braze to the face of a Mo screw, the height of which could be adjusted in a water-cooled Cu block to control the temperature. A two-color infrared pyrometer monitored the seed surface temperature, which was kept at 1250 ± 20 °C. The flame jet impinged upon the screw, with the seed crystal remaining within the flame feather. A Mo screw with a pinhole in its top face was connected to a differentially pumped mass spectrometer. The gases in the boundary layer will be sampled and the ratio of C, H and O atoms will be correlated to the growth conditions and rates.

Results and Discussion

Figures 2a and 2b show scanning electron micrographs of the diamond seed crystal before and after a one hour-long growth. The top {100} face grew into a regular octagon. The growth rate was $\sim 100 \mu\text{m/hr}$. The top face of the crystal is smooth except for $10 \mu\text{m}$ wide steps and optical microscopy shows the grown diamond to be remarkably clear. The Raman spectrum of the flame-grown diamond, shown in figure 3, has the same peak position and width as natural type IIa diamond within the limits of the instrument. A very small fluorescence background can be seen, but no non-diamond carbon can be detected in the spectrum.

The Laue X-Ray diffraction photograph shown in figure 4 shows that the diamond is a single crystal and that the growth is epitaxial. This is also seen from the trapezoidal side faces in figure 2b which correspond to the {111} faces on a cubo-octahedron.

Figure 5 shows a photoluminescence spectrum of the flame-grown diamond at 6 K. It was collected at a wavelength of 488 nm and a power of 20 mW. The major features seen besides the normal diamond Raman peak at 2.375 eV (b) are at 2.155 eV and 1.946 eV (d, e) and correspond to a N-vacancy complex and pair respectively, which are normally seen in flame-grown diamond (5). A small background luminescence seen across the entire spectrum is probably due to recombination of extended defects, which is seen in natural diamond as well.

Conclusions

High quality single crystal diamonds were grown in flames. The diamonds were exceptionally clear and have Raman and photoluminescence spectra showing high purity and low defect densities. Flame-grown diamonds grow at high rates and high temperatures suggesting a possible method for growing diamond boules.

References

1. E. Bruton, *Diamonds*, Chilton Book Company, Radnor, PA, 1978
2. Y. Hirose, S. Amanuma and K. Komaki, *J. Appl. Phys.* **68** 6401 (1990)
3. Y. Tzeng, C. Cutshaw, R. Phillips and S. Teradot, *Appl. Phys. Lett.* **56** 134 (1990)
4. K. V. Ravi and A. Joshi, *Appl. Phys. Lett.* **58** 246 (1991)
5. L. M. Hanssen, K. A. Snail, W. A. Carrington, J. E. Butler, S. Kellogg and D. B. Oakes, *Thin Solid Films* **196** 271 (1991)
6. K. A. Snail and C. J. Craigie, *Appl. Phys. Lett.* **58** 1875 (1991)
7. K. A. Snail and L. M. Hanssen, *J. Crystal Growth* In press, 1991
8. K. A. Snail, J. A. Freitas, C. L. Vold and L. M. Hanssen, *Proc. 2nd Intl. Symp. on Diamond Mats.* The Electrochemical Society, In press, 1991
9. J. A. Freitas, J. E. Butler and U. Strom, *J. Matl. Res.* **5** 2502 (1990)

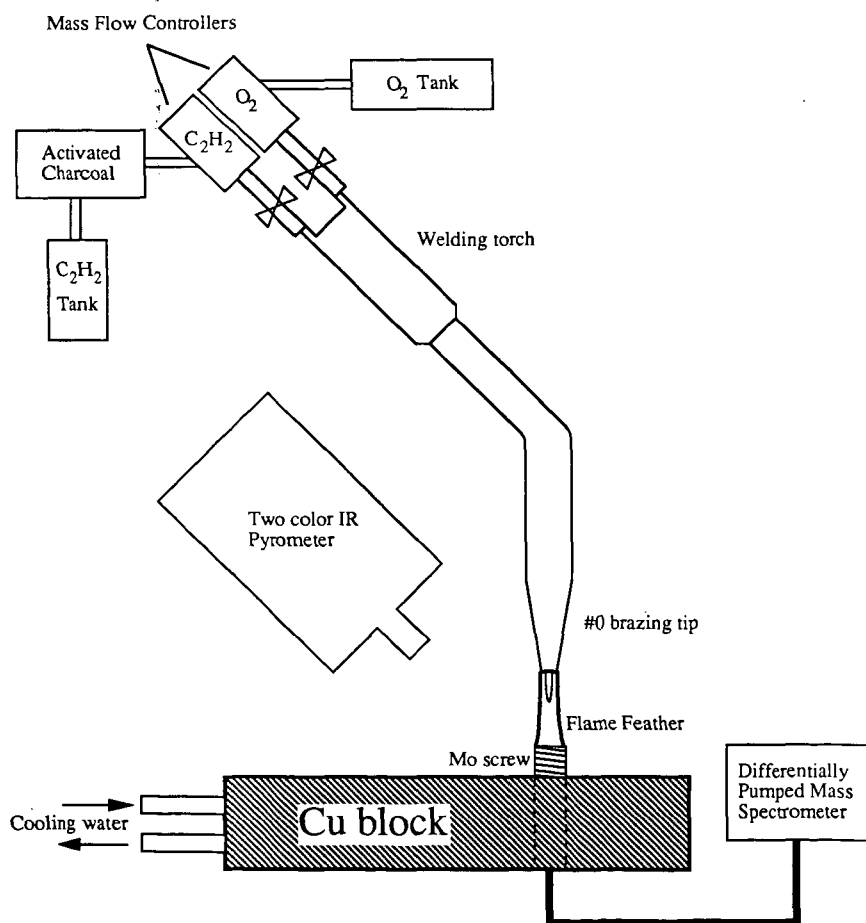


Figure 1. Oxyacetylene torch diamond growth apparatus.

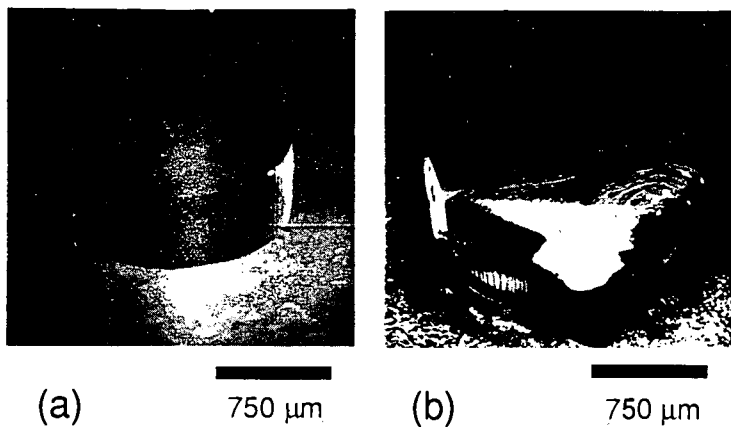


Figure 2. SEM photo of the seed diamond before (a) and after (b) growth in torch.

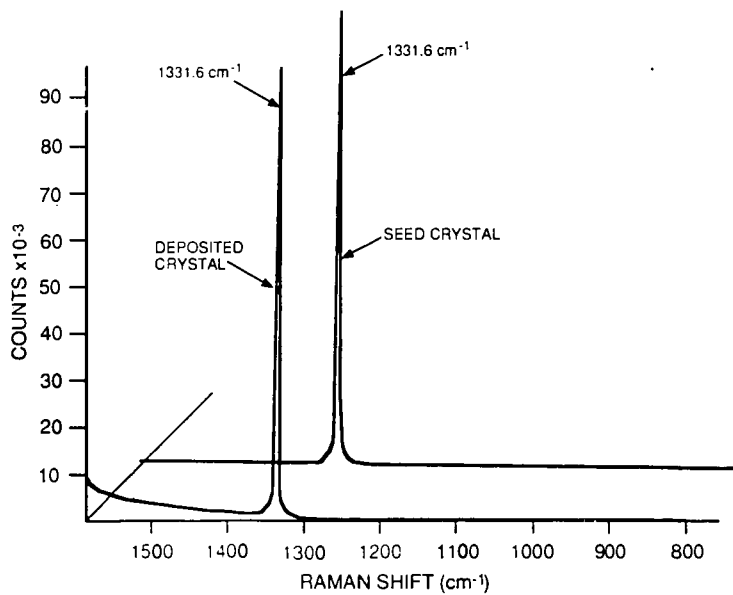


Figure 3. Raman Spectrum of the seed and flame-grown diamonds.



Figure 4. LaueX-Ray diffraction pattern of the flame-grown diamond.

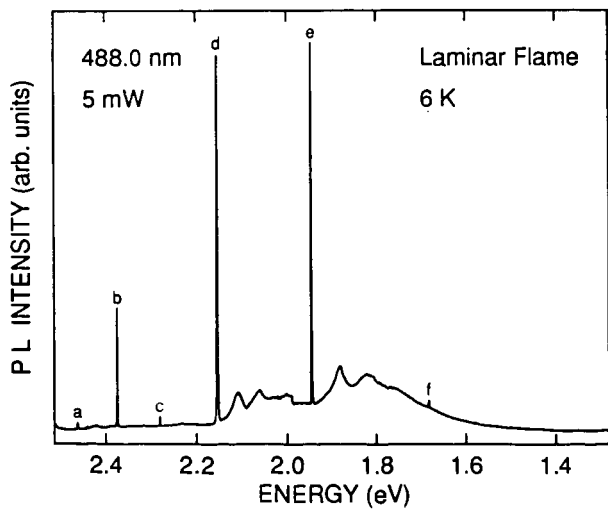


Figure 5. Photoluminescence Spectrum of the flame-grown diamond.

CARBON BLACK FROM COAL BY THE HYDROCARB PROCESS

Meyer Steinberg
Department of Applied Science
Brookhaven National Laboratory
Upton, NY 11973

INTRODUCTION

Carbon black is an ancient material and has been produced for over a century by several traditional processes.⁽¹⁾ The raw materials have been mainly residual oils from refineries and from natural gas. Furnace black is made by partial combustion of oil. Channel black is made by partial combustion of natural gas and the carbon is collected on iron channels. Thermal black is made from the thermal decomposition of natural gas (methane). About 2 million tons of carbon black is sold in the U.S. About 85% of the carbon black goes into the manufacture of tires for automotive purposes. It is a vulcanization and strengthening agent. The remainder goes into pigments, printing inks, and fillers. The largest part of carbon black, that which is used in tires is made from residual oil by the furnace black process. The smaller fraction is made by the thermal black process from natural gas.

There have been a number of attempts in the past to produce carbon black from coal. The recent ones deal with partial combustion in a sooty flame and collecting the fine carbon soot. However, the yields are poor and have never reached even advanced development stage. The value of searching for an alternative feedstock to oil and gas for carbon black production is important when considering the competitive use of the basic natural raw materials as energy sources, oil and gas being premium fuels. The resource of coal is an order of magnitude greater than oil and gas and as a source of carbon, coal as a feedstock is the cheapest.

Over the last six years we have conceived and are developing a process for producing carbon from coal primarily to satisfy the energy market. However, the process has implications for the carbon black commodity market.

THE HYDROCARB PROCESS

The HYDROCARB process was conceived and developed for the purpose of producing a clean carbon fuel and coproduct gaseous and liquid fuel coproducts^(2,3,4) from any carbonaceous feedstock and particularly from coal.

The process basically consists of two major steps. In the first step, coal is hydrogenated to produce methane. In this step, the carbonaceous raw material is gasified with a recycled hydrogen-rich gas stream to form a light hydrocarbon, methane-rich gas, while the non-volatile ash remains behind. With the optional addition of limestone to the feed material, sulfur in the feedstock is removed as non-volatile calcium sulfide which is later oxidized to calcium sulfate for disposal. The methane-rich gas which also contains carbon monoxide and smaller amounts of water and carbon dioxide is sent to a recuperative condenser. For the production of methanol, the carbon monoxide and hydrogen in the process gas is catalytically combined to produce methanol. The deoxygenated methane-rich gas stream is then sent to a methane decomposer where the methane is cracked to pure particulate carbon and hydrogen gas. The pure carbon is removed as a clean product and most of the hydrogen-rich gas is returned to the coal hydrogenator. The two basic steps are then coal hydrogasification in a hydrolysis reactor (HPR) and methane decomposition in a methane pyrolysis reactor (MPR). Table 1 outlines the process chemistry and Table 2, gives a schematic broadening of the process to

any carbonaceous raw material feedstock and indicates the co-product options, which include either a hydrogen-rich gas, a methane-rich gas, and methanol. Figure 1 shows one version of a process flow sheet. The methanol co-product option appears most attractive because of its usefulness as a high value chemical commodity and an environmentally preferable liquid transportation fuel.⁽⁵⁾

Among the important features of the process which assures high efficiency, is the fact that the hydrogasification or hydrolysis step is exothermic, giving off heat and the methane pyrolysis step is endothermic absorbing heat. By transferring heat from step 1 to step 2, the process efficiency is greatly enhanced. This is accomplished by circulating solid alumina pellets as a heat transfer and transport media through the hydrolyzer and to the methane pyrolyzer as shown in Figure 1. The reactors can be either moving bed or fluidized bed types.

The process is based on sound thermodynamic, and process chemistry principles. Experimental data for the hydrolysis and methane decomposition through pilot plant scale are available. Engineering demonstration is yet to be performed.

PROPERTIES OF CARBON BLACK

Because the carbon black is ash- sulfur- and nitrogen-free it is a potentially ideal coal derived fuel which can be utilized in heat engines, i.e., diesels and turbines, as well as in power plant and industrial boilers with little modification. Its major drawback is that it has no volatility resulting in a higher ignition temperature. Radiant combustors or additives of oil or methanol can solve that problem for use in conventional systems. Because the density of carbon black is high (1.8 to 2.0 gm/cc) it can be added to hydrocarbon fuels to volumetrically energy densify those fuels. Fig. 2 shows that adding carbon to methanol will increase the heating value of hydrocarbon fuels. A 55% carbon black-45% methanol slurry has a HHV equivalent to that of gasoline.

We have produced carbon black from methane in our laboratory in a countercurrent moving alumina bed reactor at 1000°C and 800 psi which is about the design conditions for the HYDROCARB process. Photomicrographics of the carbon black are shown in Fig. 3. The figure compares the collected carbon with a commercial grade carbon designated as N-990 produced by the thermal black process from natural gas. The HYDROCARB carbon black shows similar spherical particles ranging in size from 0.3 to 1.0 micron agglomerated up to about 4.0 microns. The commercial grade ranges from 0.2 to 0.5 microns with aggregates of over 100 microns. Geometrically, the laboratory carbon black appears in the range of thermal black. We have yet to examine the surface properties or whether other particle sizes can be produced at different reactor conditions. Further characterization must be performed to determine whether commodity grade carbon black can be produced and especially its suitability for the tire market.

ECONOMIC ESTIMATES

Preliminary economic estimates of the production of carbon black in large scale coal plants using the HYDROCARB process have been made. For a 25,000 T/D high volatile bituminous coal feedstock it is estimated that the production capacity would be about 16,000 T/D maximum and taking credit for by-product hydrogen would be priced at between 3.5¢ and 5.0¢ per pound competing with \$2.50 to \$3.50/MMBTU or \$15 to \$21/Bbl of oil.^(2,3) This price includes 15% return on plant equity. It is instructive to compare the economics of the manufacture of commercial carbon black from various fossil fuel resources with that projected for the HYDROCARB prices. Based on 1986 prices, Table 2 indicates that carbon black from natural gas (thermal black) and crude oil (furnace black) ranged in price from 16¢ to 35¢ per pound depending on the more than a dozen different grades produced by the industry. Recent (1990) prices run up to as high as 50¢/lb.

From the raw feedstock point of view, the cost of contained carbon from natural gas and oil ranges from about 6 to 10¢ per pound and remembering that residual oil from crude may be somewhat lower. However from coal, the contained carbon ranges from 1.1 to 1.8¢ per pound which is from 5 to 10 times lower than for oil or gas. If the HYDROCARB carbon can be found to be suitable for the tire as well as for other commodity markets, then the estimated selling price would be 3 to 10 times less than the commodity selling price of carbon black. If off-grade carbon black which is only available at times in limited quantity for as low as 10¢ per pound HYDROCARB carbon would be 2 to 3 times lower. However, one 25,000 T/D HYDROCARB plant would produce almost 3 times the entire annual capacity of commodity carbon black in the U.S. Therefore, HYDROCARB carbon black designed for supplying the fuel market could easily supply all the commodity market as a by-product.

CONCLUSION

HYDROCARB process carbon black designed primarily for the energy market can supply the commercial commodity market at much reduced prices. Much additional work is necessary to determine the characteristics of HYDROCARB carbon black for suitability for tire manufacture as well as for any other possible large scale commodity market. Process demonstration of an integrated system is necessary to prove the ability to scaleup the process to commercial size.

REFERENCES

- 1) J.B. Donnet and A. Voct, Carbon Black, Marcel Dekker, Inc., New York (1976).
- 2) E.W. Grohse and M. Steinberg, "Economical Clean Carbon and Gaseous Fuels from Coal and other Carbonaceous Raw Material," BNL 40485, Brookhaven National Laboratory, Upton, NY 11973 (November 1987).
- 3) M. Steinberg and E.W. Grohse, "Economical Clean Carbon Fuel and Co-product Gaseous and Liquid Fuel from Coal," BNL 42489, Brookhaven National Laboratory, Upton, NY 11973 (September 1989).
- 4) M. Steinberg, "Coal to Methanol to Gasoline by the HYDROCARB Process," BNL 43555, Brookhaven National Laboratory, Upton, NY 11973 (August 1989).
- 5) R.H. Borgwardt, M. Steinberg, E.W. Grohse, and Y. Tung, "Biomass and Fossil Fuel to Methanol and Carbon via the HYDROCARB Process," Presented at the Institute of Gas Technology Conference in Energy from Biomass XV, Washington, D.C., March 27, 1991 (to be published in Proceedings of Conference).
- 6) G. Wei and M. Steinberg, "Carbon Black Slurries, Preparation and Characteristics," BNL 43732, Brookhaven National Laboratory, Upton, N.Y. 11973 (November 1989).

TABLE 1
HYDROCARB PROCESS FOR
PRODUCTION OF ASH-FREE AND SULFUR-FREE
CLEAN CARBON FUEL (CARBOLINE) AND FUEL GAS FROM COAL

TWO BASIC STEPS:

I. HYDROGASIFICATION OF COAL WITH HYDROGEN TO METHANE.

BITUMINOUS COAL + HYDROGEN \longrightarrow METHANE + WATER + HYDROGEN + ASH



REACTION IS -18 KCAL/MOL EXOTHERMIC.

II. THERMAL DECOMPOSITION OF METHANE.

METHANE \longrightarrow CARBON BLACK + HYDROGEN.



REACTION IS +18 KCAL/MOL ENDOTHERMIC.

HYDROGEN IS RECYCLED. EXCESS HYDROGEN IS A CO-PRODUCT. CARBON BLACK IS A FUEL AND CAN BE SLURRIED WITH WATER TO PRODUCE CARBOLINE CWM PRODUCT.

OVERALL COAL CRACKING REACTION



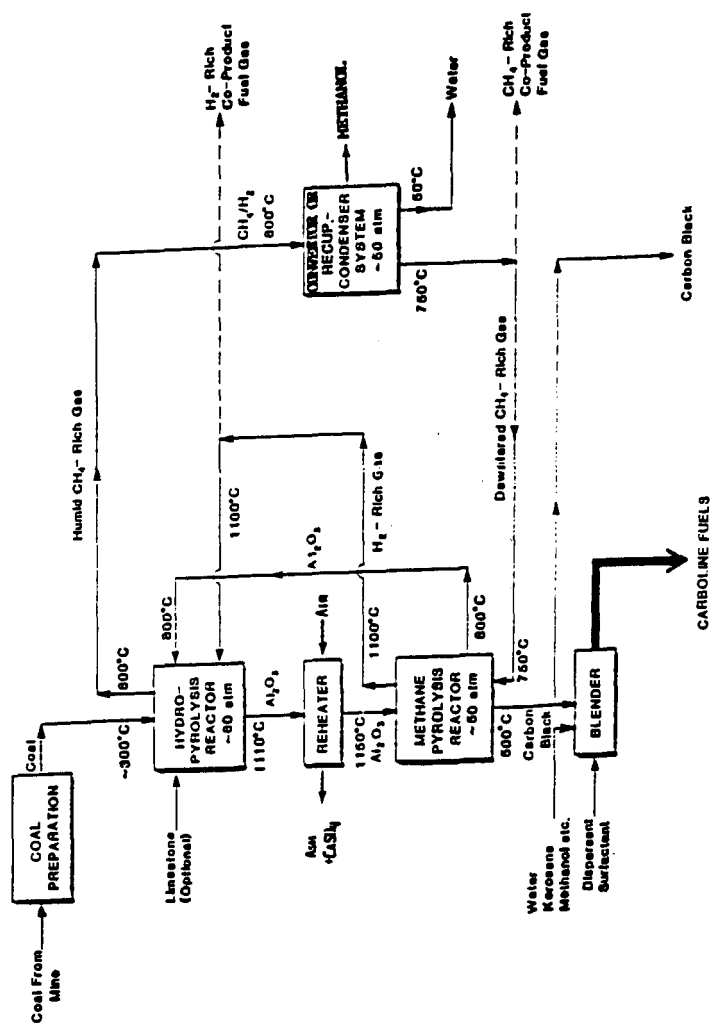
B.7

Table 2

Comparative Economics of Carbon Black Production in the U.S.
From Various Fossil Energy Resources (1986)

Resource	Natural Gas	Crude Oil Residuals	Coal (Proposed)
<u>Raw Material Cost</u>			
\$/MMBtu	2.00 to 3.00	2.50 to 3.50	1.00 to 0.70'
\$/MSCF	2.00 to 3.00	-	-
\$/Bbl	-	15.00 to 21.00	-
\$/ton	-	-	25.00 to 10.00
¢/lb of contained C	6.3 to 9.5	6.2 to 8.7	1.8 to 1.1
<u>Present Prices of Carbon Black</u>			
Commodity Grade:			
¢/lb	16 to 35	16 to 35	Suitability for tire
\$/ton	320 to 700	320 to 700	manufacture still
\$/MMBtu	11.35 to 24.80	11.35 to 24.80	to be established
Offgrade (for fuel):			
¢/lb	10 (est'd)	10 (est'd)	3.5 - 5.0
\$/ton	200	200	70 to 100
\$/MMBtu	7.10	7.10	2.50 to 3.50
<u>Total Present U.S. Capacity for The Production of Carbon Black</u>			
Tons/year	0.2×10^6	2.0×10^6	5.3×10^6 *
Tons/day	600	6,000	16,000
<u>Estimated Present Availability of Fuel Grade Carbon Black</u>			
Tons/day	200 (est'd)	2,000 (est'd)	16,000*
No. of plants	1	10	1

*Proposed HYDROCARB plant. This is the production capacity for one 25,000 T/D coal plant producing carbon black and fuel gas (corresponding to a total fuel equivalent 83,500 BPD FOE oil refinery).



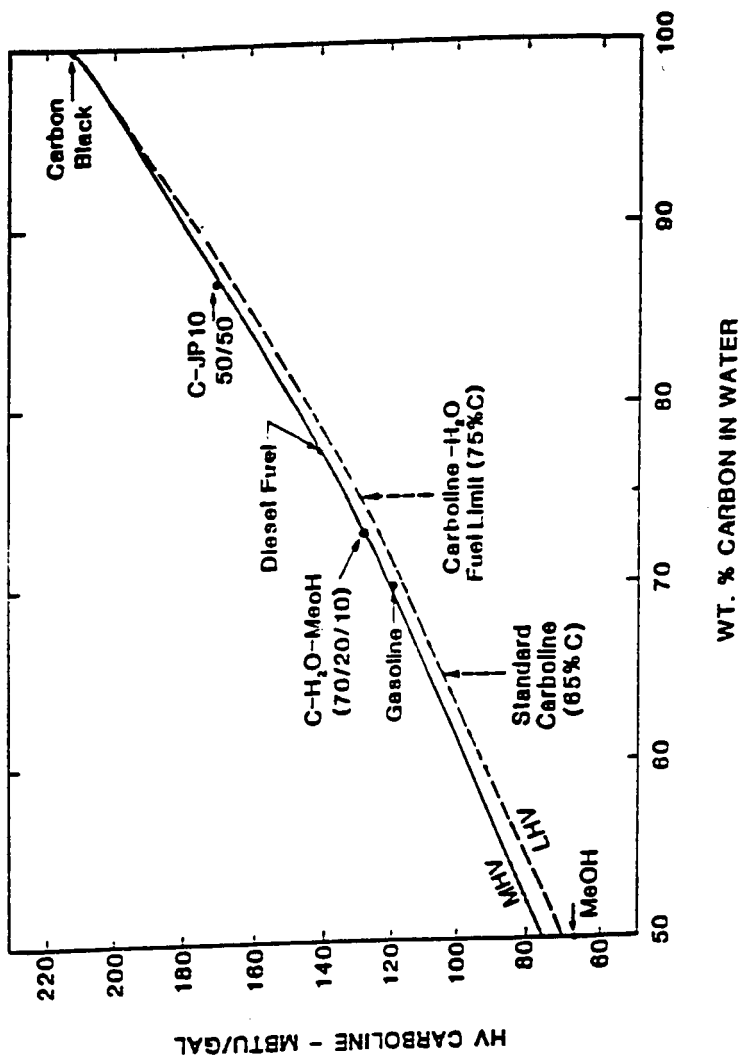
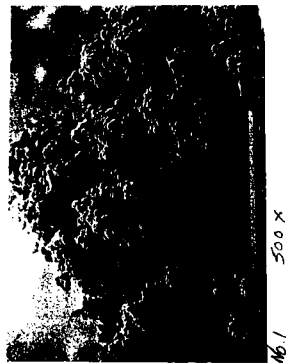
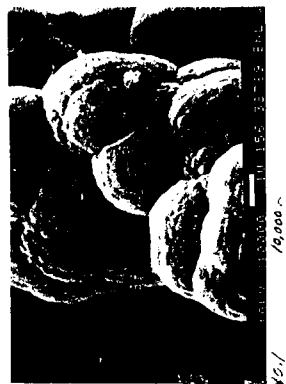


Figure 2. Heating Values of Carboline and Competitive Fuels



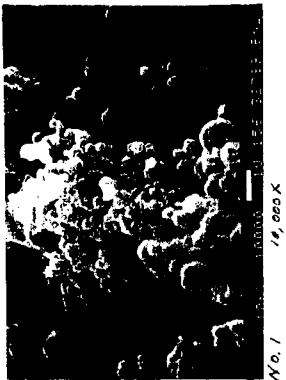
No. 1

500 X



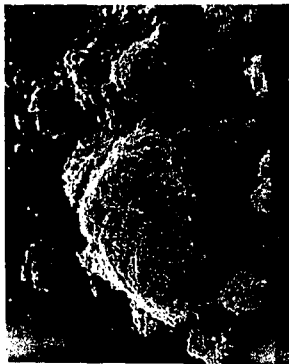
No. 1

10,000 X



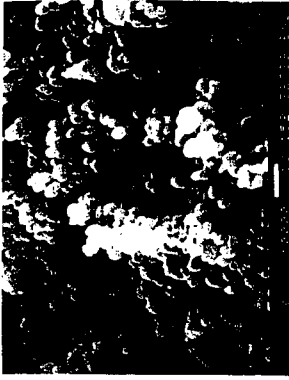
No. 1

14,000 X



No. 2

500 X



No. 2

10,000 X



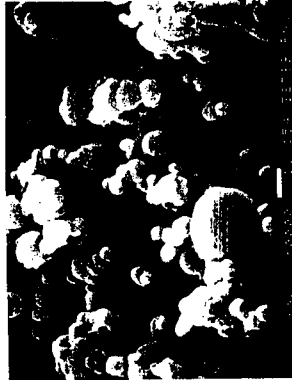
No. 3

500 X



No. 3

10,000 X



No. 3

10,000 X

- NO. 1 - C-BLACK FROM BNL MOVING BED REACTOR RUN NO. 1099 -
PLUG IN REACTOR FORMED AT 800 PSI AND 1000°C -
0.5 TO 1 μ AGGLOMERATED TO $\sim 4\mu$
- NO. 2 - C-BLACK FROM HUBER CO. - COMMERCIAL GRADE H-990
PARTICLE SIZE 0.2 TO 0.5 μ
- NO. 3 - C-BLACK FROM BNL MOVING BED REACTOR RUN NO. 1099
FILTER LOCATION FORMED AT 800 PSI AND 1000°C -
0.3 TO 2.0 μ

Figure 3. Photomicrographs of
Carbon Black

THE PRODUCTION OF ACTIVATED CARBONS FROM COALS BY CHEMICAL ACTIVATION

F J Derbyshire, M Jagtoyen, B McEnaney,
A R Sethuraman, J M Stencel, D Taulbee
and M W Thwaites

University of Kentucky Center for Applied Energy Research,
3572 Iron Works Pike, Lexington, Kentucky 40511-8433, USA.

Keywords: coal; activated carbons; chemical activation;
phosphoric acid.

ABSTRACT

Activated carbons prepared from coals by chemical means using phosphoric acid as the activant have a dominantly microporous adsorptive capacity which develops up to 450 °C. Chemical activation promotes carbonization at lower temperatures than is obtained thermally and is effective in removing sulfur, mainly as hydrogen sulphide. Reducing the ash content of a bituminous coal by cleaning prior to activation has beneficial effects upon surface area development.

INTRODUCTION

Coals are widely used as feed-stocks for activated carbons produced by "thermal" methods, i.e., by carbonization followed by reaction with oxidizing gases (e.g., steam or carbon dioxide) at elevated temperatures. By contrast, the preparation of activated carbons from coals by "chemical" activation (i.e., by reaction with an ionic reagent at lower temperatures than are used for thermal activation) has been little studied. Chemically-activated carbons are commercially produced from cellulosic precursors using zinc chloride or phosphoric acid as activants (1), but here too there is little fundamental understanding of the chemistry of the conversion processes.

The objectives of the present work are to investigate the potential of coals of different rank as precursors for the production of active carbons using phosphoric acid as the activant. Specific aims are to relate the development of porosity in the carbons to the structure of the precursor and to the chemical and morphological changes. In this paper we report a study using a subbituminous coal and a bituminous coal as precursors, including some results of pre-cleaning the bituminous coal using flotation.

EXPERIMENTAL

Chemical Activation.

The sub-bituminous coal is mined from the Wyodak seam in Wyoming (designated: Wyodak coal) and the bituminous coal was selected from the Illinois Coal Basin Sample Program (designated IBC 101 coal); chemical analyses of the coals are shown in Table 1.

The ground coals (-850 μm) were reacted with 50% phosphoric acid in two temperature stages. For the Wyodak coal, the first stage involved refluxing a coal-acid mixture (4:1 ratio of acid solution to coal) for 60 min, following which the slurry was concentrated by evaporation (maximum temperature, about 130°C). In the second stage, the slurry was heat treated in a stainless steel reactor, under flowing nitrogen at atmospheric pressure and held for 60 min at a final heat treatment temperature (HTT) between 350 and 650°C.

For the IBC 101 coal, the first stage procedure was modified: a coal-acid slurry (30 ml acid:20 g of coal) was heated to 170 °C in the same reactor, and held at this temperature for about 30 minutes before heating to the final HTT. The content of H_2S released as gas was monitored with a HACH Carle gas chromatograph using standard procedures for calibration. The solid products were leached with distilled water to pH = 6 and vacuum dried at 110 °C for further analysis. For comparison, parallel series of carbonized coals were prepared by heat treatment for 1 h in flowing nitrogen (80 ml/min) at the same HTT values.

Coal cleaning.

Clean coal samples have been produced using a laboratory scale flotation unit. In a typical arrangement, fuel oil or pentane is vigorously mixed with a coal/water slurry to render the coal particles hydrophobic and to selectively agglomerate them. The agglomerated slurry is then screened; the free ash particles flow through the screen and agglomerated coal is retained.

Characterization.

Elemental analyses of the carbons were carried out using standard methods. The carbons were also examined using Fourier transform infra red spectroscopy (FTIR) and X-ray photoelectron spectroscopy (XPS). FTIR spectra were acquired using a NICOLET 20 SXC spectrometer at 4 cm^{-1} resolution. Pressed KBr pellets at a sample/KBr weight ratio of 1:200 were scanned and then normalized to 0.5 mg. Spectral subtractions were conducted on an equivalent weight basis. XPS analysis of the coal samples was carried out in a Leybold-Heraeus LH-11 spectrometer equipped with a hemispherical analyzer using Mg $\text{K}\alpha$ radiation (1253.6 eV) at a pass energy of 100 eV. The powdered coal samples were pressed into a thin wafer and were placed on a stainless steel sample holder using a conductive adhesive. The spectra obtained in all regions have been referenced to C1s at 284.3 eV (BE). The identification of the various chemical species has been carried out using NIST XPS Database Version 1.0 and standard compounds. Pore structure characterization was carried out using nitrogen adsorption at 77K using an Autoscan 6 automated adsorption apparatus.

RESULTS

Chemical and Structural Changes

Comparison of the thermally-treated and chemically-activated carbons, Table 1, shows that acid-treatment of both coals causes a more rapid increase in carbon content and reduction in H/C atomic ratio with increasing HTT, which are more pronounced at lower HTT. The ash contents of carbons from both precursors increase with HTT, but those for the acid-treated products are much higher, particularly at $\text{HTT} > 450^\circ\text{C}$, and correlate with increases in P content. For both coals, acid-treatment up to $\text{HTT} = 650^\circ\text{C}$ releases about 75% of the sulphur in the original coal, Table 1, mainly as H_2S , e.g., Figure 1. The release of sulfur as H_2S from the thermally-carbonized series shows a similar trend to that observed by Khan (2).

The FTIR spectra for the IBC 101 coal and the chemically-activated carbons are shown in Figure 2. There is a strong band at 2914 cm^{-1} in the parent coal, due to aliphatic C-H stretch, which decreases at $\text{HTT} = 350^\circ\text{C}$, while the band at 3040 cm^{-1} due to aromatic C-H stretch intensifies, suggesting that aromatization may be occurring. The band appearing at 1690 cm^{-1} after $\text{HTT} = 350^\circ\text{C}$ is due to carbonyl (C=O) groups. It weakens in intensity at $\text{HTT} = 550^\circ\text{C}$ and disappears at $\text{HTT} = 650^\circ\text{C}$. Carbonyl groups have also been found both in Sutcliffe Speakman 110 activated carbon (3) and in carbons produced by activation of coconut shell with phosphoric acid (4). The difference spectrum obtained by subtracting the spectrum of the thermally-treated sample from that of the acid-treated sample at $\text{HTT} = 450^\circ\text{C}$ (Figure 3) suggests that the coal is oxidized by chemical activation. For the chemically-activated carbons a particularly strong band appears at 1180 cm^{-1} at $\text{HTT} = 450^\circ\text{C}$, 550°C and 650°C . The origin of this band is uncertain. It may be due either to additional C-O stretch, or to P=O groups attached to an aromatic structure. The source of the 1180 cm^{-1} band is being investigated.

Compilations of the C1s and P2p XPS spectra obtained from the chemically-activated carbons from IBC 101 coal after various HTT are in Figure 4; these spectra have been de-convoluted into component peaks. The C1s spectra, Fig. 4(a) to 4(e), have been fitted to four component peaks. The most intense peak, ca. 284.3 eV, is attributed to graphitic-type carbon species; the second peak at ca. 285.8 eV may be due to organophosphate species; the third peak at ca. 287.9 eV coincides with that of carbonyl groups, in agreement with the FTIR results; the fourth peak at ca. 289.1 eV is due to carbonate groups. The prominent peaks at ca. 133.5 eV and ca. 135.3 eV in P2p spectra, Fig. 4(a)-(b)', are attributed to inorganic hydrophosphate groups and to P_2O_5 respectively. When HTT increases from 350 to 450°C , the hydrophosphate intensity decreases and there is a corresponding increase in the P_2O_5 intensity, suggesting a dehydration process. At $\text{HTT} = 550$ and 650°C , the hydrophosphate and P_2O_5 peaks are

still present, but two additional peaks appear whose origins are uncertain. The peak at ca. 131.6 eV could either be due to a phosphide of a transition metal or to a phosphorous compound in association with organic sulfur species. The peak at ca. 136.1 eV may be due to a P-containing species in a high oxidation state; work on the identification of these peaks is continuing.

Pore Structure Characterization

BET surface areas, S_{BET} , were obtained from the nitrogen adsorption isotherms for the activated carbons. The isotherms were also analyzed by the α_s method (5) to yield non-microporous surface areas, S'_{BET} , and micropore volumes, V_o , Table 2. Both carbon series are dominantly microporous, although the development of microporosity is more extensive for the carbons produced from the Wyodak coal. The extents of mesoporosity in the two series (indicated by S'_{BET} values) are comparable for $\text{HTT} > 450^\circ\text{C}$. For both carbon series S_{BET} and S'_{BET} pass through maxima below $\text{HTT} = 650^\circ\text{C}$, as observed by others (4). However, the effect of HTT on surface area is obscured by the substantial ash contents of the activates, Table 1. Assuming that the ash makes a negligible contribution to nitrogen adsorption, the surface areas can be recalculated on a dry, ash-free (daf) basis, Table 2. The corrected data show that, for the Wyodak coal series, the maximum in S_{BET} is shifted to a higher HTT , while, for the IBC coal series, the maximum disappears (or is possibly shifted to $\text{HTT} > 650^\circ\text{C}$). S_{BET} values for the thermally-treated coals (not shown in Table 2) increase with HTT up to 50 m^2/g for the Wyodak coal series and up to 24 m^2/g for the IBC 101 coal series. The results indicate that the thermally-treated carbons contain narrow micropores and negligible mesoporosity.

The data in Tables 1 and 2 show that coal cleaning by flotation substantially reduces the ash content of the parent IBC 101 coal by 61%; the ash content of the chemically-treated carbon produced from the cleaned coal at $\text{HTT} = 550^\circ\text{C}$ is reduced by 55% when compared with that for the activate formed from the parent coal at the same HTT . Table 2 shows that coal cleaning produces a significant increases in both S_{BET} and S'_{BET} .

DISCUSSION

Chemical analyses and FTIR results show that phosphoric acid treatment of the coals promotes aromatization and carbonization at low HTT . Evidence for accelerated carbonization is also provided by reflectance measurements on the subbituminous coal (6). The processes occurring during the reaction of phosphoric acid at low temperatures are probably analogous to acid-catalyzed cracking reactions in coal liquefaction using Lewis acids. Acid catalysts can promote rupture of methylenic, etheric and thioetheric linkages between cyclic structures in coal by ionic mechanisms which involve protonation followed by bond scission (7). Proton donation from phosphoric acid to aromatic

entities, -Ar-, in the coal structure is consistent with the XPS evidence for inorganic hydrophosphates; the reactions can be represented as:



In the present case, it is likely that bond scission will be followed by rapid condensation of aromatic fragments to form a strongly cross-linked solid product at much lower temperatures than are required for thermal decomposition of the coal. The indications from FTIR and XPS for the presence of organophosphorus entities suggest that direct reactions between phosphoric acid and the coal structure also occur, particularly at high temperatures. The formation of an extensive cross-linked network at low temperatures in the chemical activation process may be linked to the early development of significant open microporosity. By contrast, the condensation processes which accompany thermal carbonization occur at much higher temperatures and lead to significant shrinkage and formation of a closed micropore network which can only be developed by subsequent thermal activation.

CONCLUSIONS

There are clear differences in porosity development between the thermally-carbonized and chemically-activated coals, which reflect differences in structural development. Acid-treatment causes the rupture of linkages in the coal structure, leading to adduction and the early development of a strongly cross-linked solid product. This process is accompanied by the development of high surface areas at moderate HTT. Work on elucidating the mechanisms of the chemical activation process is continuing.

ACKNOWLEDGEMENTS

The authors thank several colleagues at the CAER for help with this research, the Illinois Center for Research on Sulfur in Coal and the CAER for financial support, and Kerr-McGee Coal Corporation for the gift of the Wyodak coal sample.

REFERENCES

1. Smisek, M. and Cerny, S. *Active Carbon Manufacture, Properties and Applications*, Elsevier, Amsterdam, 1970.
2. Khan, M. R., *Fuel*, 1989, **68**, 1439.
3. Meldrum, B.J. and Rochester, C.H., *Fuel*, 1991, **70**, 57.
4. Laine, J., Calafat, A. and Labady, M., *Carbon*, 1989, **27**, 191.
5. Rodriguez-Reinoso, F., Martin-Martinez, J.-M., Prado-Burquette, C. and McEnaney, B., *J. Phys. Chem.*, 1987, **91**, 515.
6. Derbyshire, F. J., Jagtoyen, M., McEnaney, B., Rimmer, S. M., Stencil, J. M. and Thwaites, M. W. *Proc. 20th Biennial Carbon Conference*, 23-28 June, 1991, Sta. Barbara, CA., in press.
7. Derbyshire, F.J., *Catalysis in Coal Liquefaction.*, IEA Coal Research, London, 1988, pp. 29-36.

TABLE 1. CHEMICAL ANALYSIS OF COALS AND CARBONS (wt%)

Material	HTT	C	H	N	S	P	Ash
	(°C)	(daf)					(mf)
<u>Wyodak coal</u>							
Parent coal		74.3	5.0	1.0	1.2	0.03	8.2
Thermally treated	350	77.7	3.8	1.2	1.1	0.01	8.0
carbons	450	82.6	2.9	1.3	0.9	0.01	9.3
	550	91.6	2.0	1.5	1.2	0.01	11.9
	650	94.1	1.5	1.4	1.2	0.3	11.9
Chemically treated	350	87.7	2.3	1.2	0.8	1.4	9.7
carbons	450	91.1	1.7	0.9	0.5	1.4	7.3
	550	94.4	1.3	0.9	0.3	4.7	17.6
	650	94.6	0.4	1.1	0.3	4.4	15.9
<u>IBC 101 coal</u>							
Parent coal		79.8	5.2	1.4	5.2	0.0	10.5
Thermally treated	350	78.8	4.9	1.4	4.6	0.01	10.2
carbons	450	86.5	3.1	1.7	3.7	0.01	13.6
	550	91.1	2.2	1.9	4.7	0.01	15.1
Chemically treated	350	87.1	3.8	1.5	2.9	2.5	15.8
carbons	450	86.9	2.5	1.2	1.6	5.1	26.6
	550	93.4	1.4	1.4	1.2	3.9	20.8
	650	102.7	0.9	1.4	1.2	7.2	31.1
Cleaned parent		78.0	5.2	1.4	4.4	0.03	4.1
Clean carbon	550	88.9	1.9	1.1	0.9	1.5	9.2

TABLE 2. ADSORPTION PARAMETERS FOR CHEMICALLY-ACTIVATED CARBONS

Precursor	HTT (°C)	S _{BET} (m ² g ⁻¹)	S' _{BET} (m ² g ⁻¹)	V ₀ (cm ³ g ⁻¹)	S _{BET} (daf)	S' _{BET} (daf)
<u>Wyodak coal</u>						
	350	416	31	0.17	461	34
	450	791	54	0.32	853	58
	550	731	47	0.30	887	57
	650	718	34	0.30	854	40
<u>IBC 101 Coal</u>						
	350	2	1	>0.01	2	1
	450	401	25	0.14	546	34
	550	575	56	0.20	726	71
	650	539	46	0.19	782	67
Cleaned coal	550	638	96	0.21	703	106

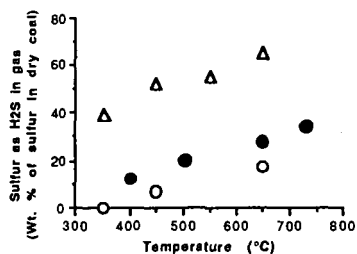


Figure 1. Liberation of sulfur as H₂S

This work: Δ (acid treated coal), \circ (no acid treatment)

\bullet Khan (2), (no acid treatment)

18C-101 PHOSPHORIC ACID TREATED SAMPLES

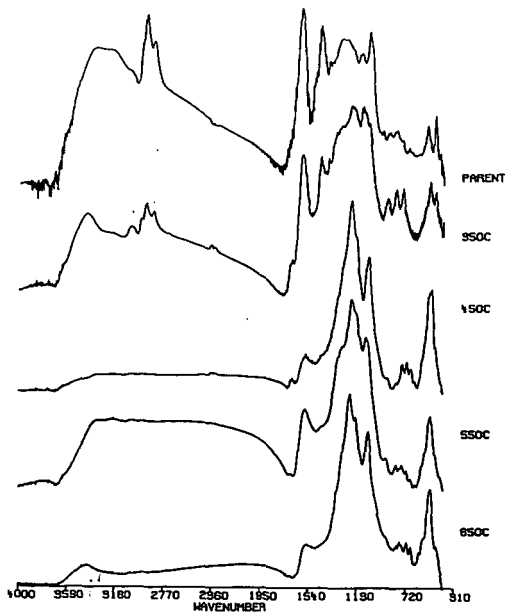


Figure 2. Infrared spectra of activated carbon prepared by chemical activation with phosphoric acid at 350, 450, 550 and 650°C along with parent coal.

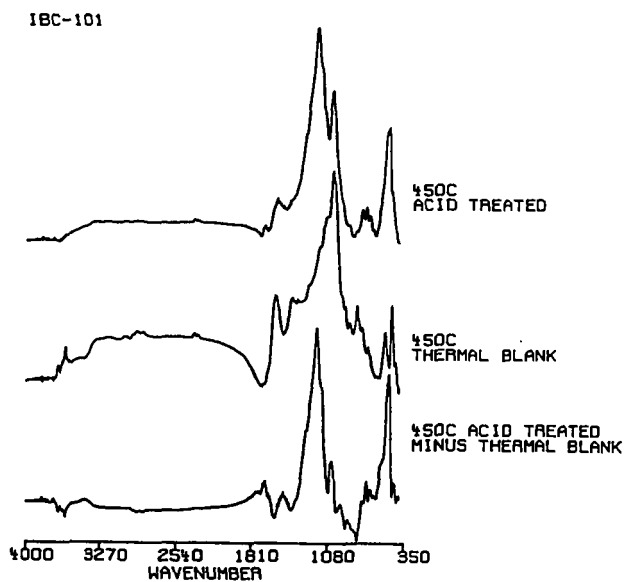


Figure 3. Infrared spectra of chemically activated carbon and thermally carbonized carbon at 450°C and a difference spectrum of chemically activated carbon minus thermal blank.

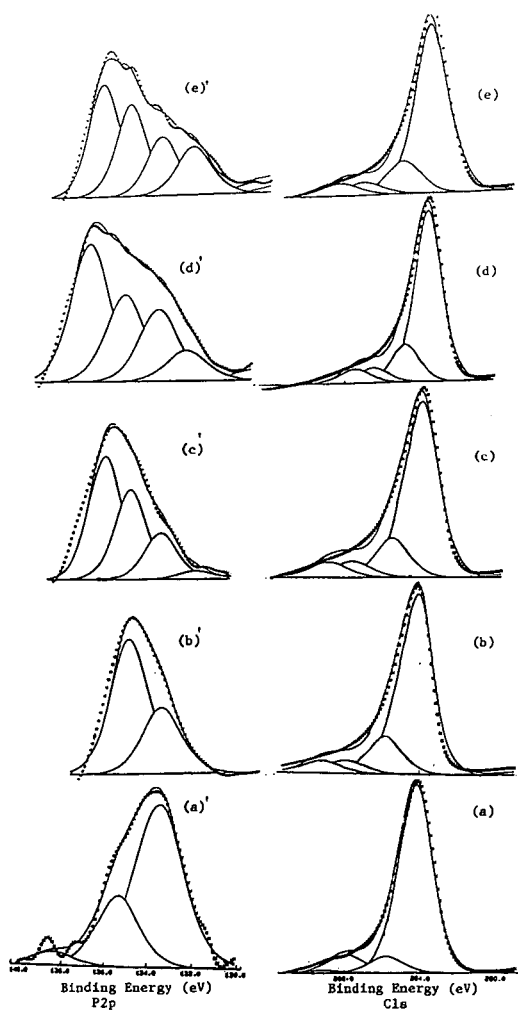


Figure 4. XPS spectra for carbons produced from IBC 101 coal. HTT(°C): 350 (a) (a'); 450 (b) (b'); 550 (c) (c'); 550 (cleaned coal) (d) (d'); 650 (e) (e').

IN SITU EVALUATION OF THE CARBONIZATION BEHAVIOR OF GRAPHITIZABLE CARBON PRECURSORS

Joaquin Rodriguez, John W. Tierney and Irving Wender
Chemical & Petroleum Engineering Department
University of Pittsburgh, Pittsburgh PA 15261

Keywords: Mesophase, Polarized light microscopy, Graphitizable carbons

ABSTRACT

Highly aromatic petroleum residues were carbonized in a high temperature high pressure cell mounted under a polarized light microscope in order to evaluate the appearance, development and type of the anisotropic mesophase. Kinetic parameters (formation and coalescence periods) were related to the nature of constitutive fractions (aromatics, resins, asphaltenes). The final type of anisotropic mesophase is determined by the nature of the starting material. However it is also sensitive to mixing and pretreatment processes such as desulfurization and thermal cracking. This technique can be used to select suitable carbon fiber feedstocks and to evaluate the effects of modifying agents, mixing and treatment processes. It has many advantages over traditional methods which measure the optical texture of polished surfaces.

INTRODUCTION

The complex nature of petroleum residues used for the production of graphitizable carbons (e.g. needle coke, mesophase pitch carbon fibers) makes it difficult to find a single chemical analysis or physical property to rank potential feedstocks in terms of final product quality. It is known, however, that high aromaticity and low Conradson Carbon values are required⁽¹⁾, and development of the liquid crystalline state intermediate (mesophase) is necessary^(2,3). Since the discovery of the nature of the mesophase intermediate by Brooks and Taylor⁽⁴⁾ attempts have been made to characterize and correlate its description with the potential to produce graphitic carbons. Patrick⁽⁵⁾ and Marsh⁽⁶⁾ have developed two classifications in terms of the shape and size of optical texture of anisotropic cokes observed by polarized light microscopy using polished surfaces. These classifications are complemented by assignment of an arbitrary index (Optical Texture Index), related to the area of microstructural units⁽⁷⁾. The OTI can be implemented in point counting techniques to give an average number. Similar attempts have been made for Scanning Electron Microscope⁽⁸⁾ and brightness histograms⁽⁹⁾. However, these methods require preparation of solid samples (in autoclaves) and extremely careful polishing before observations can be made. Alternatively, Perrotta⁽¹⁰⁾ introduced a dynamic analysis based on in situ monitoring of mesophase development taking place in a micro-cell mounted on a hot stage polarized light microscope. It follows the actual transformation of pitch into anisotropic structures. The test can be performed in less than one hour, in comparison with several days required for previous methods.

This paper introduces a classification of mesophase structures for this dynamic test which is also applied to the evaluation of petroleum residues, constitutive HPLC (High Performance Liquid Chromatography) fractions and treated (distillation, desulfurization, thermal cracking, delayed coking) samples.

EXPERIMENTAL

A high temperature (to 500 ° C) high pressure (to 2000 psig) micro-cell (Figure 1) was designed⁽¹⁰⁻¹¹⁾ to fit a hot stage placed under a polarized light microscope. The cell arrangement includes a 2.9 mm o.d. by 1.25 mm cylindrical quartz pan (2 mg sample capacity) mounted on the bottom of the cell which is equipped for the flow of gases. A 5 mm o.d. by 2 mm soft copper O-ring is mounted on top of the pan and coupled with a 5 mm o.d. by 1.65 mm spinel crystal, sealed together tightly on a stainless steel cover. The cell is mounted on a Leitz 1618 hot stage incorporating a tungsten filament furnace that surrounds the bottom of the cell. The Leitz

Orthoplan microscope is equipped with interchangeable objectives (H 20X is the most convenient), a λ retarder plate and a polarizer. A color NEC camera is mounted on the microscope and connected to a PANASONIC video-recorder and a NEC Monitor to follow the carbonization reactions in situ. Temperature, pressure, time and size data are displayed on the screen. The cell is connected through 1/32" tubing to a gas system that supplies hydrogen or nitrogen at regulated pressures.

RESULTS AND DISCUSSION

The development of mesophase starts with the appearance of sub-micrometer spherulites (Figure 2-a) that grow in size and occasionally also in number (Figure 2-b) and coalesce (Figure 2-c) until forming a bulk mesophase (Figure 2-d) that is characteristic of the nature (mainly the distribution of carbon atom types) of the feedstock. The time for the appearance of mesophase spherulites and the coalescence period are recorded and related to the nature of the starting material and operating conditions.

A wide range of feedstocks have been evaluated in order to observe the widest range of mesophase structures to be included in the classification. This includes the case where coalescence of mesomorphic structures did not develop, leading only to isolated small spherulites, indicating no bulk formation of graphitizable carbon. Figure 3-a represents the smallest size of coalesced anisotropic structures (less than 1 μm) called fine grained mosaics, characteristic of low grade anode coke. Figure 3-b represents an improvement in the extension of aromatic layers where basic anisotropic structures can reach 50 μm , coalesced in what is named as coarse flow mosaic. Figure 3-c represents the case of extended flow domain mosaics characterized by homogeneous anisotropic structures with internal disclinations (defects caused by the folding patterns of the aromatic layers). Larger sizes (ranging from 50 to over 500 μm) correspond to higher degrees of graphitizability. This type of structure is characteristic of high quality needle coke. Finally, Figure 3-d represents the case of non-restricted flow domain mosaic: the actual size is imposed by the geometrical configuration of the micro-cell but the fluid nature of the material would make it spread over larger surfaces if available. This is characteristic of good feedstocks for carbon fiber production.

In addition to characteristic size and shape of the final mosaic, there are typical kinetic parameters (mesophase formation and coalescence period) associated with each material (Table 1): longer coalescence periods appear to be associated with granular and coarse flow mosaics, but no relation is observed with formation time.

To further explore this aspect, one of the feedstocks (FCC Decanted Oil) was fractionated (HPLC) into four constitutive fractions: saturates, aromatics, polar aromatics and asphaltenes. Each one of the fractions was evaluated under the same carbonization conditions (700 psig hydrogen, 50 °C/min, 30-450 °C). Figure 3 shows the differences in the final mosaic: the restricted (250 μm) flow domain mosaic of the original feedstock (Figure 3-a) is increased largely (430 μm) for the aromatic fraction (Figure 3-b), but reduced for the polar aromatic (Figure 3-c) and asphaltene (Figure 3-d) fractions, while the saturates fraction volatilizes completely and does not form mesophase. In addition, the asphaltene fraction exhibited a fast formation time similar to that of the feedstock (Table 2), while polar aromatic and aromatic fractions were characterized by longer times. The opposite tendency was observed for the coalescence period. This can be interpreted to mean that the asphaltenes fraction (even though in very small concentration), by initiating its mesophase development, provides the path for catalyzing/promoting the development of mesophase of other fractions, with a final result that is dependent upon the interactions of carbon atom types present in the reacting material.

Research was also performed to evaluate the ability to modify the carbonization process of a particular material (FCC Decanted Oil). Mixing with other feedstocks generally result in a balanced compromise: when mixed with Lube Oil Extract (Figure 4-a) that exhibits no bulk mesophase but isolated spheres, the final mosaic (Figure 4-b) was a collection of poorly coalesced and small anisotropic regions; when mixed with a conversion residue (Figure 4-c) that exhibits coarse flow, the final mosaic was an agglomerate (Figure 4-d) of several flow domain regions. Distillation (Figure 5 a-b) also alters the final mosaic: higher cut point residues tend to result in larger anisotropic structures. On the other hand, hydrodesulfurization (Figure 5-c) significantly reduced the size of the final mosaic. Operating the carbonization process at higher pressures (1500 psig) results in larger mosaics.

Thermal treatments (Figure 6 a-d) considerably increase the size of the final mosaic, particularly at long times and relatively low temperatures, producing a pitch that transforms into

non-restricted (fluid) flow domain (Figure 6-c), suitable for carbon fiber production; however increasing the severity of the process results in a heterogeneous and solid bulk mesophase (Figure 6-d).

CONCLUSIONS

In situ monitoring of mesophase development by hot stage polarized light microscopy has been complemented with a classification of final mosaic structures and applied to elucidate the effect of constitutive fractions, mixtures and pretreatment processes upon the carbonization behavior of petroleum residues, providing a technique for selecting graphitizable carbon (needle coke, carbon fibers) precursors.

BIBLIOGRAPHY

1. Feintuch, H.M. et al., in Handbook of Petroleum Refining, pp. 3-61, McGraw-Hill (1986)
2. Lewis, I.C. and Singer, L.S., in Polynuclear Aromatic Compounds, pp. 269-285, ACS (1988)
3. Marsh, H. and Smith, J., in Analytical methods for coal and coal products, Vol. 2, pp.371-414, Academic Press (1978)
4. Brooks, J.D. and Taylor, G.H., Carbon, 3:185-193 (1966)
5. Patrick, J.W. et al., Fuel, 52(3):198-204 (1973)
6. Marsh, H. and Menendez, R., in Introduction to Carbon Science, pp. 37-73, Butterworths (1989)
7. Marsh, H. and Latham, C.S., in Petroleum Derived Carbons, pp 1-28, ACS (1986)
8. Ke-shun, S., 19th Bien. Conf. Carbon, pp.176-177 (1989)
9. Sunago, H. et al., 19th Bienn. Conf. Carbon, pp. 102-103, (1989)
10. Perrota, A.J. et al., High Temp. High Pres., 13(2):159-166 (1981)
11. McCullough, J.P., University of Pittsburgh, 1984

ACKNOWLEDGEMENTS

This work has been financially supported by INTEVEP S.A. (R&D Center of Petroleos de Venezuela). Special thanks are due to Carlos Mota, project leader. Also we appreciate the assistance of Michael Wen, Dave Herrick and Larry Herman.

Table 1. Classification of delayed coking feedstocks for anode and needle coke.
(Based on dynamic hot stage microscopy at 450 °C, 50 °C/min and 700 psig hydrogen)

Material	Aromaticity ¹³ C nmr wt%	Mesophase formation min	Coalescence period min	Optical Texture Size, μm	Uses
Lube Oil Extract	29.30	5	No	Spheres	None
Heavy Crude Oil	37.30	11	11	<1	Anode
Conversion Residue	41.43	9	13	10-50	Anode
FCC Decanted Oil	52.73	2	3	250-500	Needle
Petroleum Pitch A-240	88.61	18	-	>500	Needle, Fibers

Table 2. Mesophase development of FCC Decanted Oil HPLC fractions.
(Based on dynamic hot stage microscopy at 450 °C, 50 °C/min and 700 psig hydrogen)

Material	Yields wt %	Mesophase formation min	Coalescence period min	Optical Texture Size, μm
FCC Decanted Oil	-	2	3	250
HPLC Fractions				
Saturates	26.8	No	No	-
Aromatics	67.3	12	3-10	430
Polar Aromatics	4.7	9	25	50
Asphaltenes	1.2	2	>37	<1

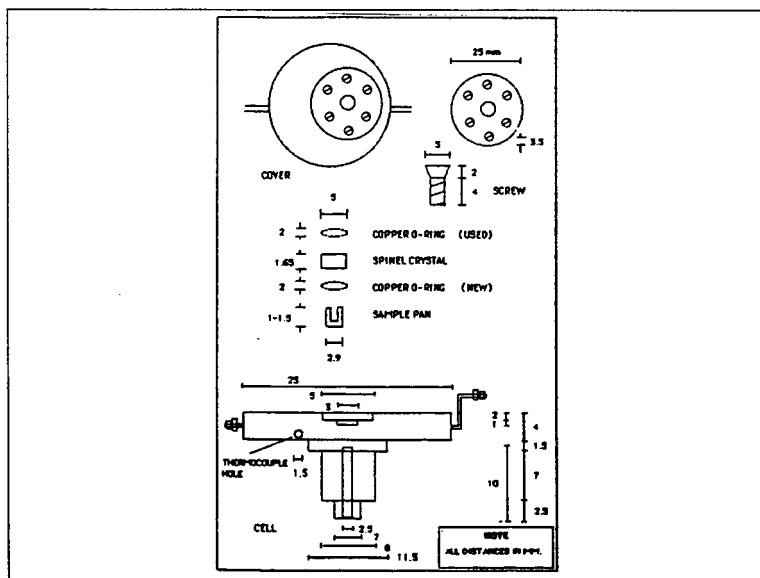


Figure 1. High Temperature High Pressure Micro-cell

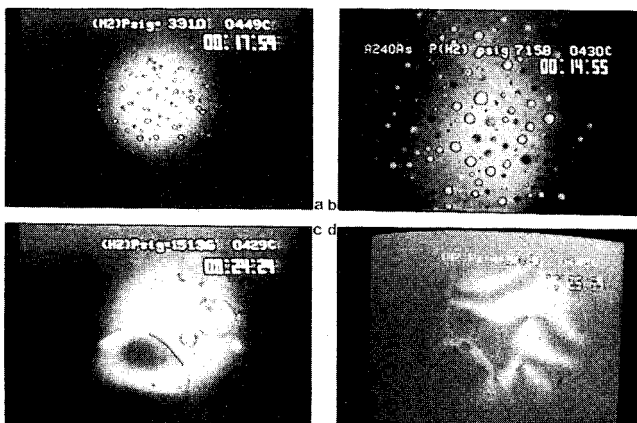


Figure 2. Evolution of mesophase development: (a) appearance, (b) growth, (c) coalescence, (d) final mosaic (screen size: 475 μm)

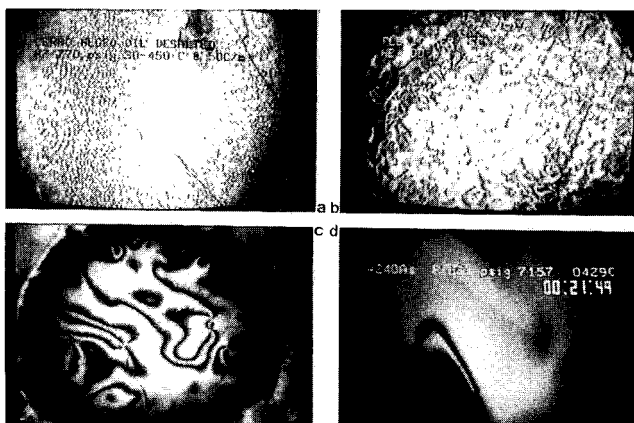


Figure 3. Classification of final mosaic: (a) fine grain, (b) coarse flow, (c) flow domain, (d) fluid flow domain (screen size: 475 μm)

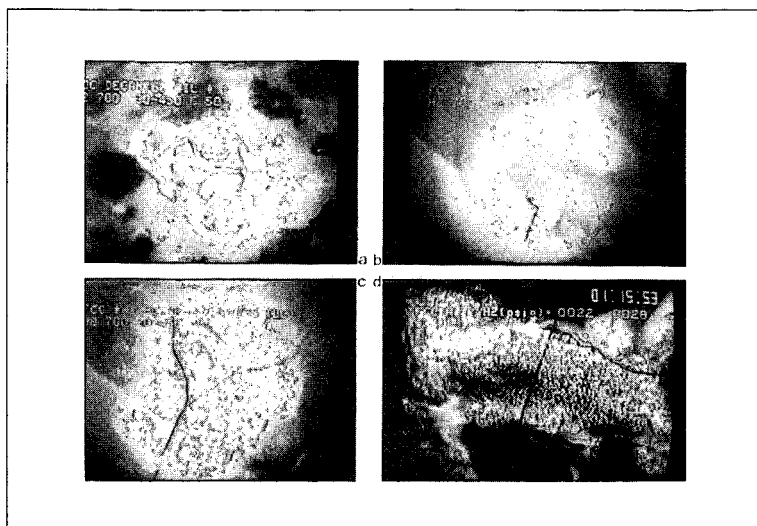


Figure 4. Final mosaics of HPLC fractions: (a) FCC Decanted Oil, (b) Aromatics, (c) Polar aromatics, (d) asphaltenes (screen size: 475 μm)

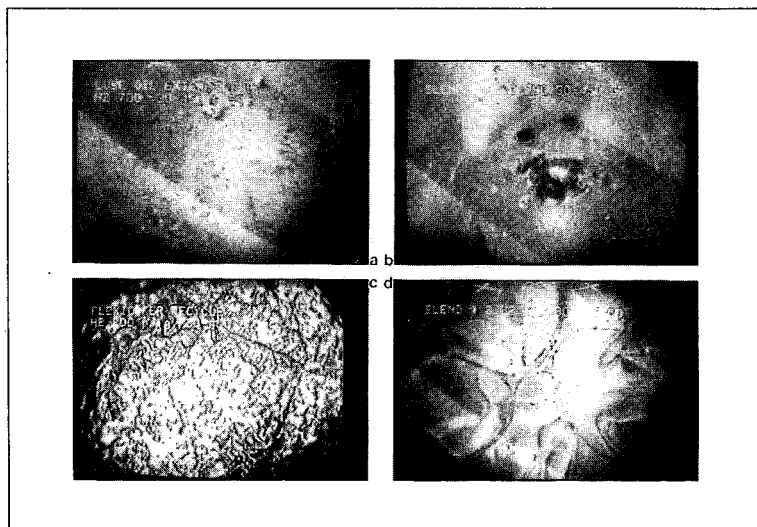


Figure 5. Final mosaics of mixtures: (a) Lube Oil Extract, (b) 70% FCCDO & 30% LOE, (c) Conversion residue, (d) 70% FCCDO & 30% CR (screen size: 475 μm)

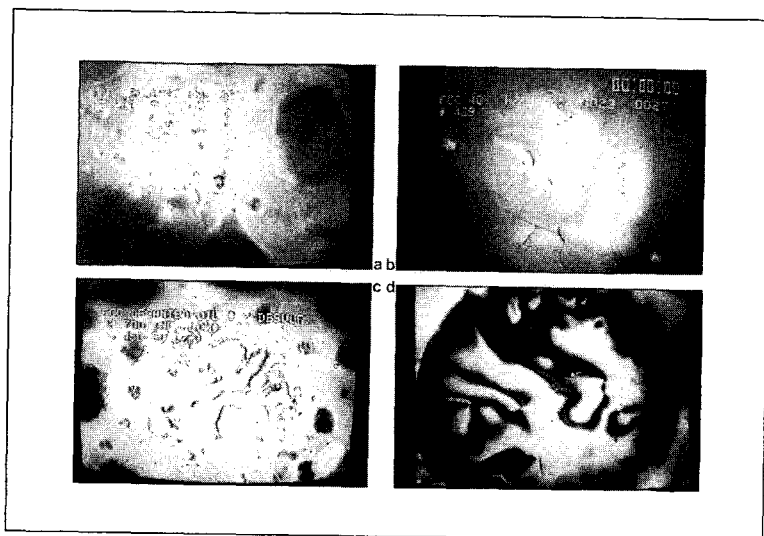


Figure 6. Final mosaics of pretreated materials: (a) Distillation bottoms 63%, (b) Distillation bottoms 40%, (c) Desulfurized, (d) High pressure carbonization (screen size: 475 μ m)

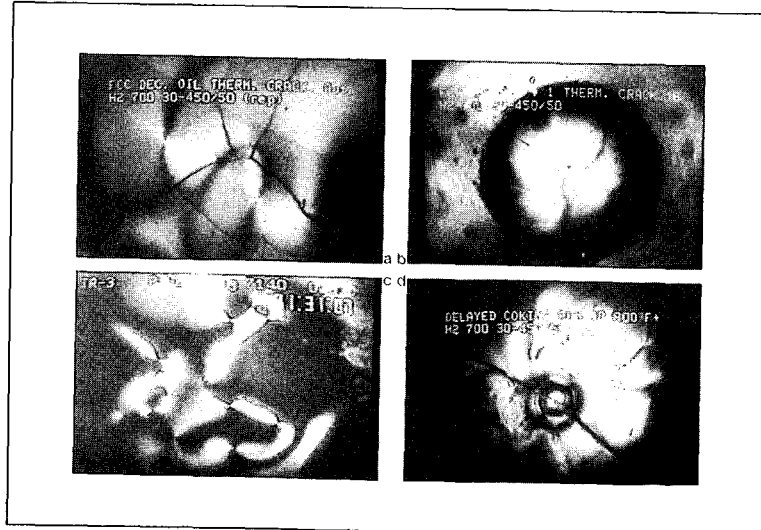


Figure 7. Final mosaics of pretreated materials: (a) Autoclave thermal cracking, (b) Pilot plant thermal cracking, (c) Severe thermal cracking (long time), (d) Delayed coking residue (screen size: (a) 190 μ m, (b-d) 475 μ m)

DEVELOPMENT AND TESTING OF CARBON PISTONS

J. Heuer

Research, Structural Materials
Daimler-Benz Aktiengesellschaft
7000 Stuttgart 80
Germany

INTRODUCTION

The research department of Daimler-Benz has been developing carbon pistons for combustion engines for about 3 1/2 years. In this context "carbon" means graphite without the addition of reinforcing fibres.

Although the development of the material would itself without doubt be an essential topic, this paper is restricted to the application of the material and treats the matter from the view of a mechanical engineer.

The project "Development of Carbon Pistons" is a joint project in which several partners and sub-contractors are working together and is sponsored by the German Ministry for Research and Technology.

REASONS FOR THE DEVELOPMENT OF CARBON PISTONS

Today, aluminum alloy is generally used for mass produced pistons. However, graphite has several advantages in comparison with aluminum. The most important differences are shown in Fig. 1.

The density of graphite is much lower than that of aluminum alloy. Other favorable properties of graphite are the lower coefficient of thermal expansion and the higher resistance to heat. Unfavorable is that the tensile strength of graphite at room temperature is comparatively low. However, considering the tensile strength as a function of temperature, as shown in Fig. 2, you see that the strength of aluminum alloy drops at temperatures above 160 °C. In contrast to this the tensile strength of graphite even increases slightly with temperature.

On the basis of these graphite material properties the following advantages can be expected if the material is applied to pistons:

- a reduced piston weight because of the lower material density,
- a smaller piston clearance because of the low coefficient of thermal expansion.
- Furthermore, it can be expected that the carbon piston transmits less noise because of the material's damping capacity.
- Another advantage of graphite are the excellent emergency frictional properties, which make piston scuffing impossible.

These were the advantages which triggered our development of carbon pistons. As we will see later on, the carbon piston lived up to our expectations, and showed even more improvements.

DESIGN AND FABRICATION

A carbon piston was designed and built to fit into an existing production engine. As a test bed, the engine of the Mercedes-Benz model 190 E was chosen. This engine is a 4-stroke-4-cylinder-gasoline engine with a displacement of 2 litres and a bore of 89 mm.

Carbon pistons were manufactured by turning and milling from the solid with the aid of numerically controlled machines. The material for the pistons came from Poco Graphite, Inc., Decatur, Texas, which had the highest strength of all standard grades in the market.

TESTS OF FUNCTIONALITY AND DURABILITY

After the first carbon pistons were built, their functional test followed. At first, only one carbon piston was installed in the 4-cylinder engine, which was mentioned before, together with 3 standard pistons. The carbon piston was equipped with standard piston rings and a normal connecting rod but with a ceramic piston pin of silicon nitride. The engine was tested on a simple engine bench. This bench was used employing a moderate test program with alternating loads.

After 56 hours on the bench the engine was dismantled for inspection. The carbon piston and the ceramic piston pin were in an excellent condition.

At the beginning of 1989 an engine was equipped for the first time with 4 carbon pistons and 4 ceramic piston pins. The carbon pistons and the ceramic piston pins had thicker walls than the conventional metallic parts to compensate for the inferior strength. In spite of this fact the total weight of the carbon pistons and the ceramic piston pins was 20 % less than that of the corresponding metallic production parts.

This first engine, which was completely furnished with carbon pistons, was tested for 120 hours on the bench according to a rather severe test program, where almost 40 % of the running time the engine was at full load. In this program the engine was under much more load than in normal road traffic. After 120 hours the engine was disassembled and the carbon pistons and the ceramic piston pins were inspected. All components were in an excellent condition, and could be used again.

Thus the engine was reassembled and installed in a test car - a Mercedes-Benz model 190 E. In this car the engine with carbon pistons accumulated more than 15 000 miles without any trouble. The car was used by all colleagues of our department on public roads - i. e. in city - and long distance traffic. In consideration of the safety of the driver, the engine speed was restricted not to exceed

4 000 rpm. This was the only restriction.

During the road test the engine performed very well all the time. Compression graphs, which were taken before and after a distance of 15 000 miles, indicated no difference and thus a continuing good engine condition. Fig. 3 shows a carbon after 120 hours on the engine bench and 15 000 miles in the test car.

COMPARISON MEASUREMENT

After the function and a sufficient service life of the engine with carbon pistons had been established, exact measurements could be started. With the aid of these tests the expected and possible other advantages of carbon pistons in comparison to today's production pistons should be evaluated.

For the comparison measurements only one engine was used to avoid the influence by tolerances of different engines. So at first all tests were performed with carbon pistons. Then the carbon pistons and the ceramic pins were replaced by their series counterparts.

The evaluations concerned mainly the following items:

- fuel consumption
- oil consumption, and
- exhaust emissions

Fuel consumption and exhaust emissions were determined in an official test program, which is called 14-points-CVS-test. This test corresponds to city traffic.

The oil consumption was measured in a special trial run. In this test, the engine continuously ran for three hours under full load conditions at an engine speed of 4500 rpm.

The most important results of the comparison measurements are compiled in Fig. 4. All data are relative and related to the production engine with aluminum pistons. This figure indicated that the engine with carbon pistons performed better in all points than the production engine. Concerning exhaust emissions the improvements with the engine using carbon pistons were 20 % with respect to hydrocarbons (HC), 30 % concerning carbon monoxide (CO), and 3 % concerning nitrogen oxides (NO_x). A slight improvement of 3 % was also achieved with respect to fuel consumption. The largest improvement, however, was observed in oil consumption. The carbon piston engine consumed only 44 % of the lubricating oil which the standard engine needed.

CONCLUSIONS

With the use of top quality graphites, which are available on the market, it was possible to reduce the piston weight by 10 %. Another weight reduction of 10 % was realized by the application of a ceramic piston pin. Thus in a first approach the weight of the piston/piston pin assembly was already 20 % less than with the

corresponding production parts.

Function and service life could be demonstrated up to a maximum engine speed of 5 100 rpm.

Comparative tests so far revealed no disadvantages for the engine with carbon pistons. Slight improvements - in the order of 3 % - were measured with respect to power output and fuel consumption. However, one must bear in mind that all improvements were attained by a simple replacement of successful production components. Up to now, no optimization has been undertaken - neither of the carbon piston nor of the engine with respect to the special properties of graphite.

The engine with carbon pistons showed very important and clear improvements concerning exhaust gas emissions and oil consumption. Therefore, the application of carbon pistons could help to reduce environmental pollution, and to extend the useful life of the catalyst. The improvement regarding the emission of hydrocarbons is especially essential, because this constituent is difficult to diminish when the catalyst is not yet at operating temperature.

Before the carbon piston will be suitable for mass production there are at least two pre-requisites which have to be accomplished: Firstly, the tensile strength of the graphite must be improved. This is necessary to allow at the same time a further weight reduction of the piston, and to meet the requirements of full engine speed.

Secondly, economic production methods must exist which are suitable for series production.

			Aluminum alloy	Graphite
Density	ρ	g/cm ³	2.70	1.83
Coefficient of linear expansion	α	1/K	21·10 ⁻⁶	6·10 ⁻⁶
Modulus of elasticity	E	GPa	80	11
Thermal conductivity	λ	W/mK	150	80
Melting temperature	T	°C	380	460
Tensile strength	σ_B	MPa	225	70

Figure 1. Material Data of Aluminum Alloy and Graphite

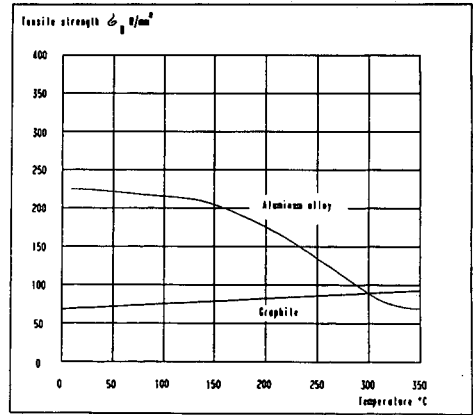


Figure 2. Tensile Strength of Aluminum Alloy and Graphite



Figure 3. Carbon Piston after 120 hours on Engine Bench and 15000 miles in Test Car.

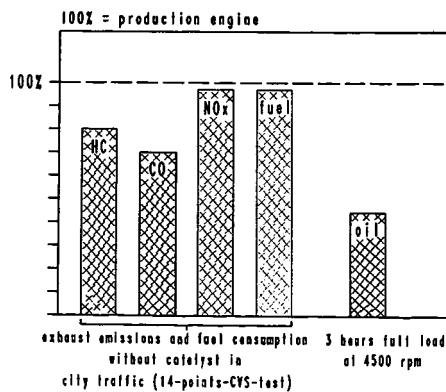


Figure 4. Engine with Carbon Pistons compared to Production Engine.

CARBON AND GRAPHITE MATRICES IN CARBON-CARBON COMPOSITES: AN OVERVIEW OF THEIR FORMATION, STRUCTURE, AND PROPERTIES

Gerald Rellick

Mechanics and Materials Technology Center, Technology Operations
The Aerospace Corporation, P.O. Box 92957, Los Angeles, CA 90009

Keywords: Carbon-carbon composites, Graphitization, Composite properties

WHY CARBON-CARBON COMPOSITES?

Carbon-carbon (C/C) composites, so-called because they combine carbon-fiber reinforcement in an all-carbon matrix, can best be viewed as part of the broader category of carbon-fiber-based composites, all of which seek to utilize the light weight and exceptional strength and stiffness of carbon fibers. However, in C/C, the structural benefits of carbon-fiber reinforcement are combined with the refractoriness of an all-carbon materials system, making C/C composites the material of choice for severe-environment applications, such as atmospheric reentry, solid rocket motor exhausts, and disc brakes in high-performance military and commercial aircraft. Their dimensional stability, laser hardness, and low outgassing also make them ideal candidates for various space structural applications.

Such mechanical and refractory properties are not met by the various bulk graphites for two reasons: (1) graphites are very flaw sensitive and, therefore, brittle; and (2) graphites are difficult to fabricate into large sizes and complex shapes. These difficulties are largely overcome by taking advantage of the "two phase principle of material structure and strength [1]."

In the classical two-phase materials system, or composite, a high-strength, high-modulus, discontinuous-reinforcement phase is carried in a low-modulus, continuous-matrix phase; e.g., graphite fibers in a thermoplastic-resin matrix. The stress in a composite structure having fiber reinforcement that is continuous in length, is carried in proportion to the moduli of the constituent phases, weighted by their respective volume fractions. Therefore, the much stiffer (higher-modulus) fibers will be the principal load bearers, and the matrix, in addition to having the task of binding together the composite, will deform under load and distribute the majority of stress to the fibers. At the same time, because the brittle carbon fibers are *isolated*, the possibility that an individual fiber failure will lead to propagation and catastrophic failure is practically eliminated.

Another major benefit of composites is that they permit the construction of complex geometries, and in such a way that different amounts of the load-carrying fibers can be oriented in specific directions to accommodate the design loads of the final structure. Closely associated with this "tailoring" feature of composites is that carbon-fiber technology enables exploitation of the exceptional basal-plane stiffness (and strength, in principle, although this is still much farther from realization) of sp^2 bonded carbon atoms—i.e., the fibers are not isotropic, but rather have their graphite basal planes oriented preferentially in the fiber axial direction.

For very-high-temperature carbon-fiber-composite applications, say, above 2000°C, even for brief periods of time, it is necessary to employ a carbon matrix; however, like the fiber, the carbon matrix is also brittle. When fiber-matrix bonding is very strong in C/C, brittle fracture is frequently observed. The explanation is that strong bonding permits the development of high crack tip stresses at the fiber-matrix interface; cracks that initiate in either fiber or matrix can then propagate through the composite. However, if the matrix or the fiber-matrix interface is very weak, or microcracked, then the primary advancing crack can be deflected at such weakened interfaces or cracks. This is the Cook-Gordon theory [2] for strengthening of brittle solids, which states, more specifically, that if the ratio of the adhesive strength of the interface to the general cohesive strength of the solid is in the right range, large increases in the strength and toughness of otherwise brittle solids may result. Therefore, good fiber strength utilization in a brittle-matrix composite like C/C depends on control of the matrix and interfacial structures.

The objective of this paper is to provide a brief overview of carbon and graphite matrices in C/C, with an emphasis on recent research on some of the more fundamental materials issues involved [3-7]. Much of what is presented is taken from our own published work, which has focused on understanding how the structure of

the carbon or graphite matrix, and fiber-matrix interphase region, is influenced by starting materials and processing methods, and, in turn, how these structures affect composite properties. For comprehensive reviews of C/C, the reader is referred to Fitzer [8,9] for an overview of the basic materials issues, and to McAllister and Lachman [10] for a thorough treatment of fabrication and processing issues. Less comprehensive but more recent reviews that build principally on those just cited but that also deal with more specialized topics, such as oxidation protection of C/C, are contained in Refs. 11-13.

FIBER ARCHITECTURE AND PREFORM DENSIFICATION

The composites designer, in addition to being able to choose from a wide variety of fiber types, also has a large number of fiber architectures available. For high-performance C/C applications, continuous (in length) fiber reinforcement is integrated to produce either a two-dimensional (2-D) or three-dimensional (3-D) fabric preform. According to Ko [14], a fabric preform is defined as "an integrated fibrous structure produced by fiber entanglement or yarn interlacing, interlooping, intertwining, or [nonwoven] multiaxial placement."

The preform may be dry, i.e., unimpregnated, as in 3-D orthogonal block structures, in which the x, y, and z yarns are "laid-in" straight to produce a structure having about 60% void volume (see Fig. 1a). The yarns may also be pultruded, i.e., impregnated with a resin binder and formed into rigid rods.

Alternatively, the fabrics may be impregnated with a thermosetting-resin binder and then the fabric plies laid up to produce the desired component (Fig. 1b). Such a structure is still termed 2-D because of the lack of through-thickness reinforcement.

To produce a C/C, the carbon-resin composite is baked, or fired, to pyrolyze the organic matrix. If the fabric is initially impregnated with a state-of-the-art phenol formaldehyde resin system, we can expect to obtain a C/C part with approximately 25% residual porosity after baking. However, experience has shown that such porosity is excessive, and that significant improvement in properties will follow if the porosity is reduced to values in the 5-15% range, depending on the particular type of structure. Therefore, not only in the dry preform, but also in the pyrolyzed "prepreg" fabric, additional volume increments of carbon matrix must be introduced into the C/C structure. The introduction can be achieved by one or a combination of three densification processes: CVI, use of coal-tar and petroleum pitches, and use of thermosetting resins. As each of these processes is discussed in turn, we will explore its characteristic structural features and densification behavior, and effects on properties. This discussion will also be used as an opportunity to introduce and discuss the various C/C characterization tools and techniques: X-ray diffraction, laser Raman microprobe spectroscopy, density measurements, and, particularly, polarized-light microscopy, and scanning and transmission electron microscopy (SEM and TEM).

CVI

The first method for C/C densification, chemical vapor infiltration (CVI) [15,16], involves the passage of a hydrocarbon gas, typically methane, through the porous preform at temperatures in the 1000-1200°C range, with resulting deposition of carbon in the open porosity. Such low-temperature CVI leads to three principal carbon microstructures as defined by polarized-light microscopy [17-19]: rough laminar (RL), smooth laminar (SL), and isotropic. Isotropic deposits are generally very low density and of little value in C/C densification. Examples of RL and SL carbons in a PAN-based carbon-fiber composite are shown in the polarized-light micrographs of Figs. 2a and b.

A characteristic feature of both the RL and SL carbons is the set of extinction crosses observed under cross-polarized light. Such crosses are a consequence of the oriented nature of the deposits; the carbon layer planes align preferentially along the fiber surface. The anisotropic structure leads to a condition of birefringence in which two of the three principal crystallographic axes of graphite oriented at 90 deg to each other have different indices of refraction. Examination of Figs. 2a and b reveals two patterns of RL and SL deposits, illustrating that not only the amount but the type of carbon deposition can vary throughout the structure, depending on local temperature and gas concentration gradients [17].

In addition to orientation, another important feature of carbon matrices is their graphitizability, which is a measure of the ease in converting the pyrolyzed carbon matrix product into crystalline graphite through high-temperature heat treatments in the ~ 2000 – 3000°C range. The state of graphitization can be assessed by a number of techniques, the most common of which is X-ray diffraction (XRD). However, in C/C it is usually very difficult to resolve the resultant composite diffraction response into the respective fiber and matrix responses, because both phases are carbon. A technique to circumvent the sample volume problem is laser Raman microprobe spectroscopy (LRMS). Although the interpretation of the Raman spectra is more ambiguous than with XRD, LRMS permits focusing of a visible-light beam, as small as $1\text{ }\mu\text{m}$ in diameter, on a region of the specimen while recording the Raman spectrum, which is active in carbon [20]. Useful structural information on a local scale can be obtained in principle.

One major difficulty with applying LRMS to composites is that the size of constituent phases is of the order of microns, making it necessary to prepare the specimens for examination using standard optical polishing techniques. Such polishing tends to damage the near-surface structures and leaves behind a thin layer of polishing debris. Since the probe depth of the optical beam is only about 50 nm [20], the Raman spectrum unfortunately becomes a function of the preparation technique [21–23].

A technique we have employed extensively and with good success, and which is an outgrowth of early work performed at Los Alamos Laboratories [24,25], involves SEM examination of specimens that have been polished and then cathodically etched with xenon. When the carbon structure is graphitic, and when the graphite layer planes are oriented perpendicular to the plane of section, we see, typically, a pronounced lamellar texture, as revealed for the inner- and outermost CVI layers in the C/C of Fig. 3. The lamellar texture is the result of differential etching rates of the various microstructural units, the exact nature of which is still not clear. The most likely mechanism is preferential removal at lower-density, less-ordered intercrystalline-type boundaries that separate regions of good crystalline registry; this is seen very dramatically in highly oriented pyrolytic graphites reacted in oxygen [26,27]. The technique is effective, principally, in distinguishing broadly between graphitic and nongraphitic carbon on a scale of microns.

Returning to Fig. 3, this particular specimen has the CVI deposition sequence RL/SL/RL (as determined separately from polarized-light microscopy) and has been heat-treated to 2500°C for 1 hr. The lamellar texture of the RL zones indicates their graphitized structure, whereas the absence of significant texture in the SL zone indicates that the SL structure is essentially glassy carbon. This observation was confirmed by XRD, LRMS, and by selected physical-property measurements [28]. The effect of having a graphitic and well-oriented matrix is illustrated by the higher thermal conductivities for heat-treated RL composites shown in Fig. 4.

Modulus enhancement is another interesting effect of a well-oriented, graphitic matrix (Fig. 5). For the particular pseudo-3-D, felt-based C/C composite of the figure, there were two CVI densifications. Following the first, the composite structure was heat-treated to 2500°C ; the second CVI was left in the as-deposited state (~ 1000 – 1200°C). The relative proportions of the first and second CVI varied with each specimen, but the total CVI weights were approximately the same. The fiber volume (and weight) fraction was constant ($\sim 20\%$) for each composite.

The strong dependence of the modulus on the relative proportion of heat-treated CVI indicates that the carbon matrix can carry a significant fraction of the load, particularly, in this case, if the structure is heat-treated to typical graphitization temperatures. The modulus-enhancement effect by the matrix is especially striking in this composite because of the use of low-modulus fibers at fairly low volume fractions. However, as will be seen, this effect is an important materials and processing consideration in all C/C composites.

Coal-Tar and Petroleum Pitches

The second method for C/C densification is the use of coal-tar and petroleum pitches. Because they are thermoplastic, pitches are used mostly for redensification; i.e., further densifying of a C/C structure that has been "rigidized" by an earlier impregnation/densification step (e.g., a resin-impregnated fabric preform) or that has sufficient rigidity from the friction between the elements of the woven structure (e.g., 3-D braided preform).

Pitches are unique in passing through a liquid-crystalline transformation at temperatures between about 350 and 550°C [29]. In this transformation, large lamellar molecules formed by the reactions of thermal cracking and aromatic polymerization are aligned parallel to form an optically anisotropic liquid crystal known as the carbonaceous mesophase [30]. The alignment of the lamellar molecules is the basis for easy thermal graphitizability of the carbonized product. One of the features of a mesophase-based matrix is high bulk density, which is achievable because the matrix density can approach the value for single-crystal graphite, 2.26 g/cm³.

The topic of pitch impregnation and densification of C/C introduces the subject of densification efficiency, the most meaningful measure of which is *volumetric* densification efficiency [31]. It is the ratio of the volume of carbon matrix in a process cycle to the volume of porosity available for densification.

For pitches carbonized at atmospheric pressure, coke yields are of the order of 50–60%, impregnant densities are ~1.35 g/cm³, and, as we have noted, densities for pitch-derived matrices are ~2.2 g/cm³. From these values we calculate volumetric densification efficiencies of only 30–40% at atmospheric pressure [31]. By resorting to so-called hot isostatic-pressure-impregnation-carbonization (HIPIC), to pressures of about 15,000 psi, carbon yields of pitches can be increased to almost 90% [10]. But even with HIPIC, volumetric filling is only 55%. Therefore, given a preform with initial porosity of 45%, typical for many 3-D woven structures, three cycles at *maximum densification efficiency* would be required to reduce the porosity to 4%. With current HIPIC procedures, however, it is found that at least five cycles at 15,000 psi are required to achieve this same level of porosity. Such reduced efficiency in real systems is the result of forced expulsion of pitch from the preform as a result of the gas-forming pyrolysis reactions accompanying carbonization.

Clearly, one way to increase efficiency, for a given weight-based carbon yield, is to select either an impregnant or an HTT that will lower the final matrix density. As will be seen in the next subsection, lower-density carbon matrices can be achieved by using resin precursors that form a glassy-carbon-type structure. But, although this approach fills more of the available space, it does so with a lower-density carbon matrix, which is different in structure from the higher-density graphitic matrix. The trade-offs in properties, particularly mechanical, are not well understood. We will touch on this topic again in the next subsection.

Approaches to improving densification efficiency of pitch-based matrices without resorting to HIPIC processing include the use of heat-treated and solvent-extracted pitches [32] and partially transformed (to mesophase) pitches [33,34]. A novel approach, developed by White and Sheaffer [35], is to oxidatively stabilize the mesophase following impregnation and transformation, an approach similar to that employed in mesophase-fiber stabilization. The result is a "hardened" mesophase that is resistant to the bloating effects of pyrolysis gases but that, upon further heat treatment, yields a dense, graphitic carbon.

The strong orienting effect of the fiber surface on the large lamellar mesophase molecules is an interesting feature of mesophase formation in C/C composites. This effect was demonstrated by the work of Zimmer and Weitz [36], who used polarized-light microscopy to show that mesophase molecules near a fiber surface in a close-packed fiber bundle always aligned parallel to the fiber surfaces, even in the presence of strong magnetic fields. Singer and Lewis demonstrated earlier that magnetic fields would orient mesophase molecules in *bulk* mesophase [37]. Zimmer and Weitz showed that mesophase would also orient in matrix-rich regions within the fiber bundles—i.e., at points far removed from fiber surfaces [36]. They calculated a magnetic coherence length of 7 μm , which corresponds roughly to the distance over which the orientation effect acts.

Such localized orientation in the liquid-crystalline state would lead one to expect the final, graphitized matrix also to be well oriented in the immediate vicinity of the fiber. First observed by Evangelides [38] using SEM in conjunction with xenon-ion-etching, such a matrix "sheath effect" is depicted in Fig. 6 in a coal-tar-pitch-densified C/C.

Modulus enhancement in pitch-based C/C has been widely reported, but whether the effect is due to the matrix or to an increase in the fiber modulus, resulting from high-temperature heat-treatment-induced structural changes in the fiber, has not been clarified [39]. The sheath effect is also pronounced in resin-based carbon matrices, but for different reasons, which we will examine in the next subsection.

Matrix microcracking is characteristic of all C/Cs, but it is particularly prevalent in graphitic matrices because of the combination of weak shear planes in polycrystalline graphite and the thermal stresses generated during heat treatment (Fig. 7) [40,41]. Microcracking also has important effects on the engineering properties of C/C materials—particularly the matrix-dominated properties in the unreinforced directions, such as the interlaminar shear strength and perpendicular-to-ply tensile strength in 2-D C/C laminates. However, as mentioned above, such microcracking appears to improve in-plane flexural and tensile strength, by way of a Cook-Gordon mechanism [42-45].

Thermosetting Resins

The third, and last, class of C/C impregnant to be discussed is thermoset resins, which are the basis for "prepreg" fabric and tapes, as noted above; resin systems can also be used for reimpregnation. In addition to their easy fabricability, thermosets have the advantage of "charring-in-place;" that is, although they soften and deform on heating, they do not fuse or liquefy, and, therefore, no special tools or techniques must be employed to retain the matrix in the composite during pyrolysis.

Thermoset resins are usually highly crosslinked, which makes them resistant to thermal graphitization in bulk form, even to temperatures of 3000°C [5,46]. Phenolic resins are currently most commonly used for prepreg operations, whereas furan-based resins are used more for reimpregnating. Both have char yields typically in the 50-60% range.

The development of ultra-high-char-yield resins derived from polymerization of diethynylbenzene (DEB) [47-51], usually termed polyarylacetylenes (PAA) [47], has received much focus in recent years. The structure of DEB is illustrated in Fig. 8, along with a synthesis route that involves a catalytic cyclotrimerization prepolymerization in methyl ethyl ketone solvent [48,49]. The cyclotrimerization liberates much of the exothermic heat of polymerization, thereby allowing safe, controllable curing. The principal appeal of PAAs is their extremely high char yield. From the average structure, we calculate a theoretical carbon yield of about 95%; in practice, PAAs can have carbon yields of 90% to 700°C, although more practical formulations employing monofunctional chain terminators to improve flow properties reduce this yield to about 85% [48,49].

Similar to other crosslinked thermosets, PAAs produce largely nongraphitizable carbons. To extend the range of matrix structures for this fabricable resin system, we have been exploring approaches to *in situ* matrix catalytic graphitization in C/C in our laboratory. One promising approach, by Zaldivar *et al.* [52], has been the use of boron in the form of a carborane compound. Figure 9a is a plot of room-temperature tensile strength of undoped and boron-doped unidirectional C/Cs versus HTT; the strengths are calculated relative to the fiber cross-sectional areas on the assumption that the matrix carries negligible load relative to the fibers. The strength of the fibers in the cured-resin composite is taken to be the value for full strength utilization. The plot illustrates a number of important features. First, for the undoped system, strength exhibits a large decrease as the composite proceeds from cure to carbonization, owing to conversion of the compliant polymer matrix into a well-bonded, low-strain-to-failure carbon matrix. Increasing boron levels lead to increased strength utilization for the 1100°C HTT samples: The undoped specimen behaves as a monolithic solid and fractures in a planar-catastrophic mode (Fig. 10a); the 5% B-doped samples exhibit extensive fiber pullout (Fig. 10b), which indicates a weakened interface. The reasons for the weakened interface are unclear, since X-ray diffraction revealed no significant difference in graphitization between doped and undoped specimens after this HTT.

At higher HTTs, the use of higher boron levels leads to a reduction in strength utilization (and an increase in modulus; Fig. 9b), due to catalytic graphitization of the fiber. Further HT of the undoped specimens beyond 1100°C "reclaims" much of the lost fiber strength, for the reasons discussed above. More work is needed to define the mechanisms by which catalytic graphitization of the matrix affects the properties of C/C.

We recently reported a striking modulus enhancement for the same type of 1-D composite studies (Zaldivar *et al.* [7]), using four mesophase-based fibers from DuPont and PAA resin (Fig. 11). The number in the fiber designation is the axial tensile modulus, in Mpsi. For HT to 2750°C, all the composites exhibit sharp increases in fiber moduli, to values exceeding 150 Mpsi, which is the theoretical limit of the graphite basal-plane modulus. Since the moduli are calculated relative to the original fiber cross-sectional areas, such values

indicate that the composite modulus must have significant contributions from the matrix. An example of a matrix sheath that may be contributing to the composite modulus is shown in Fig. 12.

This figure brings us to the subject of stress-induced orientation and graphitization in otherwise nongraphitizing carbon matrices in C/C. While the phenomenon of stress graphitization of hard carbons has been noted for some time [24,25,53,54], only recently have serious efforts have been made to understand the physical-mechanical mechanisms involved in matrix orientation and graphitization in C/C [5,6,55]. This topic is of more than academic interest, because the formation of a two-phase matrix of graphitic and nongraphitic, oriented and unoriented, zones can have a major influence on the mechanical properties of C/C composites.

To examine preferred orientation in thermosetting-resin-impregnated matrices, cross sections of C/C tows fabricated from Amoco T50 PAN-based fibers and a PAA resin were polished, then heat-treated to 2900°C for 1 hr and xenon-ion-etched. The polarized-light micrograph of Fig. 13a reveals that in addition to the pronounced lamellar zones, the smooth-appearing zones—which, by definition, have formed no observable texture with etching—are nevertheless oriented, as evidenced by the polarized-light extinction contours sweeping across the surface of the sample as the analyzer is rotated. We conclude that even the thickest ($> 20\text{ }\mu\text{m}$ matrix regions in this specimen are oriented. Pronounced optical anisotropy in the matrix for the same composite heat-treated to only 1200°C is revealed by Fig. 13b. As expected, etching produced no lamellar texture for this low HTT.

The highly localized nature of the combination of stress-induced orientation and graphitization is one of its more interesting features: i.e., all of the carbon matrix in the specimen of Fig. 13a is oriented to some degree, yet only certain discrete regions become lamellar graphite upon HT to 2900°C. SEMs of ion-etched specimens reveal this localized graphitization more clearly (Fig. 14); particularly striking is the shrinkage of the matrix away from the fiber, which is a result of the volume decrease accompanying graphitization.

TEM is an extremely effective technique for studying the local structure on an even finer scale. In the transverse (Fig. 15a) and longitudinal (Fig. 15b) bright-field images of thin sections of a T50 fiber/resin-derived C/C heated to 2750°C, crystallite formation and orientation are evident, particularly in the transverse section (compare with Fig. 13a). Selected area electron diffraction confirmed the highly crystalline structure of the interfilament matrix regions [56].

In the SEM of Fig. 16a, we observe an interesting effect: At the interstice of five contiguous fibers there is no lamellar formation in the matrix pocket, except perhaps immediately adjacent to the filament surfaces. This effect was typically observed in close-packed groups of three to five fibers. In contrast, in more extensive matrix regions—for example, those that bound two relatively fiber-rich areas, and where the matrix boundaries are fairly straight—we observe relatively unimpeded development of lamellar structure over a distance of several microns (Fig. 16b). Such lamellar development is particularly striking at the extreme outside of the single-tow specimens where quite thick ($\sim 1\text{--}2$ fiber diameters) lamellar zones form (Fig. 16c). In Fig. 16d, we see that an interruption in the uniformity of the interface between this outer matrix crust and the composite leads to a transition from the lamellar to nonlamellar structure.

Further microstructural features not seen in polished specimens are revealed in the SEM of a tensile-fracture surface (Fig. 17). The lamellar regions in the matrix are still evident, and the PAN-based fibers show their typical fibrillar structure. But we now observe in the matrix both lamellar and fibrillar textures, the latter resembling that seen in the T50 fibers, which are generally considered to be oriented glassy carbon [46].

Two observations suggested to us that the key factor in determining lamellar-structure formation in a C/C composite matrix is a *multiaxial* deformation of the resin during its pyrolysis to carbon. First, consider that, in normal PAN-fiber manufacture, which leads to a fibrillar structure, the filaments are subjected to a uniaxial tensile stress during oxidation stabilization. However, when carbonized without prior oxidation stabilization, but in *very thin sections*, such as between the layers of montmorillonite clay, PAN has been shown to yield a single-crystal structure following subsequent graphitization heat treatment [57]. Second, in partially oxidized (through-the-thickness) PAN fibers, the unoxidized, fusible core can form lamellar carbon [58].

In both examples, the mechanical restraints imposed on the PAN during its pyrolysis would be expected to produce multiaxial deformation. In this critical regime, a number of stresses act at the fiber-matrix interface, assuming good fiber-matrix adhesion: First, there is an axial tensile stress that acts on the matrix; it is a consequence of the large matrix pyrolysis shrinkage, and the high axial modulus and low axial thermal expansion of the fiber. This matrix shrinkage also generates two additional matrix stresses in the plane perpendicular to the axial direction—a compressive stress, which acts radially, and a tensile stress, which acts circumferentially.

We tested this hypothesis by performing a linear elastic plane-strain thermal stress analysis for three different local fiber-matrix composite configurations: a clustered arrangement of three fibers and four fibers, sketched in Figs. 18a and b, respectively, and a matrix with free boundaries. These three cases correspond closely to those seen in Figs. 16a-d. The material properties used for the PAN fiber and phenolic-resin matrix are typical values obtained from a variety of sources. The mechanical properties of the pyrolyzing matrix are those reported by Fitzer and Burger [59]. The thermal environment was a heatup from room temperature to 1000°C.

In the analysis we are concerned only with the stresses in the matrix in the plane perpendicular to the fiber axis, because the tensile stress of the matrix in the fiber direction at any point in the matrix is clearly more or less constant at a given temperature owing to the plane-strain consideration. The stresses in the radial-tangential plane may vary significantly, depending on their relative location to the fiber. At any point in the matrix, therefore, we have a state of triaxial stress.

The development of lamellar structure in the matrix was postulated to be favored by two factors: (1) a large value of the maximum tensile stress in the plane, and (2) a small value of the ratio of minimum-to-maximum principal stress in this same plane. That is, for a given value of maximum tensile stress in the matrix, lamellar formation is favored more when the minimum-to-maximum stress ratio at any location is either small or negative (i.e., compressive). These two parameters may vary with the fiber spacing and boundary conditions, e.g., constrained or free edge.

Figure 19a, a plot of principal stress orientation and relative stress magnitudes, indicates that the maximum stress adjacent to the outside diameter of each fiber is dominated by hoop tension with a very low level of radial tensile stress; by contrast, the maximum stress in the center of the pocket is equal to about one-third that at the fiber surface, and the minimum (tensile) stress is now significant. From our hypothesis, these two factors will work in the direction of reduced lamellar formation relative to that at the fiber surface.

The effects of an increase in the a/r ratio (Fig. 18) are to decrease the maximum hoop stress at the fiber-matrix boundary and increase the stress ratio in the pocket region. In other words, when the three fibers are more closely packed, the formation of lamellar structure at the fiber surface is more favored than when they are loosely packed; however, within the pocket, it is less favored. Similar results were found for the four-fiber case.

We used the model of Fig. 18b to make the calculation for the free-boundary condition occurring along a straight, resin-rich area; the stress in the matrix along the free boundary is primarily unidirectional. Figure 19b illustrates that the relative stress magnitude and orientation correlate with the location of formation of lamellar structure depicted in Fig. 16c.

In conclusion, it is seen that the magnitude and orientation of the matrix shrinkage stresses during pyrolysis, as estimated by this analysis, are consistent with the proposed model for stress orientation and graphitization.

Much still remains to be learned about matrix stress graphitization in C/C: e.g., the effects of fiber type, fiber volume, matrix precursor, and high-temperature creep deformation. Equally intriguing is the possibility of being able to control C/C properties by controlling the matrix orientation and graphitization behavior.

SUMMARY

Carbon-carbon composites are an exceptional class of high-strength, low-weight refractory materials; however, effective utilization of the carbon fiber properties requires appropriate selection of the carbon or graphite matrix and processing conditions. The matrices may be derived from hydrocarbon gases, coal-tar and petroleum pitches, and thermosetting resins, and represent a range of structures and properties. Current research is beginning to elucidate how C/C composite properties may be controlled by controlling the structures of the matrix, both in bulk matrix regions and, more sensitively, at the crucial fiber-matrix interphase region.

ACKNOWLEDGMENTS

This paper reviews selected aspects of work funded by the Air Force Space Systems Division under Contract No. F04701-88-C-0089, and by the Aerospace Sponsored Research Program. The author wishes to thank a number of coworkers: Rafael Zaldivar, particularly, who, as an Aerospace MS and PhD Fellow, is responsible for much of the work discussed here; Dr. Dick Chang for his effective collaboration on portions of this work; and Paul Adams, Jim Noblet, Ross Kobayashi, Joe Uht, Dick Brose, and Ca Su, all of whom contributed in significant ways.

REFERENCES

1. Slayter, G., *Sci. Am.*, 124 (January 1962).
2. Cook, J., and Gordon, J. E., *Proc. R. Soc. London A282*, 508 (1964).
3. Jortner, J., *Effects of Weak Interfaces on Thermostructural Behavior of C-C Composites*, Office of Naval Research, Annual Report, pp. 19-31 (March 1985).
4. Peebles, L. H., Meyer, R. A., and Jortner, J., In *Interfaces in Polymer, Ceramic and Metal Matrix Composites*, H. Ishida, Ed., p. 1, Elsevier (1988).
5. Zaldivar, R. J., and Rellick, G. S., "Some Observations on Stress Graphitization in C-C Composites," *Carbon* (in press).
6. Rellick, G. S., Chang, D. J., and Zaldivar, R. J., *Ext. Abstr., 20th Carbon Conf.* (1991), p. 404.
7. Zaldivar, R. J., Rellick, G. S., and Yang, J., *Ext. Abstr., 20th Carbon Conf.* (1991), p. 400.
8. Fitzer, E., *Carbon* 25, 163 (1987).
9. Fitzer, E., and Huttner, W., *J. Phys. D: Appl. Phys.* 14, 347 (1981).
10. McAllister, L. E., and Lachman, W., In *Handbook of Composites*, A. Kelly and S. T. Mileiko, Eds., Vol. 4, p. 109, Elsevier (1983).
11. Hsu, S. E., and Chen, C. I., In *Superalloys, Supercomposites and Superceramics*, p. 721, Academic Press (1989).
12. Buckley, J. D., *Ceram. Bull.* 67, 364 (1988).
13. Strife, J. R., and Sheehan, J. E., *Ceram. Bull.* 67, 369 (1988).
14. Ko, F., *Ceram. Bull.* 68, 401 (1989).
15. Bokros, J. C., In *Chemistry and Physics of Carbon*, P. L. Walker, Jr., Ed., Vol. 5, p. 1, Dekker, NY (1969).
16. Kotlensky, W. V., In *Chemistry and Physics of Carbon*, P. L. Walker, Jr., Ed., Vol. 9, p. 173, Dekker, NY (1973).
17. Pierson, H. O., and Lieberman, M. L., *Carbon* 13, 159 (1975).
18. Granoff, B., *Carbon* 12, 405 (1974).
19. Loll, P., Delhaes, P., Pacault, A., and Pierre, A., *Carbon* 15, 383 (1977).
20. (a) Tuinstra, F., and Koenig, J., *J. Chem. Phys.* 53, 1126 (1970); (b) *J. Compos. Mater.* 4, 492 (1970).
21. Miller, T. G., Fischbach, D. B., and Macklin, J. M., *Ext. Abstr., 12th Carbon Conf.* (1975), p. 105.
22. Vidano, R., and Fischbach, D. B., *Ext. Abstr., 15th Carbon Conf.* (1981), p. 408.
23. Katagairi, G., Ishida, H., and Ishitani, A., *Carbon* 26, 565 (1988).
24. Chard, W. C., Reiswig, R. D., Levinson, L. S., and Baker, T. D., *Carbon* 6, 950 (1968).
25. Reiswig, R. D., Levinson, L. S., and O'Rourke, J. A., *Carbon* 6, 124 (1968).
26. Rodriguez-Reinoso, F., and Thrower, P. A., *Carbon* 12, 269 (1974).
27. Rellick, G. S., Thrower, P. A., and Walker, P. L., Jr., *Carbon* 13, 71 (1975).
28. Rellick, G. S., *Ext. Abstr., 20th Carbon Conf.* (1991), p. 368.

29. Brooks, J. D., and Taylor, J. H., *Nature* **206**, 697 (1965).
30. White, J. L., In *Prog. Solid State Chem.*, J. O. McCauldin and G. Somarjai, Eds., Vol. 9, p. 59, Pergamon Press (1975).
31. Rellick, G. S., *Carbon* **28**, 589 (1990).
32. Zimmer, J. E., and Salvador, L. M., U.S. Patent 4,554,024 (19 November 1985).
33. Brückmann, H., Dr.-Ing Thesis, University of Karlsruhe (1979).
34. Singer, L. S., Lewis, I. C., and Bacon, R., *Proceedings of the JANNAF Rocket Nozzle Technology Subcommittee Meeting*, Naval Surface Warfare Center, Silver Spring, MD (17-19 October 1989).
35. White, J. L., and Sheaffer, P. M., *Carbon* **27**, 697 (1989).
36. Zimmer, J. E., and Weitz, R. L., *Carbon* **26**, 579 (1988).
37. Singer, L. S., and Lewis, R. T., *Ext. Abstr.*, *11th Carbon Conf.* (1973), p. 207.
38. Evangelides, J. S., *Ext. Abstr.*, *12th Carbon Conf.* (1975), p. 93.
39. Jortner, J., Appendix A in Ref. 3 above.
40. Jortner, J., In *Proc. Army Symp. on Solid Mechanics*, AMMRC MS 76-2 (1976), pp. 81-97.
41. Jortner, J., *Carbon* **24**, 603 (1986).
42. Buch, J. D., *Structure-Property Relationships in Advanced Carbon Materials*, Report No. TOR-0079(4726-04)-1, The Aerospace Corporation, El Segundo, CA (25 September 1979).
43. Manocha, L. M., and Bahl, O. P., *Carbon* **26**, 13 (1988).
44. Manocha, L. M., Yasuda, E., Tanabe, Y., and Kimura, S., *Carbon* **26**, 333 (1988).
45. Meyer, R. A., and Gyetvay, S. R., In *Petroleum Derived Carbons*, J. Bacha, J. Newman, and J. L. White, Eds., ACS Symp. Series **303**, p. 380, ACS (1986).
46. Jenkins, G., Kawamura, K., and Ban, L. L., *Proc. R. Soc. London* **A327**, 501 (1972).
47. Jabloner, H., U.S. Patent No. 4,070,333 (24 January 1978).
48. Barry, W. T., Gaulin, C., and Kobayashi, R., *Review of Polyarylacetylene Matrices for Thin-Walled Composites*, Report No. TR-0089(4935-06)-1, The Aerospace Corporation, El Segundo, CA (25 September 1989).
49. Katzman, H. A., *Polyarylacetylene Resin Composites*. TR-0090(5935-06)-1, The Aerospace Corporation, El Segundo, CA (2 April 1990).
50. Zaldivar, R. J., Rellick, G. S., and Yang, J. M., "Processing Effects on the Mechanical Behavior of Polyarylacetylene-Derived C-C," *SAMPE J.* (in press).
51. Brown, S. C., and Reese, H. F., *Proc. JANNAF RNTS Mtg.*, CPIA Publ. No. 496, Patrick AFB, FL (1986).
52. Zaldivar, R. J., Kobayashi, R., Rellick, G. S., and Yang, J. M., "Carborane-Catalyzed Graphitization in Polyarylacetylene-Derived C-C," *Carbon* (in press), and *Ext. Abstr.*, *20th Carbon Conf.* (1991), p. 388.
53. Franklin, R. E., *Proc. R. Soc. London* **A209**, 196 (1951).
54. Hishiyama, Y., Inagaki, M., Kimura, S., and Yamada, S., *Carbon* **12**, 249 (1974).
55. Kimura, S., Tanabe, Y., Takase, N., and Yasuda, E., *Jpn. J. Chem. Soc.* **9**, 1479 (1981).
56. Rellick, G. S., and Adams, P. M., Aerospace Sponsored Research Program unpublished results.
57. Kyotani, T., Sonobe, N., and Tomita, A., *Nature* **331**, 331 (1988).
58. Johnson, J. W., Rose, P. G., and Scott, G., *Third Conf. on Indust. Carbons and Graphites*, SCI, London (1971), p. 443.
59. Fitzer, E., and Burger, A., In *Carbon Fibers: Their Composites and Applications* **134**, The Plastics Inst., London (1971).

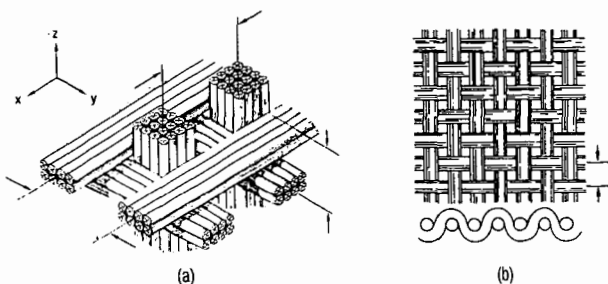


Figure 1. Schematic of (a) 3-D block construction and (b) 2-D plain-weave fabric (McAllister and Lachman [10]).

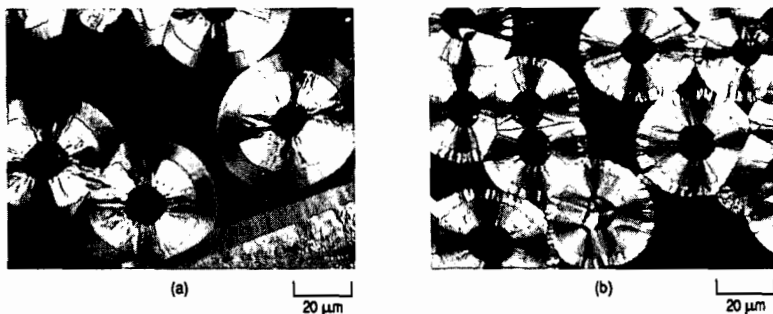


Figure 2. Polarized-light micrographs showing as-deposited CVI carbon microstructures of two specimens. Deposition sequence: (a) RL/SL; (b) SL/RL (Rellick [28]).

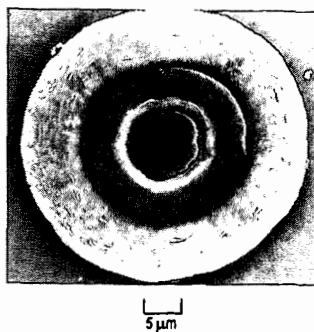


Figure 3. Scanning electron micrograph of specimen after heat treatment at 2500°C for 1 hr [28].

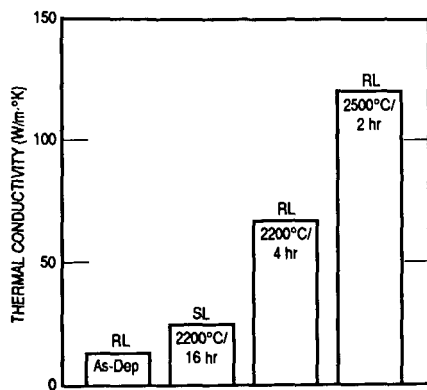


Figure 4. Through-thickness thermal conductivity (at RT) for composite specimens of different CVI structures and processing stages [28].

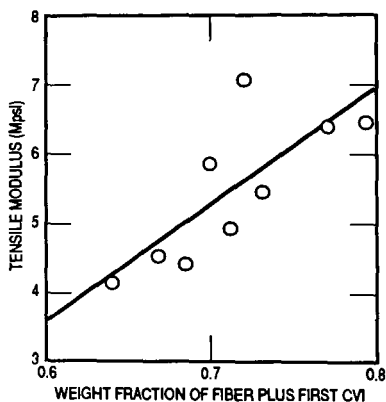


Figure 5. Composite tensile modulus versus weight fraction of fiber plus heat-treated CVI [28].

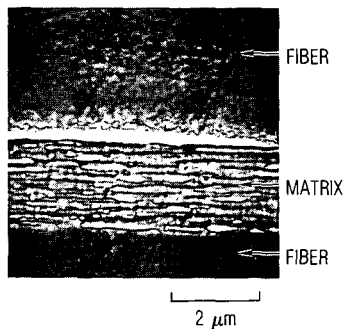


Figure 6. SEM showing highly aligned coal-tar-pitch-derived graphite matrix in the interfilament region of a C/C composite. Fibers are Amoco T50 from PAN.

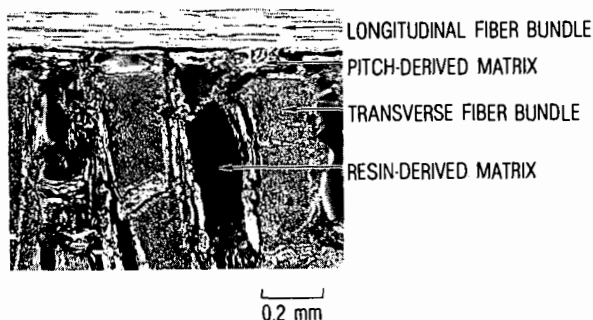


Figure 7. Optical micrograph of cross section of 3-D C/C composite densified with both pitch and resin and heat-treated to 2750°C. Note extensive matrix microcracking.

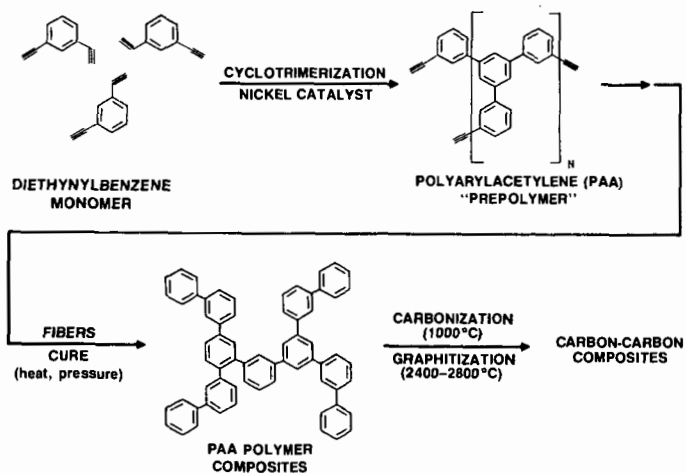


Figure 8. Chemical structure and processing of PAA-based composites (Barry *et al.* [48] and Katzman [49]).

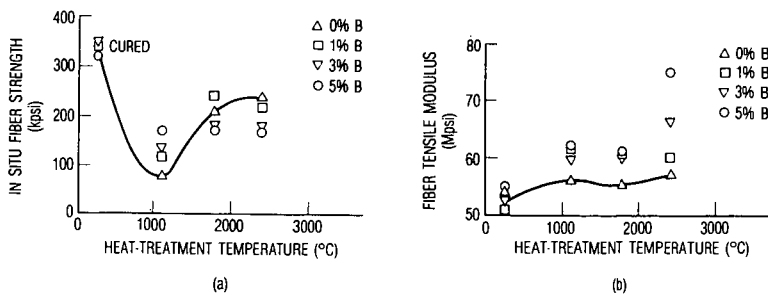


Figure 9. Plots of tensile (a) strength and (b) fiber modulus of undoped and B-doped PAA/T50 C/C composites (Zaldivar *et al.* [52]).

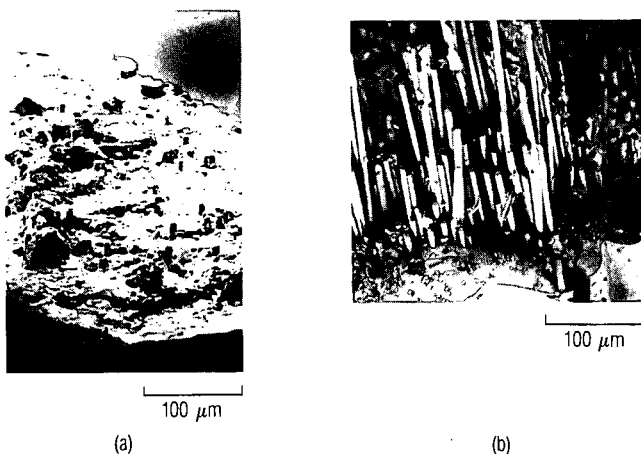


Figure 10. Micrographs of fracture surfaces of (a) undoped and (b) B-doped PAA-derived C/C composites heat-treated to 1100°C [52].

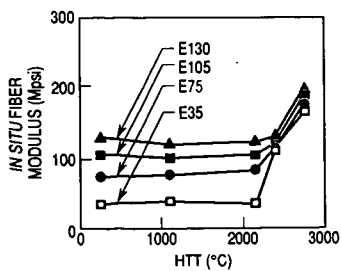


Figure 11. Moduli of composites versus HTT (Zaldivar *et al.* [7]).



Figure 12. Fracture surface of E105 composite to 2750°C HTT, showing matrix sheath tube (Zaldivar *et al.* [7]).

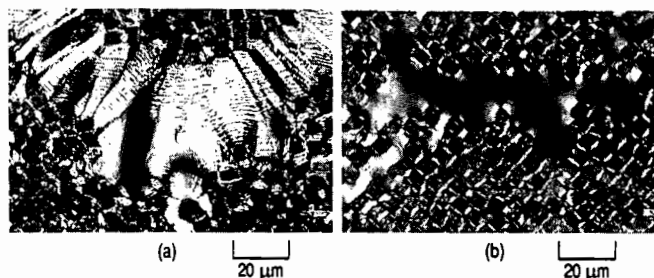


Figure 13. Polarized-light micrographs of unidirectional C/C composite heat-treated to (a) 2900°C and (b) 1100°C (Rellick *et al.* [6]).



Figure 14. SEM micrograph of PX-7 filament embedded in PAA-derived carbon matrix heat-treated to 2750°C.

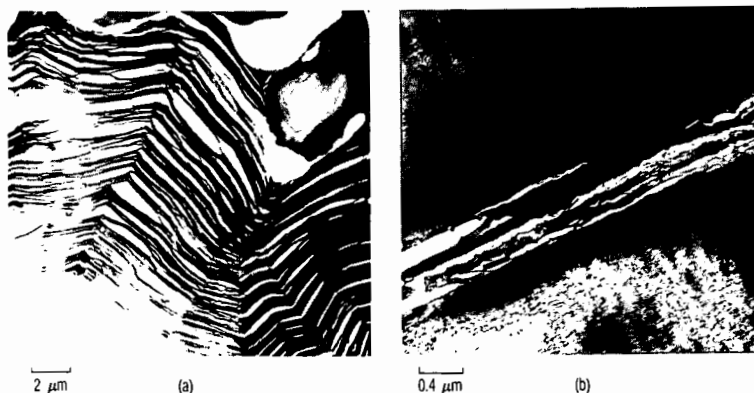


Figure 15. TEM bright-field images of C/C resin-matrix-derived unidirectional composite: (a) transverse and (b) longitudinal sections (Rellick and Adams [56]).

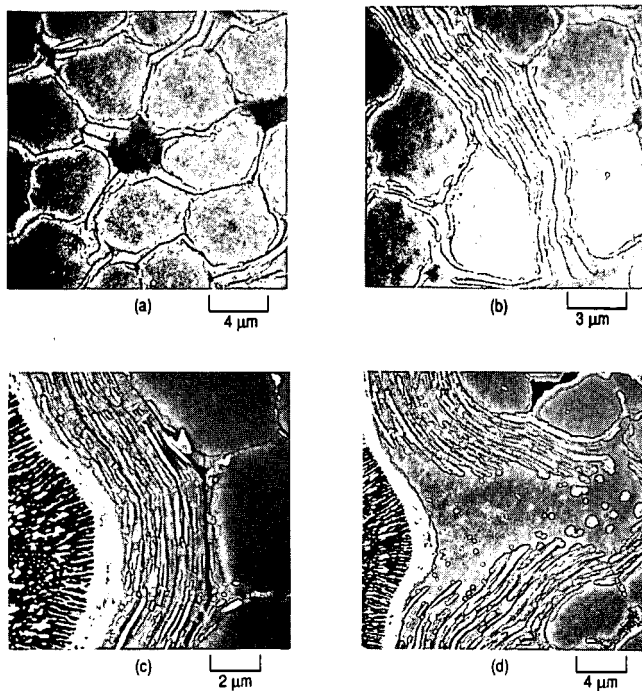


Figure 16. SEMs of ion-etched unidirectional C/Cs heat-treated to 2900°C (Rellick *et al.* [6]).



Figure 17. SEM fracture surface of T50/SC1008 heat-treated to 2900°C [6].

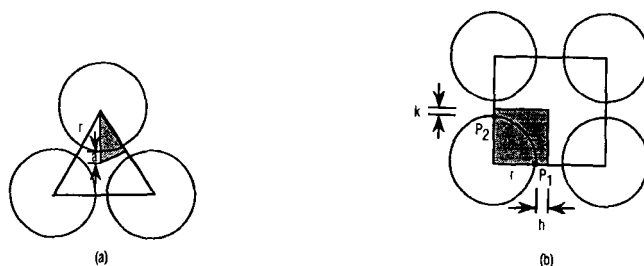


Figure 18. Schematic of the local packing arrangement of (a) three and (b) four fibers. Shaded area denotes region for which stresses are calculated [6].

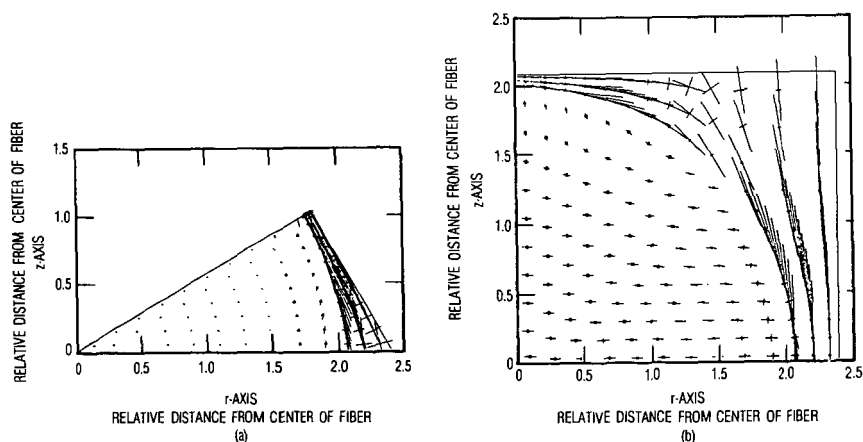


Figure 19. Computer plot of the directions and relative magnitudes of the matrix stresses in the plane of the fiber of various points, relative to Figs. 18a and b [6].

PRODUCTION OF CARBON MATERIALS FROM BIOMASS

Michael A. Serio, E. Kroo, R. Bassilakis, P. R. Solomon
Advanced Fuel Research, 87 Church Street, East Hartford, CT 06108

R. Malhotra
SRI International, 333 Ravenswood Avenue, Menlo Park, CA 94025

KEYWORDS: Biomass, Carbon, Materials

INTRODUCTION

Lignin is the most abundant renewable aromatic polymer. There is an abundance of lignin residues produced as a byproduct of pulp and papermaking which have a fuel value of between \$0.00 and \$0.04 per pound (1). The size of this resource can be appreciated by considering that the total amount of lignosulfonates and kraft lignin together outweigh the sum of all manmade polymers in the United States (2). Given the relatively low cost, high abundance, and renewable nature of this resource, it is not surprising that many attempts have been made to develop higher value products from lignin (1,3,4).

Carbon materials are a much higher added value product than almost any other use of the products which can be produced from lignin. This is especially true in the case of carbon fibers. Carbon fibers are becoming increasingly important as components of composite materials due to their unique chemical and physical properties (5). The finished fibers can sell for tens to hundreds of dollars per pound, so the potential exists for a large premium to be paid for a feedstock which could result in lower manufacturing costs or superior fiber properties. Consequently, the development of processes which can utilize lignins for this purpose and the production of other high value carbon materials has the potential for a high payoff. It would also result in the utilization of lignin as a raw material for a high technology, internationally competitive industry.

EXPERIMENTAL

Sample Selection - A set of eight different lignin samples was examined. The lignin samples and their sources are listed in Table 1. The first six samples were used in a previous project (6) and the last two were obtained specifically for the current project (7).

Table 1 - LIGNIN SOURCES

<u>Lignin</u>	<u>Wood</u>	<u>Manufacturer</u>	<u>Pre-Treatment</u>
Iotech	Aspen	Iotech Corp. ^a	Steam explosion
Stake (ST)	Aspen	Stake Tech. Ltd. ^a	Autohydrolysis
BEC	Aspen	Biological Energy Corp. ^b	-
Indulin I	Pine	Westvaco ^c	-
Ethanol (ET)	Aspen	d	Steam explosion
H ₂ SO ₄	Aspen	d	Steam explosion
SE	Poplar	VPI	Steam explosion
RTI		Repap Technologies	Ethanol/water Extraction

Notes for Table 1

- a. Extraction in dilute basic solution followed by precipitation with dilute acid.
- b. Wood chips are cooked with an ethanol-water solution in an autoclave at 130°C for 30-90 minutes.
- c. Wood is cooked with a 10% solution of 80/20 volume % sodium hydroxide/sodium sulfide. Trade name is Indulin ATR-CK1.
- d. Prepared by Eitan Avni at the University of Connecticut from wood steam exploded by Iotech Corp.

The lignin samples were chosen to represent a range of wood types and preparation methods.

Experimental Approach - The production of carbon materials from lignin is made difficult by the fact that it is highly substituted with oxygen functional groups. This makes the material too reactive toward crosslinking reactions for the formation of anisotropic carbons. These groups must be removed without removing much of the aromatic material which is desirable for the production of carbon materials. The approach taken in this study was to first pyrolyze the lignins to produce a tar and then to thermally and/or catalytically treat the tars to produce a material which could be a substitute for mesophase pitch produced from petroleum. The basis for this approach was previous work done on coal tars which suggested that secondary pyrolysis of tars would reduce the amount of functional group substituents and reduce the average molecular weight (8-11). In order to implement this approach, a two-stage reactor system was developed, as described below and in Ref. 7.

Two-Stage Fixed-Bed Reactor - The lignin pyrolysis/tar cracking experiments were done in a reactor with two separate pyrolysis zones with independent temperature regulation capabilities and with the ability to monitor the product tars on-line with FT-IR spectroscopy (see details of TG-FTIR software-hardware principles discussed below) using an IBM IR-40 spectrometer. A portion of the product stream is extracted out through a filter by means of a peristaltic pump through a line which bypasses the multi-pass cell. The tar component of the products which collected on the filter (cotton wool) was washed out with acetone, dried, weighed and used for further analysis. Helium was used as the carrier gas and the best reproducibility was achieved at pumping rates which resulted in 10-30% extraction of the tar.

The typical experimental conditions were as follows: sample weight: 0.15 ± 0.05 g; He flow: 0.47 liter/min, cm^2 (inner tube I.D. is 0.7 cm). The heating rate (upper chamber) was 30°C/min. (max. temp 780°C) and the secondary pyrolysis (lower chamber) temperature was kept constant during the whole experiment at temperatures ranging from 400 to 700°C. The carbon content of the tar deposited on the wall of the inner tube or on the catalyst surface was measured by replacing the He flow with O_2 . The upper and lower chamber temperatures were raised up to 700°C separately to achieve complete combustion and the CO_2 and CO measured.

This reactor was used primarily for experiments where lignin was pyrolyzed in the first stage at a constant heating rate and the tars were passed to an isothermal second stage. Experiments with both the second stage empty and filled with a catalyst bed were done.

Catalyst Selection - The catalyst examined in the second stage was Alcoa (Type F-20) chromatographic grade 80-200 mesh activated Alumina (EM Science). Glass wool was used to support the catalyst particles. Other catalysts, such as calcium oxide, were considered but good results were obtained initially with alumina and it was used for the remainder of the study. The alumina was chosen because it has a high affinity for polar materials and the goal was to selectively remove oxygen functions from lignin tar. It is also a material which can easily be regenerated once coke formation has occurred.

RESULTS

Lignin Characterization Experiments - A series of lignin screening experiments was done to see how many lignins would be suitable candidates for this approach. These experiments were done in a TG-FTIR system developed at AFR (12,13). The apparatus consists of a sample suspended from a balance in a gas stream within a furnace. As the sample is heated, the evolving volatile products are carried out of the furnace directly into a 5 cm diameter gas cell (heated to 150°C) for analysis by FT-IR. The FT-IR can obtain spectra every 0.2 s to determine quantitatively the evolution rate and composition of several hydrocarbon compounds. The system allows the sample to be heated on a pre-programmed temperature profile at rates between 3°C min⁻¹ and 100°Cs⁻¹ up to a temperature between 20 and 1000°C and held for a specified time. The system continuously monitors: 1) the time-dependent evolution of the gases (including specific identification of the individual species such as, CH₄, C₂H₂, C₂H₄, C₂H₆, C₃H₈, benzene, etc.; 2) the heavy liquid (tar) evolution rate and its infrared spectrum with identifiable bands from the functional groups and 3) weight of the non-volatile material (residue). An analysis of C, H, N and S in the residue at the end of the pyrolysis experiment can be obtained by introducing oxygen to burn the residue and analyzing the combustion products.

As an example of the analysis procedure, the pyrolysis of the lotech lignin is described. Figure 1 illustrates the weight loss from this sample, the sum of the evolved products, and the temperature history. A 20 mg sample is taken on a 30°C/min temperature excursion in the helium sweep gas, first to 150°C to dry for four minutes and then to 900°C for pyrolysis. The evolutions of gases derived from the IR absorbance spectra are obtained by a quantitative analysis program that employs a database of integration regions and calibration spectra for different compounds (12,13). Figures 1b through 1f illustrate the evolution rates and integrated amounts evolved for Tar, CH₄, H₂O, CO₂ and CO, respectively. Because the data are quantitative, the sum of the evolved products matches the weight loss as determined by the TGA balance (Fig. 1a).

The results from a standard (30°C/min) TG-FTIR analysis of the eight lignin samples are summarized in Fig. 2. The tar yields from the eight samples ranged from ~10 wt. % tar for the H₂SO₄ lignin to > 50 wt. % for the lotech lignin. A number of the lignins gave relatively high tar yields (>30 wt. %), so it appears that the generation of primary lignin tar by pyrolysis is a good starting point. An especially interesting sample was the Repap Technologies (RTI) lignin. This sample is produced in large quantities as a byproduct of a proposed organosolv pulping process.

The amount of tar formed was sensitive to the heating rate of the primary pyrolysis stage and to the bed depth (7). The results suggested that the highest yields of tar would be obtained in a dilute phase, entrained flow pyrolysis experiment. This is similar to what has been observed in the case of coal pyrolysis (14).

Experiments In Two-Stage Reactor - A series of experiments was done in the two stage reactor with an alumina catalyst with two of the lignins (SE and RTI) over a range of second stage temperatures (400-700°C). The results from the on-line absorbance measurements are shown for the RTI lignin for various cases in Figs. 3 and 4. For both lignins, a significant reduction in oxygen functions was observed in the on-line FT-IR spectra of the tar when the catalyst (alumina) is present, but not when it was absent.

The IR spectra of both the SE and RTI lignin are very similar and the oxygen containing functional groups appear at 1215, 1107 and 1060 (C-O) cm^{-1} as well as 1607 (C=O) cm^{-1} . To characterize the polar nature (oxygen content) of a tar we use the parameter

$$PI = \frac{\frac{A(1215)}{A(1508)} + \frac{A(1107 \text{ or } 1060)}{A(1508)}}{2}$$

where $A(\nu)$ is the peak height of the νcm^{-1} peak and PI is a polarity index. The smaller the value of PI, the less oxygen the tar contains and the better it might be as a precursor for carbon materials.

Figure 5a shows PI for the main tar evolution peaks for SE and RTI lignins. Figure 5b shows the corresponding results for the tar yield and deposit formation. These results show that relatively high yields of tar can be obtained at high oxygen removal efficiencies, with relatively low deposit formation. The optimal temperature for operation of the second bed was about 550°C.

CONCLUSIONS

The preliminary conclusions of this work are as follows:

- o A set of eight lignins was characterized using the TG-FTIR programmed pyrolysis system. The amount of tar produced in a standard 30°C/min. pyrolysis of most of the lignins was about 35-50% on a dry basis. The amount of tar produced was found to be sensitive to heating rate and bed depth. Higher heating rates produced higher tar yields while larger bed depths produced lower tar yields.
- o A thermal treatment of the tars in the second stage does not significantly degrade the oxygen content.
- o The presence of activated alumina does significantly and selectively catalyze the decomposition of oxygen functional groups in the tar based on the on-line FT-IR analysis. The main gaseous products of the tar decomposition are CO, CO₂ and CH₄.
- o The activity of the alumina appears to be a maximum for oxygen removal at - 550°C. The loss of tar under these conditions is about 40%.
- o The net yield of modified tar from the current system appears to be - 15% for SE lignin and 20% for RTI lignin under the best conditions. This may be improved by an entrained bed reactor system for the primary pyrolysis stage.

ACKNOWLEDGEMENTS

This work was supported by the United States Department of Energy under Contract No. DE-FG05-90ER80880. The authors also acknowledge helpful discussions with Dr. Helena Chum of the Solar Energy Research Institute (Golden, CO) and Dr. Jairo Lora of Repap Technologies, Inc. (Valley Forge, PA).

REFERENCES

1. Glasser, W.G., "Lignin", in Fundamentals of Thermochemical Biomass Conversion, (R.P. Overend, T.A., Milne, and L.K. Mudge, Eds.), Elsevier Applied Science, 1982, pg. 61.
2. Falkehag, S.I., Appl. Polym. Symp., **28**, 247, (1975).
3. Bungay, H.R., Science, **218**(4573), 643, (1982).
4. Kringstad, K., Future Sources of Organic Raw Materials - CHEMRAWN, (L.E. St-Pierre and G.R. Brown, Eds.), Pergamon Press, New York, 1980, pp. 627-636.
5. Hansen, C.F. and Parker, J.A., "Carbon-Fiber Technology", Presented at 16th Symposium on Polymers in the Service of Man, ACS Div. of IEC, (June 9-11, 1980).
6. Squire, K.R., Solomon, P.R., "Characterization of Biomass as a Source of Chemicals" Final Report to NSF for Contract No. CPE-8107453 (Nov. 1983).
7. Serio, M.A., Kroo, E., Bassilakis, R., Solomon, P.R., and Malhotra, R., "Innovative Methods for the Production of Polymers from Biobased Materials" Final Report to DOE for Contract No. DE-FG05-90ER80880 (May 1991).
8. Serio, M.A., "Secondary Reactions of Tar in Coal Pyrolysis", Ph.D. Thesis, Department of Chemical Engineering, Massachusetts Institute of Technology, Cambridge, MA, (1984).
9. Serio, M.A., Peters, W.A., Sawada, K., and Howard, J.G., "Secondary Reactions of Nascent Coal Pyrolysis Tars", Proceedings of the International Coal Conference on Coal Science, p. 533, Pittsburgh, PA, (1983).
10. Serio, M.A., Peters, W.A., Sawada, K., and Howard, J.G., ACS Div. of Fuel Chem. Prepr., **29**(2), 65, (1984).
11. Serio, M.A., Peters, W.A., and Howard, J.G., Ind. Eng. Chem. Res., **26**, 1831, (1987).
12. Carangelo, R.M., Solomon, P.R., and Gerson, D.J., Fuel, **66**, 960, (1987).
13. Whelan, J.K., Solomon, P.R., Deshpande, G.V., and Carangelo, R.M., Thermogravimetric Fourier Transform Infrared Spectroscopy (TG-FTIR) of Petroleum Source Rock - Initial Results, Energy and Fuel, **2**, 65, (1988).
14. Howard, J.B., Peters, W.A., and Serio, M.A., "Coal Devolatilization Information for Reactor Modeling", Report Prepared under EPRI #AP-1803/RP 986-5, (April 1981).

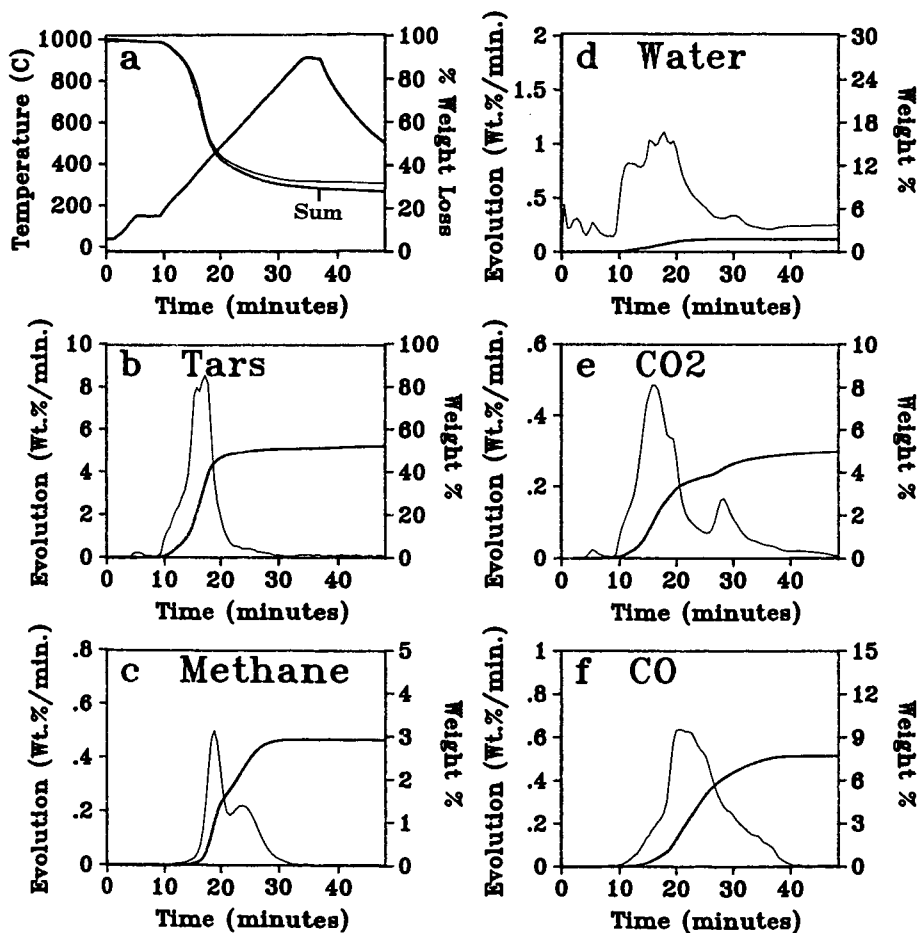


Figure 1. TG-FTIR Analysis of Iotech Lignin at 30°C/min.

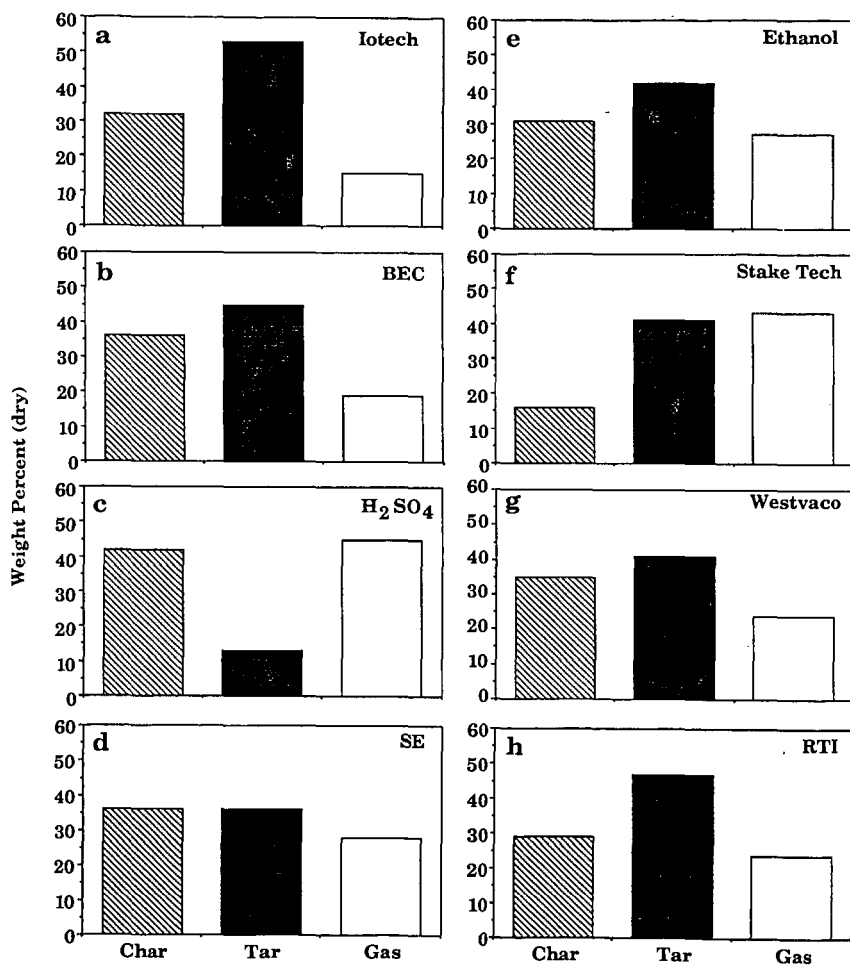


Figure 2. Comparison of Char, Tar and Gas Yields from Programmed Pyrolysis of Eight Lignins.

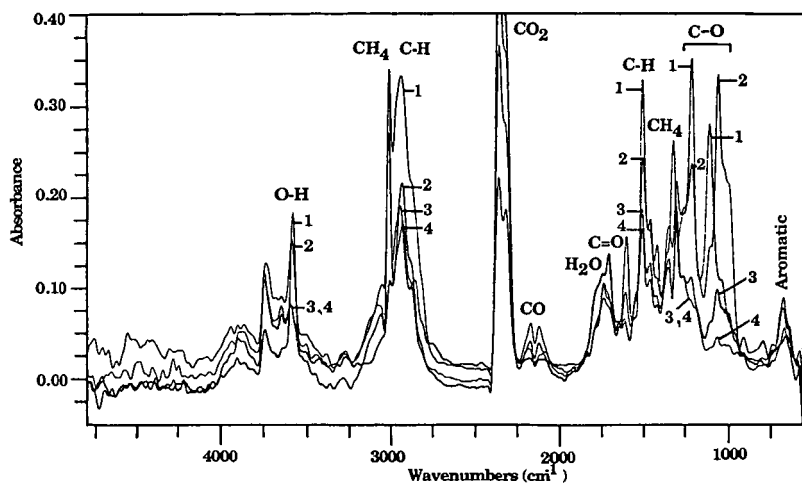


Figure 3. On-Line Tar Spectra from Experiments in the Two-Stage Fixed-Bed Reactor with RTI Lignin. Case 1 = 400°C, No Catalyst; Case 2 = 400°C, with Catalyst; Case 3 = 550°C, with Catalyst; and Case 4 = 600°C, with Catalyst.

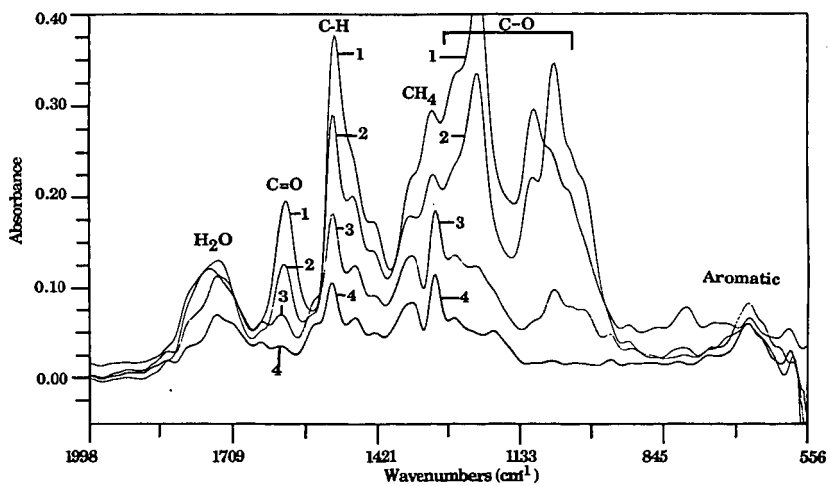


Figure 4. Expanded View of Spectra in Fig. 3.

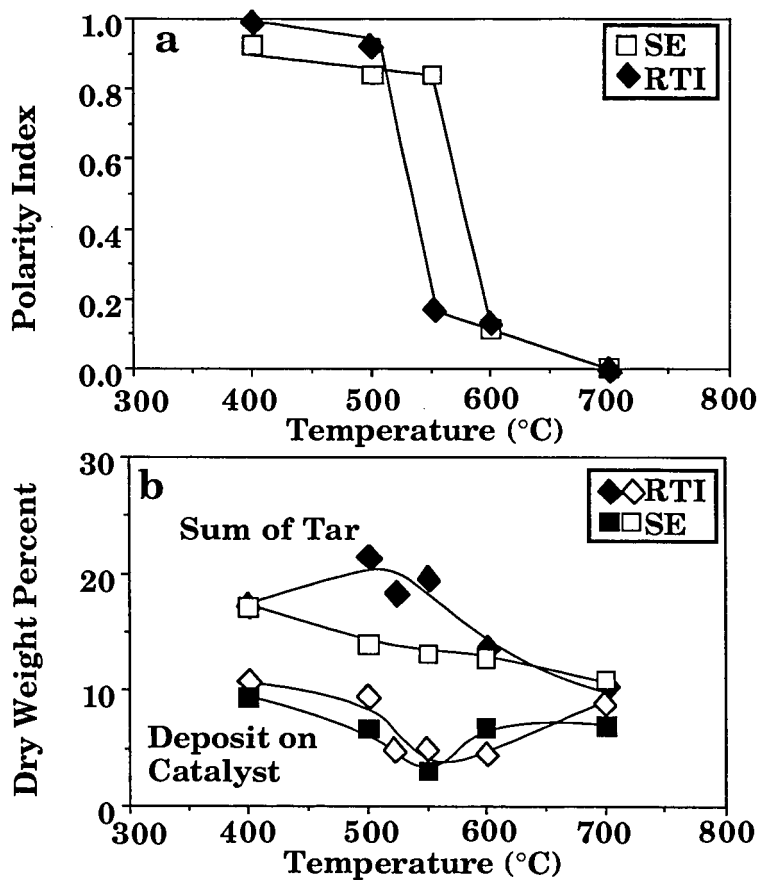


Figure 5. Effect of Lignin Type and Temperature on a) Tar Polarity Index and b) Tar Yield (◆, □), Deposit Yield (◇, ■).

**EFFECTS OF POLYETHYLENE TEREPHTHALATE (PET)
FROM PLASTICS WASTE ON THE THERMAL PROPERTIES OF ASPHALT**

RAMONA LEDESMA AND L.L. ISAACS
The City College of CUNY
Dept. of Chemical Engineering
New York, N.Y. 10031

Keywords: Thermal Characterization of asphalt/PET mixtures, waste plastic utilization, filled asphalt.

INTRODUCTION

Asphalt concretes are widely used for pavements. Asphalt itself is a bitumen and although it occurs naturally, it is mostly obtained as a byproduct of oil production. However, its thermoplastic characteristics cause difficulties with roads. It has been demonstrated that the apparent glass transition temperature of asphalt is near zero degree celsius [1,2]. Thus, asphalt concretes are susceptible to low temperature cracking that may lead to fracture. Further, in high summer temperatures asphalt undergoes flow or creep. The stability of asphalt paving surfaces requires that it does not flow or creep under heavy load. Numerous investigations are underway involving the modification of asphalt with different fillers that may improve its pavement performance. For example, the modification of asphalt with polymers leads to bituminous materials having improved properties and allows the utilization of waste products [3].

In this investigation, the effect of polyethylene terephthalate (PET) obtained from used plastic bottles on the thermal properties of asphalt, specifically its effect on the thermal expansion coefficients, glass transition temperatures, melting points, and flow properties of asphalt, PET, and asphalt/PET mixture samples, is evaluated. Polyethylenes have been confirmed as potentially useful modifiers for increasing the low temperature fracture toughness of the asphalt and may also contribute to pavement stability at elevated temperatures by minimizing distortion due to creep [4]. The abundance of used plastic bottles that contributes to the litter problem and the resultant environmental pollution caused by conventional non-degradable plastics makes PET fillers economically attractive for improving the performance of asphalt concrete paving materials.

EXPERIMENTAL TECHNIQUES

Sample Preparation

Asphalt of grade AC-20 certified to comply with the state of New York highway specifications was provided by Prima Asphalt Conc., Inc. Polyethylene terephthalate (PET) filling material was obtained from used plastic soda bottles that were first cut into

strips about 1/4 inch in thickness and then ground using a grinder with a 20 mesh sieve.

The asphalt/PET mixtures were prepared by slowly adding a weighted amount of PET to a known quantity of asphalt maintained at 120°C while the mixture was vigorously stirred. This temperature is below the melting point of PET but above that of asphalt. After several minutes of stirring, the mixtures were left to cool to room temperature, and stored until used for testing. Sample concentration ranged from 10% to 50% PET by weight.

DSC Measurements

The glass transition temperatures (T_g) and the melting points of asphalt, PET, and asphalt/PET mixtures were measured using differential scanning calorimetry (DSC). The samples were heated at a 10 °K/min rate. between 100°K and 600°K.

TMA measurements

Thermomechanical analysis (TMA) was employed to determine the expansion coefficients, glass transition temperatures (T_g), melting points, and flow properties of asphalt, PET, and asphalt/PET mixture samples. The temperature range of the measurements was between 100°K and 600°K. Cylindrical samples approximately 9.5 millimeter in diameter and between 0.3 and 3.0 millimeter in thickness were heated at a rate of 5°K/min. Expansion coefficients were calculated from the TMA expansion profiles using aluminum expansion coefficient data to determine the dynamic calibration constant. A 5 grams mass supplied the compressive force to the samples. Flow properties were measured using parallel plate rheometry. Samples were compressed by a 50 gram load.

DISCUSSION AND RESULTS

Differential Scanning Calorimetry

Based on several DSC runs, the average T_g for pure asphalt was calculated to be -41.4°C. Values for asphalt T_g 's in the literature range between -0.4°C to -53°C [5,6]. In general, the change in the heat flow curve slope indicating the glass transition temperature was very small and sometimes even undetectable; consequently, it was very difficult to characterize the samples using DSC technique. However, in the cases where it was detected, the DSC results were reproducible and yield T_g values within the 5% accuracy of the instrument.

The PET/asphalt mixture DSC measurements yield T_g values in the same range as those obtained for pure asphalt. There was no

indication that the presence of PET fillers affected the Tg of asphalt. Fig. 1 is the plot of the Tg versus PET concentration.

DSC was also used to measure the melting point (Tm) of PET. For pure PET the average melting point was determined to be 235.4°C. As with the asphalt Tg, there was no indication that the melting point of PET was affected by the presence of asphalt. The average melting temperature of PET calculated using results obtained from pure PET and PET/asphalt mixtures was estimated as 234.9°C. Fig. 2 is a plot of the PET Tm values versus mixture composition. Literature gives a range for the melting point of pure PET between 250°C and 265°C. Taking into account the difference in techniques used, the accuracy of the instrumentation, and the fact that the DSC results were obtained using PET from used plastic bottles instead of pure PET, The discrepancy between the DSC findings and literature values is not unexpected.

Thermomechanical Analysis

As stated previously, the average Tg value for asphalt was estimated at -41.4°C. In general, the asphalt Tg obtained using the TMA technique is about 70 degrees higher than those obtained by the DSC technique. This discrepancy may be attributed to the fact that these techniques measure different phenomena. The Tg by DSC corresponds to a change in the ability of the sample to absorb heat, while the TMA detects the Tg as a change in the thermal expansion profile of the sample.

The average Tg for asphalt as determined by the TMA technique was estimated as 39°C; the value estimated including glass transition temperatures obtained for the PET/asphalt mixtures is 33.4°C. A plot of the average asphalt Tg values versus PET concentration is shown in Fig. 3.

The melting point of PET was also measured using the TMA technique. These measurements yield 248.3°C as an average Tm for PET, and an average Tm value of 243.8°C for the asphalt/PET mixtures. These TMA results are about 10 degrees higher compared to the DSC findings and that much closer to the literature values. In Fig 4, the average Tm values are plotted as a function of asphalt concentration.

Examination of the TMA curve shows that PET exhibits a glass transition temperature at about 81°C that was not detected when the DSC technique was used. PET TMA measurements yield an average Tg of 81.8°C with values ranging from 80.4°C to 85.8°C. The literature [7] value for PET Tg is 81°C. Unlike the previous findings, the glass transition temperature of PET does seem to be affected by the presence of asphalt; so much that it was not possible to detect it with certainty from examination of the TMA curves for PET/asphalt mixtures. Furthermore, when the PET samples were subjected to a heating cycle, the Tg could not be detected.

The expansion coefficients were determined from TMA expansion/contraction profiles. An example of a TMA expansion/contraction profile for a PET sample is shown in Fig 5. Note that in this figure the slope of the TMA curve noticeably changes after the crossing of the glass transition temperature. For PET samples, two distinct regions are observed: a region that ranges from liquid nitrogen temperatures to about 81°C, the glass transition temperature of PET, and second one that extends from 81°C to the melting temperature. The average expansion coefficient for the first region is 109 $\mu\text{m}/\text{m}/^\circ\text{C}$. The average expansion coefficient for the second region was estimated to be 955 $\mu\text{m}/\text{m}/^\circ\text{C}$. The expansion coefficient for asphalt was found to be 290 $\mu\text{m}/\text{m}/^\circ\text{C}$.

The addition of PET to asphalt has a more pronounced effect on the expansion coefficient. The addition of 10 wt% PET to asphalt reduces the expansion coefficient to 108 $\mu\text{m}/\text{m}/^\circ\text{C}$. 20 wt% PET has an expansion coefficient of 89, 30 wt% PET has 85, 40% PET has 83, and a 50 wt% PET mixture has an expansion coefficient of 76 $\mu\text{m}/\text{m}/^\circ\text{C}$, in the first region.

Additional information can be gained by studying the TMA derivative curve, using the parallel plate rheometer accessory [8]. The amplitude of the derivative curve will vary in intensity with the flow of the sample. The temperature of the peak (Ti) corresponds to the point of maximum flow rate. In general, the peak flow rate for PET/asphalt samples are very similar to those of PET. The Ti values range from 248.2°C for a 10/90 PET/asphalt sample to 252.3°C for a PET sample. This suggests that even for 10% PET concentration the overall flow of the mixture is dominated by the flow properties of PET. The PET filler acts as a binder restricting the flow of the asphalt until the filler itself starts melting. The inflection temperatures for pure asphalt range between 48.4°C to 58.6°C with an average Ti of 52.8°C. That is, the maximum flow rate for asphalt occurs at about this temperature.

Fig. 6 is a typical TMA plot for a 10/90 PET/asphalt sample featuring a derivative curve with two inflection points. The first one at 47°C corresponds to the maximum flow rate of asphalt. It is followed by a plateau due to the binding effects of the PET filler. The maximum flow rate of the mixture occurs at 252°C, the second inflection point. At this temperature, the PET filler is melting and flowing out of the rheometer plates together with the remaining asphalt.

A limited amount of viscosity information was also collected using the TMA parallel plate rheometer. The temperature dependent dimensional changes of a sample under a known load in the rheometer are converted to viscosity [9]. As expected there is a change of several orders of magnitude in the viscosity over a narrow temperature range as the sample starts to deform in the shear mode, due to thermal softening, see Figure 7. In the fluid region, the viscosity decreases with increasing temperature.

CONCLUSIONS

- . Thermomechanical analysis and differential scanning calorimetry are useful techniques and yield reproducible results in obtaining melting points, glass transition temperatures, expansion coefficients, and the point of maximum flow rate (inflection temperature).
- . In general, asphalt's glass transition temperature does not seem to be affected by the presence of polyethylene terephthalate fillers.
- . The PET's glass transition temperature was clearly detected by the thermomechanical analysis technique even though the DSC measurements do not show a T_g for PET.
- . The overall flow of the PET/asphalt mixtures is dominated by the flow properties of the PET.

ACKNOWLEDGMENTS

R. Ledesma was supported by a W.R. Grace Graduate Fellowship and by supplemental support of the Plastics Institute of America. The work presented is based on her doctoral thesis.

References

1. Kortschot, M., Woodhams, R.T., Polymer Eng. Sci., **24** (6), 252 (1984).
2. Shim Ton, J., Kennedy, K.A., Piggot, M.R., Woodhams, R.T., Rubber Chem. Technol., **53**, 88 (1980).
3. Lea, E.M., "The Chemistry of Cement and Concrete," Chemical Comp., New York, 1971.
4. Jew, P., Woodhams, R.T., Proceedings of the Association of Asphalt Paving Technologists, **55**, 541 (1987).
5. Breen, J.J., Stephens, J.E., Proceedings of the Association of Asphalt Paving Technologists, **35**, 19 (1966).
6. Schmith, R.J., Santucci, L.E., The Association of Asphalt Paving Technologists, **38**, 706 (1969).
7. Bader, A., Harvey, D., Nagarkatti, J., Aldrich Catalog Handbook, Aldrich Chemical Company, Inc., (1990).
8. Fair, P.G., Gill, P.S., Leckenby, J.N., DuPont Thermal Analysis Application Brief No. TA-90.
9. Dienes and Kelmm, J. Appl. Phys., **17**, 458 (1946).

Ave. Asphalt Tg Vs PET Concentration
Using DSC Technique

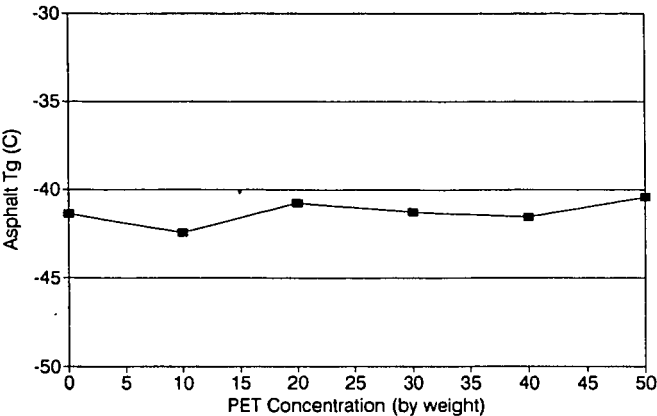


FIGURE 1.

Ave. PET Tm Vs Asphalt Concentration
Using DSC Tehcnique

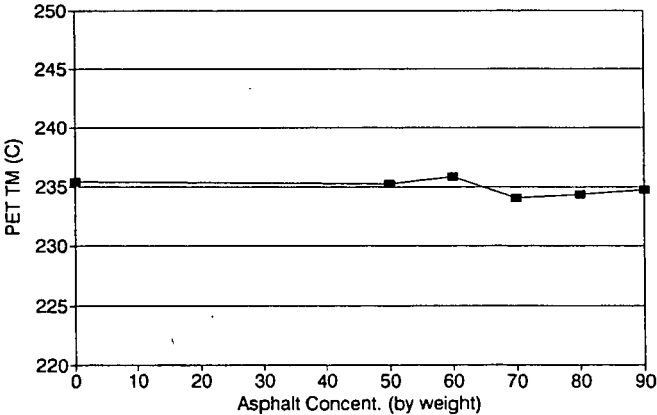


FIGURE 2.

Ave. Asphalt Tg Vs PET Concetration Using TMA Technique

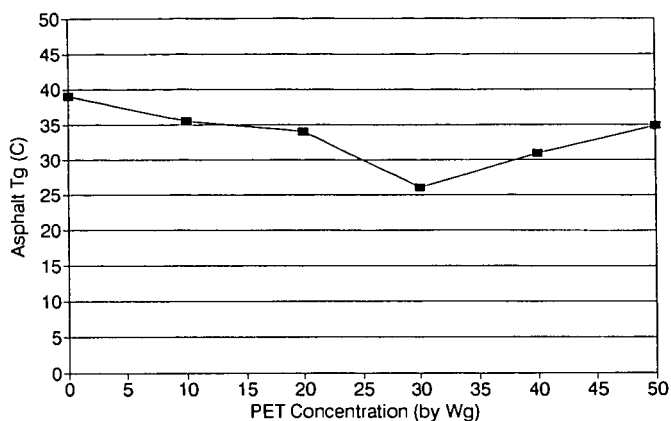


FIGURE 3.

Ave PET Tm Vs Asphalt Concentration Using TMA Technique

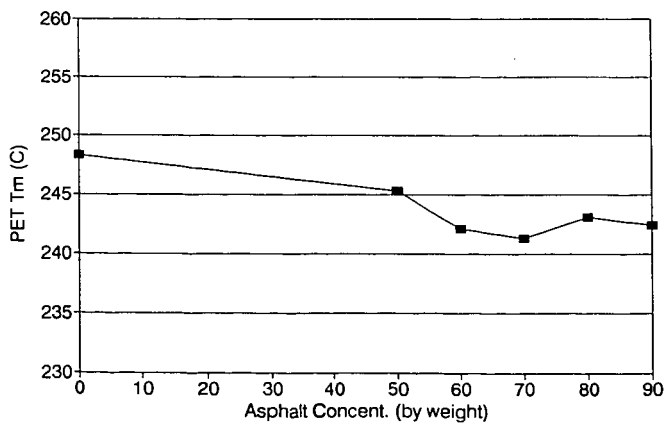


FIGURE 4.

Sample: PET (POWDER)
Size: 2.2900 mm
Method: TMA

File: C: PETASP-TMA.07
Operator: RL
Run Date: 15-Nov-90 11:57

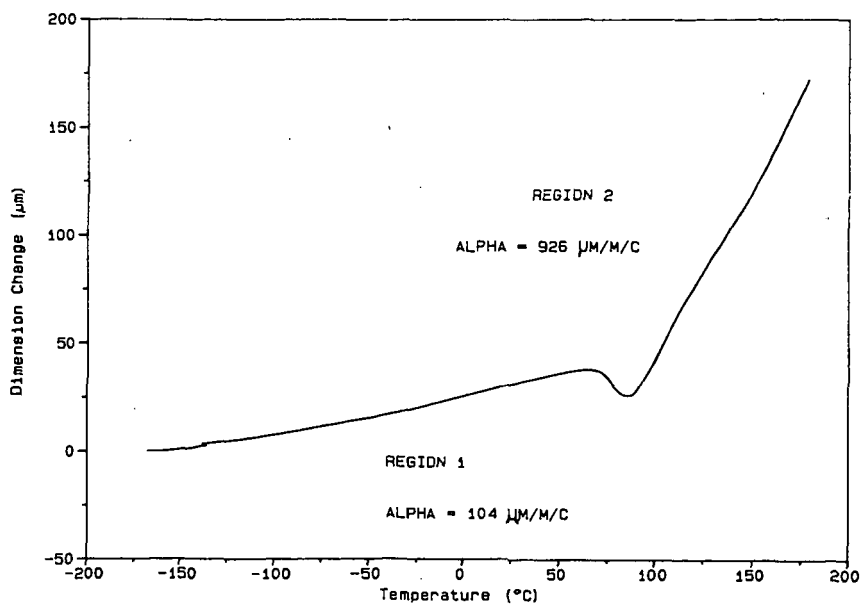


FIGURE 5.

Sample: PET/ASPHALT 10/90
Size: 0.7746 mm
Method: PPR

File: C: ASPE1.19
Operator: RL
Run Date: 23-Jan-91 14:28

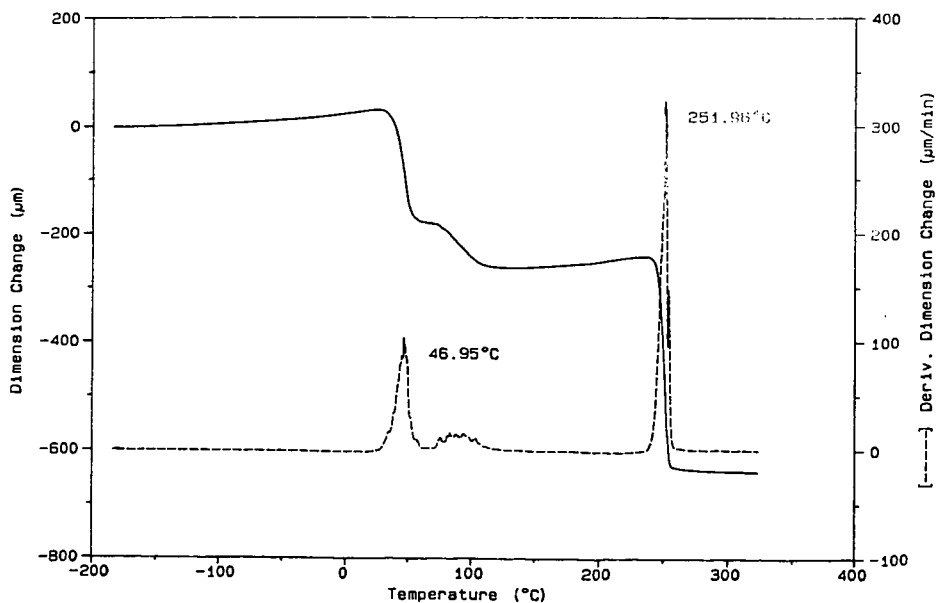


FIGURE 6.

40/60 PET/ASP. Visc. Vs Temp. (TMA PPR)

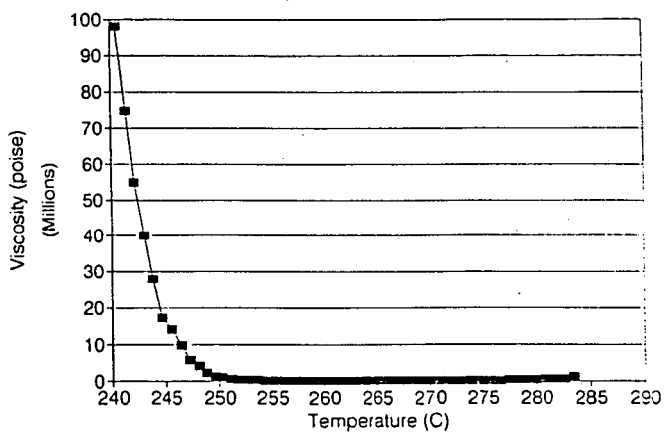


FIGURE 7.

COAL AND CARBON IN THE POST-PETROLEUM WORLD
David G. Walker of WALKER CHEMISTS INC.
904 Fleetwood Drive
Baytown, Texas 77520

Keywords: Coal, carbon, mobile motor fuel

INTRODUCTION: The petroleum age, which we now enjoy, and which makes possible the luxuries, comforts and necessities of our modern world, will not last long. As has already happened in the United States, the ability of the world to produce oil will fail to meet the market demand. The U. S. dodges this problem at present by importing nearly one-half of its oil. In the future the world has scant chance of importing oil from the moon, from Mars, or anywhere else.

The coal deposits of the world are some 100 times as big as the original oil deposits. There was a coal age which preceded the petroleum age. It was associated with the industrial revolution. Iron was made in large amounts by the use of coke from coal. Steam engines using coal drove railroad locomotives, ships and factory engines. Cities were lighted and heated with coal gas. Coal is now used only to make coke and for the generation of electricity. This last market causes air pollution or "acid rain".

Technology exists (pioneered in Germany by Bergius and Fischer-Tropsch in 1920-45) for the conversion of coal to gasoline and diesel oil. This technology was used by US industries and the government in the period 1974-82 in an attempt to make mobile motor fuel using coal as the resource base. This commercialization failed utterly. The conversion of coal to gasoline and diesel yields scarcely more than one-third of the coal's energy in useful products. In addition, the investment and operating costs of these conversion plants are some 15 times as expensive as petroleum refineries. (Gaensslen 1979)

This paper proposes that coal be used to supply mobile motor fuel by a different method. Pure carbon (Boudouard Carbon) is made as a major product from the coal. This carbon serves to replace gasoline, diesel oil and jet fuel.

Refinery Block Diagram: Post-Petroleum World (Figure 1): The future coal refinery will use coal as the raw material. Coal will also be supplemented by shale oil, tar sands and residual petroleum oil.

The coal will be coked in staged, fluidized beds with oxygen for partial combustion to supply the needed heat directly. This section, in addition to coke, will make a good grade of crude oil and sulfur as co-products. Part of the hydrogen-rich gas product is used to up-grade the volatilized hydrocarbons into a synthetic crude oil. The major product is powdered coke (Bloom 1977). The product coke, after briquetting, is transferred to the main section of the coal refinery.

Briquetted coke is gasified in a slagging-ash gas producer using air as oxidant and CO₂ as reductant gas (Ermankov 1957). The CO

and H₂S of the producer gas are separated together from the N₂, CO₂ and H₂ (small) by a solvent (Walker 1987) (Bartish 1983). H₂S is converted into product sulfur in a Claus plant while the CO is converted into CO₂ and Boudouard carbon product. (Donald 1956). The large reaction heat of the Boudouard reactor is used to make electricity as an additional product of the refinery.

Coking Section of the Coal to Carbon Refinery (Figure 2): This follows exactly the COED process which was developed by the FMC corporation and the Office of Coal Research (1960-75). (Bloom 1977). All kinds of coal can be used in this process. The temperatures of the stages of coking are somewhat different with different coals. The amount of oil produced varies from 1 to 1.5 barrels per ton depending upon the coal's volatile matter content. A minor amount of hydrogen-rich gas is available for other uses.

This coking has never been used on large scale commercially. Because the sulfur content of the coke product is just as high as that of the coal feed, the coking must be justified by the difference in price between the oil product and the coal feed. Contemporary price ratios of coal and oil are not yet different enough for this process to be economically viable as long as the coke is simply to be burned in the conventional generation of electricity. However, as is the case of this present proposal, if the coke is used to make a major high grade motor fuel, the economics will be quite different. This coking also has the desirable property of making the available hydrogen content of the coal into liquid hydrocarbons. While not of interest at the present, this can be of immense important in the future when there is no petroleum left. All of the future petrochemical industry might be supplied by this coal refinery side-product: The much larger mobile motor fuel market, at that time, would then be supplied by carbon.

Coke to Carbon Section-Coal to Carbon Refinery (Figure 3) (Hadley-Coates 1988) : Process Description: Coke is fed to a fixed bed slagging-ash gasifier fed with hot air as oxidant and hot CO₂ as reductant gas (Ermankov 1957). Tar and pitch are absent from the producer gas. The sensible heat of the gas is used to generate steam. The cooled gas is dedusted and stringently dried. A separation solvent next quantitatively catches the CO and H₂S content of the gas after which the residual gas is exhausted to the atmosphere (Walker 1987 and Hadley-Coates 1988). The mixed CO and H₂S stream is regenerated from the solvent and then fed to an aqueous ethanalamine solvent unit to quantitatively separate the H₂S from the CO. The H₂S is fed to a Claus plant and converted quantitatively into product sulfur. The pure CO is converted into CO₂ and product carbon in a Boudouard reactor at 500-25 C (Donald 1956). Hot CO₂ is recycled to the gas producer. The temperature of the Boudouard reactor is maintained by evaporating a high temperature organic solvent within heat exchanger tubes. The gaseous organic is then fed across a turbine to generate electricity. The low pressure organic gas from the turbine is condensed in process reboilers at 150 C and recycled to the Boudouard reactor. The process reboilers are used with the separation solvents to catch CO + H₂S and to separate H₂S from CO.

Carbon as Motor Fuel (Figure 4) : Diesel engines were run for many years in Germany in a large scale development program(1910-45). This program used coal dust as the motor fuel. Many devices were developed to feed the coal dust into the engine with successful results. One such device, used by the Germans, is shown at the top of figure 4.

The coal dust engine failed to be commercially successful because of two reasons. The ash content of the coal caused unacceptable wear rates on the cylinder walls, rings and piston heads of the engine. Coal dust, as ground in practical grinders, contains too many large particles. These will not burn up completely in the short times available in a diesel engine. (Soehngen 1976)

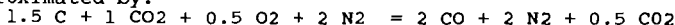
Boudouard carbon is completely ash-free ! In addition, the intrinsic particle size of Boudouard carbon is very small (Watanabe 1929); much smaller than can be obtained than by grinding large solids into powders. (Soehngen 1976). The particle size of Boudouard carbon is small enough to burn completely in a high speed Diesel engine (Essenhight 1979).

Otto-cycle engines compress a fuel mixture of fuel and air and then fire it by an electric spark. Some early engineers once ran a model A car successfully on flour by means of a dust carburetor! Nowadays some cars use injection methods to mix air and gasoline instead of a carburetor. Otto-cycle engines can be made to work on solid and non-volatile fuels like pure carbon.

The turbine-cycle engine is shown diagrammatically. In a turboprop airplane the propeller is tied to the power coupling. With jet planes the hot combusted pressure gas propels the plane directly. This type of engine, while not as efficient as the diesel, puts out a great deal more work per given engine weight. For airplanes this is a decisive advantage. It is also a simple engine which can run for millions of miles in its lifetime provided that the fuel used is very clean.

Boudouard carbon is fine grained and entirely free of ash, pitch or tar. (Watanabe 0. 1929)

Yields and Costs of the Coke to Carbon Part of the Coal to Carbon Refinery: The overall reaction of the gasifier is approximated by:



The yields of the process (based on energy of the coke fed) are estimated to be:

Boudouard Carbon	70 %
Electricity	3 %

Useful Product Yield 78 %

Using Gaenslen's (1979) methods, it is estimated that a coal to carbon refinery will require less than one-third the investment and operating cost of present technology to convert coal to gasoline and diesel oil (Hadley-Coates 1988). It will

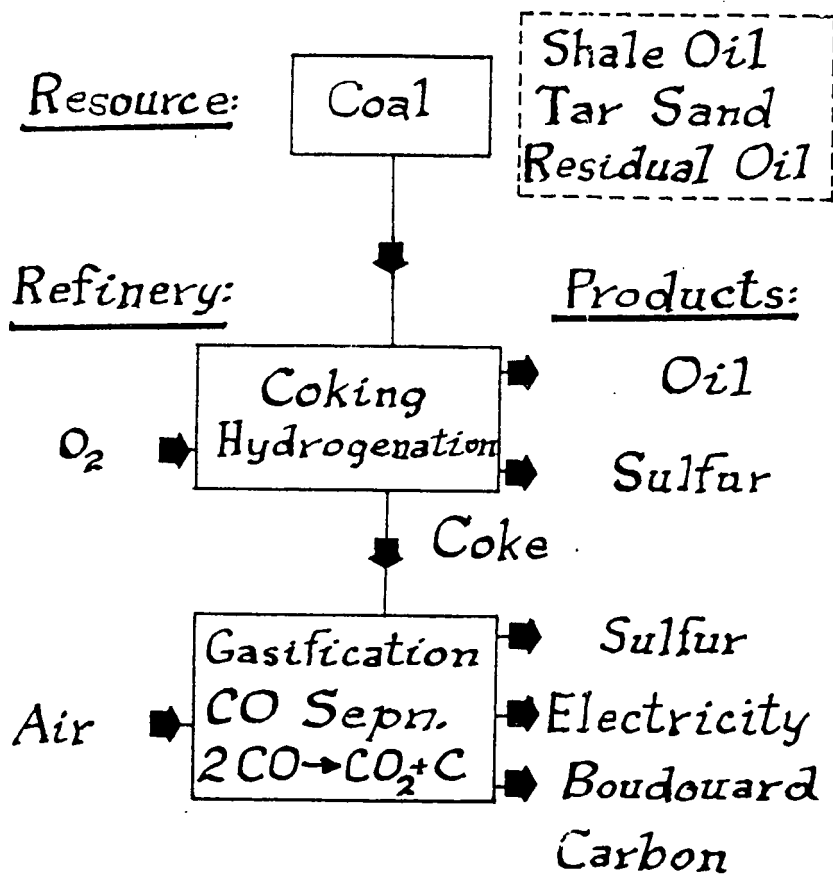
also make twice the yield of useful products.

Final Thoughts: A new technology is possible which uses coal to make Boudouard carbon as a major product. This product can, in the future, supply most of the mobile motor fuel requirements of the world. New directions are required in research and development in order to make this technology a practical reality. I hope that this paper will stimulate many of you to enter this vital and important field of endeavor. You can help to make both it and yourselves successful.

REFERENCES CITED

- Bartish, F., et al 1983- "Carbon Monoxide" in Encyclopedia of Chemical Technology 4 3rd ed. John Wiley
- Bloom, Ralph Jr. & Howard L. Malakook 1977- "COGAS Process for the Conversion of Coal to Gas and Oil Products" ENERGY TECHNOLOGY HANDBOOK D M Considine Ed. McGraw-Hill New York (I:255-61)
- Donald, Jack H 1956- "An Annotated Bibliography of the Literature and Patents Relating to the Production of Carbon by the Decomposition of Carbon Monoxide" Mellon Institute of Industrial Research, Pittsburgh Pa.
- Ermankov, V G 1957- "Production of Technological Gases By Gasification of Lean Fuels with Removal of Liquid Slag" Khimicheskaya Pererabotka Topliva Izd AN SSSR Moscow 1957 400-7
- Essenhigh H. 1979- "Coal Combustion" in COAL CONVERSION TECHNOLOGY 171-312 C Y Yen and S Lee Eds. Addison-Wesley Pub. Co, Reading, Mass.
- Gaensslen, Hans 1979- "A Shortcut to Investment Costs" CHEMTECH, May 306-9
- Hadley-Coates, Lyndon & D G Walker 1988- "Boudouard Carbon : An Alternate to Gasoline and Diesel Oil" INTERNATIONAL JOURNAL OF ENERGY RESEARCH 12 2443-51
- Soehngen, E E 1976- "The Development of the Coal Burning Diesel in Germany" Report FE/WEPO 3387-1 Purchase Order No 3387 U S Energy Research and Development Administration
- Walker, D G 1987- US Patent 4,654,202 31 March 1987 "Separation of Hydrogen Sulfide from Gases by the Use of Cuprous Aluminum Tetrachloride as a Reversible Complexing Agent" US Patent 4,691,074 1 Sept. 1987 "Monochlorobiphenyl: Cuprous Aluminum Tetrachloride"
- Watanabe, O & N. Tokunosuke 1929- "The Nature of Carbons Monoxide Produced by the Catalytic Decomposition of Carbon Monoxide" Bull. Inst. Phy. Chem Research (Tokyo) 8 288-92

FIGURE 1



POST-PETROLEUM ECONOMY

FIGURE 2
Coal to Coke-Oil-Hydrogen: COED Process
FMC Corp. and Office of Coal Research

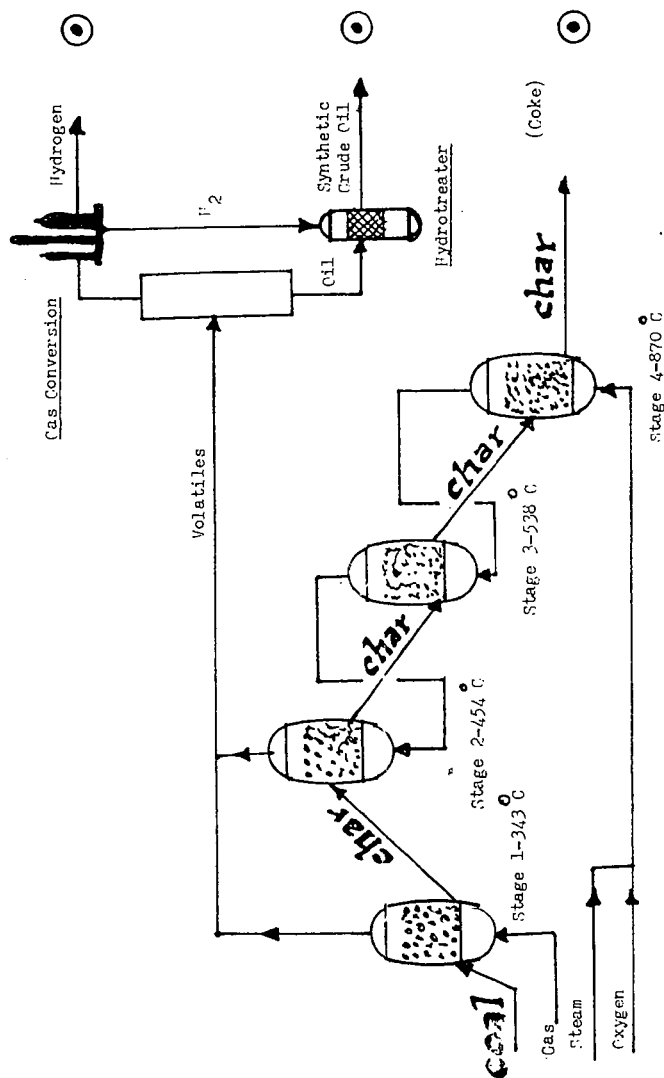
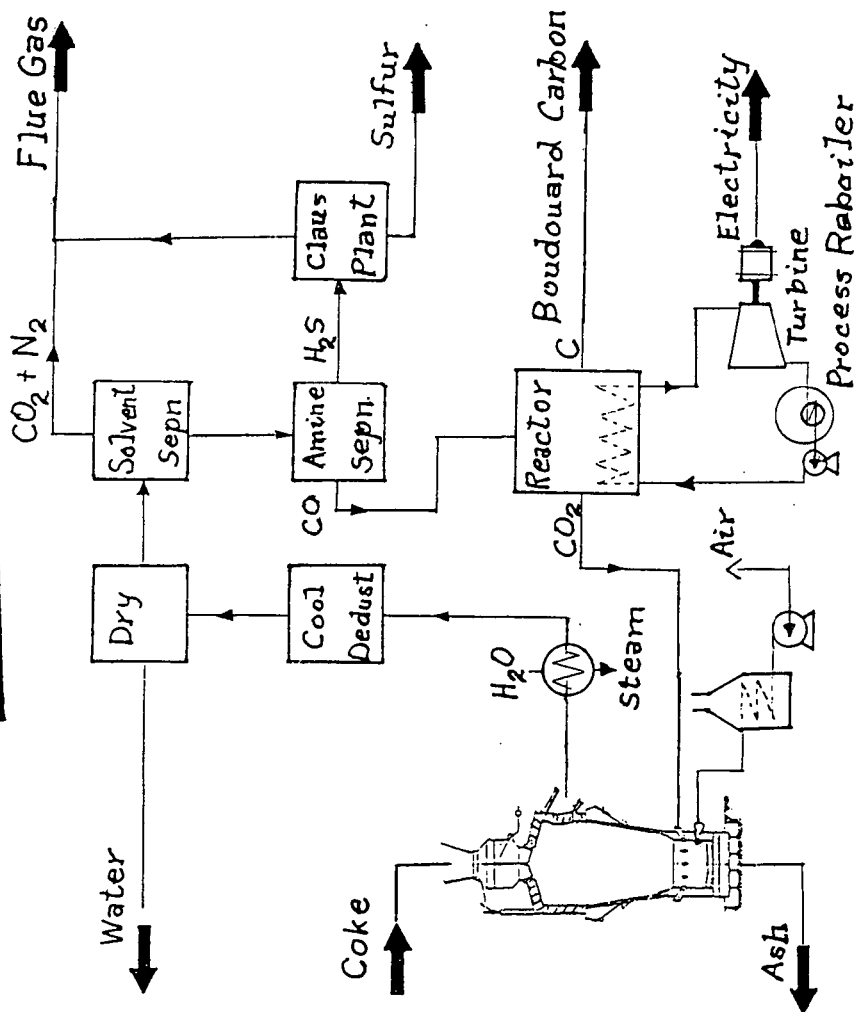


FIGURE 3



COKE TO CARBON REFINERY

Diesel Engine

Otto Cycle Engine

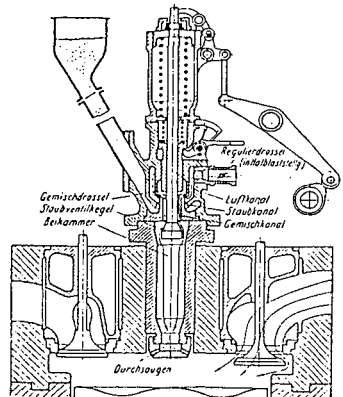
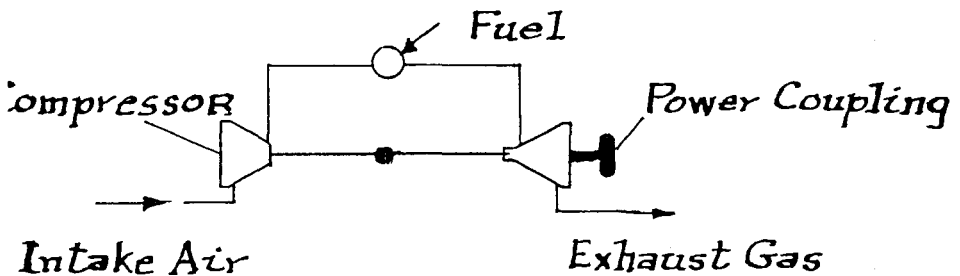


Abb. 301. Schematische Darstellung der pneumatischen Staubinjektion nach dem Verfahren NÄDEL-ZÄNNER.

Turbine Engine



CARBON AS MOTOR FUEL

FIGURE 4